



Soot-PCF: Pore condensation and freezing framework for soot aggregates

Claudia Marcolli¹, Fabian Mahrt^{2,3}, and Bernd Kärcher⁴

¹Department of Environmental System Sciences, Institute for Atmospheric and Climate Science, ETH Zurich, 8092 Zurich, Switzerland

²Department of Chemistry, University of British Columbia, 2036 Main Mall, Vancouver, BC, V6T 1Z1, Canada

³Laboratory of Environmental Chemistry, Paul Scherrer Institute, 5232 Villigen, Switzerland

⁴Institut für Physik der Atmosphäre, Deutsches Zentrum für Luft- und Raumfahrt (DLR Oberpfaffenhofen), 82234 Weßling, Germany

10 *Correspondence to:* Claudia Marcolli (claudia.marcolli@env.ethz.ch)

Abstract.

How ice crystals form in the troposphere strongly affects cirrus cloud properties. Atmospheric ice formation is often initiated by aerosol particles that act as ice nucleating particles. The aerosol-cloud interactions of soot and associated feedbacks remain uncertain, in part because a coherent understanding of the ice nucleation mechanism and activity of soot has not yet emerged.

15 Here, we provide a new framework that predicts ice formation on soot particles via pore condensation and freezing (PCF) that, unlike previous approaches, considers soot particle properties capturing their vastly different pore properties compared to other aerosol species such as mineral dust. During PCF, water is taken up below water saturation into pores on soot aggregates by capillary condensation. At cirrus temperatures, pore water can freeze homogeneously and subsequently grow into a macroscopic ice crystal. In the soot-PCF framework presented here, the relative humidity conditions required for these steps

20 are derived for different pore types as a function of temperature. The pore types considered here evolve from idealized stacking of equally sized primary particles, either in tetrahedral or cubic packing arrangements. Specifically, we encompass n -membered ring pores that form between n individual spheres within the same layer of primary particles as well as pores in the form of inner cavities that form between two layers of primary particles. We treat soot primary particles as perfect spheres and use the contact angle between soot and water (θ_{sw}), the primary particle diameter (D_{pp}) and the degree of primary particle

25 overlap (overlap coefficient, C_{ov}) to characterize soot pore properties. We find that n -membered ring pores are the dominant pore structures for soot-PCF, as they are common features of soot aggregates and have a suitable geometry for both, filling with water and growing ice below water saturation. We focus our analysis on three-membered and four-membered ring pores as they are of the right size for PCF assuming primary particle sizes typical for atmospheric soot particles. For these pore types, we derive equations that describe the conditions for all three steps of soot-PCF, namely capillary condensation, ice nucleation,

30 and ice growth. Since at typical cirrus conditions homogeneous ice nucleation can be considered immediate as soon as the water volume within the pore is large enough to host a critical ice embryo, soot-PCF becomes either limited by capillary condensation or ice crystal growth. For instance, our results show that at typical cirrus temperatures of $T = 220$ K, three-



35 membered ring pores formed between primary particles with $\theta_{sw} = 60^\circ$, $D_{pp} = 20$ nm, and $C_{ov} = 0.05$ are ice growth limited, as the ice requires a relative humidity with respect to ice of $RH_i = 137\%$ to grow out of the pore, while a sufficient volume of pore water for ice nucleation has condensed already at $RH_i = 86\%$. Conversely, four-membered ring pores with the same primary particle size and an overlap coefficient of $C_{ov} = 0.1$ are capillary condensation limited as they require $RH_i = 129\%$ to gather enough water for ice nucleation, compared with only 124% RH_i , required for ice growth. We use the soot-PCF framework to derive a new equation to parameterize of ice formation on soot particles via PCF. This equation is based on soot properties that are routinely measured, including the primary particle size and overlap, and the fractal dimension. These properties, along with the number of primary particles making up an aggregate and the contact angle between water and soot, constrain the parameterization. Applying the new parameterization to previously reported laboratory data of ice formation on soot particles provides direct evidence that ice nucleation on soot aggregates takes place via PCF. We conclude that this new framework clarifies the ice formation mechanism on soot particles at cirrus conditions and provides a new perspective to represent ice formation on soot in climate models.

45 1 Introduction

Incomplete combustion of biomass or fossil fuel produces copious quantities of soot particles, encompassing mixtures of black carbon and organic carbon that are of particular importance in the Earth's atmosphere. Soot particles influence atmospheric chemistry (Alcala-Jornod et al., 2000; Ammann et al., 1998; Andreae and Crutzen, 1997), and significantly contribute to air pollution, thereby negatively affecting human health (Bové et al., 2019; Janssen et al., 2012; Laumbach and Kipen, 2012). In addition, soot particles play an important role for climate directly through absorption and scattering of incoming shortwave radiation and indirectly by acting as ice nucleating particles (INPs) for clouds (Bond et al., 2013; Bond and Bergstrom, 2006; Ramanathan and Carmichael, 2008; Reddy and Boucher, 2007; Wang et al., 2014). Previous studies have found soot to be the second most important radiative forcing agent after carbon dioxide (Jacobson, 2001). However, owing to the complexity of the physicochemical properties of atmospheric soot particles, major gaps exist in our ability to quantify their impact on these various processes. A key example are the large uncertainties associated with aerosol-cloud interactions of soot that affect future climate projections (Bond et al., 2013). In particular, the ice nucleation activity of soot particles and their impact on cirrus clouds remain largely unconstrained.

The ice nucleation activity of soot particles has been shown to impact cirrus cloud coverage, emissivity and lifetime, thereby affecting the radiative balance (e.g. Lohmann, 2002; Lohmann et al., 2020; McGraw et al., 2020). Knowledge of the ice nucleation ability of soot particles is essential for estimating the anthropogenic influence on cirrus clouds (Kärcher, 2017; Penner et al., 2018; Zhao et al., 2019). For instance, the incomplete understanding of how aircraft-emitted soot particles nucleate ice crystals in cirrus clouds is the most uncertain component in assessing the climate impact of aviation (Lee et al., 2020). Such effects, if substantiated, are likely to become increasingly more important in view of the projected increase in global air traffic (ICAO Report, 2018).



65 There has been a considerable body of work aiming at understanding the ice nucleation activity of soot from different emission
sources and for different atmospheric conditions. These studies have found soot generally to be a poor ice nucleus above the
homogeneous nucleation temperature of supercooled liquid water $T > \text{HNT}$ (~ 235 K) and below water saturation (Chou et al.,
2013; DeMott, 1990; Dymarska et al., 2006; Friedman et al., 2011; Kanji and Abbatt, 2006; Mahrt et al., 2018; Möhler et al.,
2005a). Above (bulk) water saturation, water vapour can condense on the soot particles and they can act as INPs (Vali et al.,
70 2015) in the condensation/immersion mode. Since previous studies have reported no or only weak ice nucleation activity for
soot at $T > \text{HNT}$ and relative humidities with respect to water (RH_w) above 100 % (Chou et al., 2013; DeMott, 1990; Diehl
and Mitra, 1998; Gorbunov et al., 1998, 2001; Kireeva et al., 2009; Schill et al., 2016) the importance of soot to nucleate ice
in mixed-phase clouds (MPC) is most likely negligible (Kanji et al., 2020; Schill et al., 2016, 2020a; Vergara-Temprado et al.,
2018), given the abundance of other, more efficient INPs at these conditions. At $T \leq \text{HNT}$, on the contrary, studies have
75 reported soot to nucleate ice well below relative humidities required for homogeneous freezing of solution droplets (Crawford
et al., 2011; Ikhenazene et al., 2020; Koehler et al., 2009; Kulkarni et al., 2016; Mahrt et al., 2018; Möhler et al., 2005a, 2005b;
Nichman et al., 2019; Zhang et al., 2020). These results indicate that soot particles could represent an eminent source of INPs
at upper tropospheric conditions, with potentially important implications for cirrus cloud formation and climate. At the same
time, field studies have reported soot to be largely absent in cirrus cloud residuals (Cziczo et al., 2013; Cziczo and Froyd,
80 2014). While the latter could be partially influenced by the lower size limit of $\sim 0.2 \mu\text{m}$ of the mass spectrometer deployed
(Cziczo et al., 2006), these contrary conclusions reveal that the ice nucleation ability of soot is insufficiently understood to
date.

The recent studies by Nichman et al. (2019) and Mahrt et al. (2018) have demonstrated that for $T < \text{HNT}$, ice nucleation via
pore condensation and freezing (PCF, Christenson, 2013; David et al., 2019, 2020; Fukuta, 1966; Higuchi and Fukuta, 1966;
85 Marcolli, 2014) is the prevailing mechanism of ice formation on bare, uncoated soot particles, but can be hampered if the pores
are covered by hydrophobic material (Mahrt et al., 2020a; Zhang et al., 2020). During PCF, water uptake into pores and cavities
due to capillary condensation is followed by ice nucleation of the pore water and growth of the ice out of the pores resulting
in macroscopic ice crystals. While PCF is recognized to have the potential to explain the disparate ice-nucleation ability of
soot at mixed-phase compared to cirrus cloud conditions, previous studies have not taken the specific characteristics of soot
90 particles into account to obtain a more coherent understanding of its ice nucleation pathway. A common property of all soot
particles is their fractal morphology, with soot aggregates being composed of graphitic primary carbon spherules that cluster
together (Park et al., 2004; Samson et al., 1987). Such sintered primary particles provide ample pore structures (Rockne et al.,
2000), where water can condense. The equilibrium water vapour pressure over such capillary condensates, forming a concave
water surface, is reduced compared to bulk water, as described by the Kelvin equation (e.g. Fisher et al., 1981; Marcolli, 2014,
95 2020). Therefore, water can be taken up already at $RH_w < 100$ %. Evidence of PCF being the dominant ice formation
mechanism on soot is a sharp, almost step-like increase in the ice fraction at $T < \text{HNT}$ and below water saturation, as reported
by Mahrt et al. (2018). Such a distinct increase cannot be explained by classical nucleation theory (CNT) and assuming ice
formation to proceed via deposition nucleation, where a liquid phase is absent (David et al., 2019; Welti et al., 2014). Besides



soot, PCF was recently also observed to cause ice formation on other combustion particles such as coal fly ash (Kilchhofer et al., 2020; Umo et al., 2019).

In general, PCF is controlled by the contact angle (θ) defining the interface of soot and water (or ice) as well as the pore diameter and geometry (David et al., 2020; Fukuta, 1966; Marcolli, 2017b, 2020). The contact angle denotes the wettability of a (soot) particle surface (Lohmann et al., 2016; Pruppacher and Klett, 1997). Recent work has shown that the contact angle can play a relevant role in controlling the capillary uptake of water and thus ice formation in cylindrical pores with diameters between 2.5 nm to 9.1 nm (David et al., 2020). However, given the heterogeneity in the physical (pore size and geometry) and chemical (contact angle) properties of soot particles from different combustion sources, undergoing different aging processes, their ability to nucleate ice via PCF may vary strongly. Previous studies have focussed on using the PCF framework to predict capillary condensation and subsequent homogeneous freezing of pore water in simple pore geometries, including cylindrical pores (Marcolli, 2014) and more recently also conical and wedge-shaped pores (Marcolli, 2020). Such geometries are believed to be representative for cavities and pores found on mineral dust particles (e.g. Kiselev et al., 2016). As the conditions of capillary condensation depend on pore geometry and contact angle, neglecting the pore shape and wettability of (atmospheric) soot aggregates to predict PCF is too simplistic. Here, we develop a new theoretical framework to explore and constrain PCF on soot aggregates, capturing their vastly different pore properties compared to other aerosol species such as mineral dust. Specifically, we extend the previous work by Marcolli (2020) to pores formed between sintered primary soot particles and systematically investigate the effect of the contact angle, following earlier work on capillary condensation in soot aggregates by Persiantseva et al. (2004). Based on the physical properties of soot, we derive a new framework to predict the ice nucleation ability of soot particles resulting from PCF that fits experimental results from previous laboratory measurements (Mahrt et al., 2018, 2020b). The PCF-based parameterizations derived from this framework are able to predict the ice activated fraction (AF) of soot particles, ultimately improving parameterizations (e.g. Ullrich et al., 2017) currently used in climate models to simulate their effects on cirrus clouds and associated feedbacks.

2 Soot properties

Soot forms aggregates that are composed of primary carbon spheres, characterized by an onion-shell structure of folded graphite sheets, typically having diameters D_{pp} between 10 to 45 nm, but they can also reach larger values (e.g. Kim et al., 2001; Liati et al., 2014; Megaridis and Dobbins, 1990; Wentzel et al., 2003). The primary particles coagulate to form soot clusters that grow further in size into soot aggregates as a result of monomer-cluster or cluster-cluster collision. Sizes of ambient soot aggregates range from a few primary particles to larger, fractal aggregates with tens to hundreds of primary particles, depending on the combustion source and conditions (Sorensen, 2011; Wentzel et al., 2003), with diameters typically ranging from 0.01 to 1 μm (Ogren and Charlson, 1983; Rose et al., 2006), but can also reach larger values depending on the source and atmospheric trajectory (e.g. Okada et al., 1992). Over the past, considerable efforts have been made to characterize soot from different combustion sources and conditions, and to quantify morphological parameters such as the mobility



diameter, D_m , the primary particle diameter, D_{pp} , and the primary particle overlapping coefficient, C_{ov} . The early studies by Hees and McDonald (1983), Samson et al. (1987), and Megaridis and Dobbins (1990) have set the stage to investigate the morphology of soot aggregates using transmission electron microscopy (TEM), followed by studies of e.g. Köylü et al. (1995, 1995; 1992) and Sorensen et al. (1992). More recently, automated algorithms have emerged that can measure morphological parameters such as the primary particle diameter from TEM images of soot (Anderson et al., 2017; Bescond et al., 2014; Dastanpour et al., 2016; Grishin et al., 2012). Given the large availability of TEM-based information on primary particle size and overlapping coefficients, we make these parameters a central part of our soot-PCF framework presented here. Relevant properties for PCF are pore shape, size, and the contact angle between the pore surface with water and ice. In the following, we discuss these particle properties with respect to atmospheric soot. In our soot-PCF framework we assume that pores form between spherical primary particles and that their size and shape depend on the arrangement of the primary particles, their respective size and the overlap between primary particles. In turn, the number of pores in a soot aggregate depends on the number of primary particles in the aggregate and their compaction, i.e. fractal dimension.

2.1 Primary particle size

Ambient soot aggregates typically consist of primary particles with diameters of one to a few tens of nanometers that are close to spherical shape. The size of the primary particles depends on the emission source, as well as the fuel type and the combustion conditions. Relevant combustion conditions that influence the primary particle diameter include the fuel to air (oxygen) ratio during combustion, the flame temperature and the residence time within the flame. Previous studies have investigated the primary particle diameter of soot particles from various emission sources, including car engines (e.g. Burtscher, 2005; Ferraro et al., 2016; Smekens et al., 2005; Su et al., 2004), aircraft turbines (e.g. Delhaye et al., 2017; Liati et al., 2014, 2019; Marhaba et al., 2019; Smekens et al., 2005), and commercial carbon blacks and/or soot generated from controlled flames in the laboratory (e.g. Clague et al., 1999; Cortés et al., 2018; Ferraro et al., 2016; Megaridis and Dobbins, 1990; Ouf et al., 2016, 2019). For instance, Liati et al. (2014) used TEM to investigate the size of primary particles of a turbofan engine (type CFM 56-7B26/3), frequently used in Boeing 737 aircrafts that was operated with standard Jet A-1 fuel. They reported the primary particle diameter to increase with increasing thrust level. At 100 % thrust, typical for take-off conditions, the majority of primary particles (~60 %) had diameters between 10 and 25 nm, with a mode of 24 nm and 52 % of the particles being larger than 20 nm. At cruise conditions, equivalent to a thrust level of 65 %, the average size of the primary particles was smaller, with a mode diameter of 20 nm and the majority of particles (75 %) in the range between 10 and 25 nm. At 7 % thrust, corresponding to taxiing, the mode was decreased to 13 nm with most particles (99 %) being in the range between 5 and 20 nm. The trend of increasing primary particle diameters with increasing thrust levels is consistent with other studies of aircraft soot emissions (Delhaye et al., 2017; Liati et al., 2019; Marhaba et al., 2019). In their detailed TEM characterization of aircraft soot from the same engine type, Liati et al. (2019) also investigated the effect of fuel type on the soot morphology. This was achieved by comparing the primary particle size when burning standard Jet A-1 fuel and a blend of the same fuel along with 32 % hydro-processed esters and fatty acids (HEFA) biofuel, and analyzing soot aggregates collected at thrust levels of 85 %



(climbing conditions) and 4 % (idle conditions). Their results reveal that the biofuel blend leads to smaller primary particles
165 at both thrust levels compared with standard kerosene. This finding is consistent with Moore et al. (2017), who reported a
reduction towards smaller primary particle diameters of 3–5 nm, for the number size distributions sampled at cruise conditions
behind a turbofan engine (CFM56-2-C1) fed with a 1:1 mixture of standard Jet A-1 fuel and HEFA biofuel, compared to when
operating the engine on pure Jet A-1 fuel. Nonetheless, the results of Liati et al. (2019) revealed that the majority of particles
(75–85 %) had diameters between 5 and 10 nm at idle conditions, and 60 % of the primary particles was found to have
170 diameters between 15 and 20 nm at 85 % thrust, independent of the fuel type. These values are in good agreement with those
reported by Delhaye et al. (2017), who found a mean primary particle diameter of 15 nm, with extreme values of 4 nm and 70
nm, when testing a turbofan engine (Snecma/NPO-Saturn SaM146-1S17) over different thrust levels ranging from 7 % to 100
%.

There are also many measurements published of primary particle sizes from vehicle emissions. For instance, Su et al. (2004)
175 used TEM to investigate the primary particle sizes of an Euro IV diesel engine. They reported a mean primary particle diameter
of 13 nm, which was found to be significantly lower compared to the mean primary particle diameter of 35 nm for soot particles
from older engines reported in the same study. The latter is consistent with the value of 30 nm for the mean primary particle
diameter determined for diesel (VW Golf) soot particles, at idle and full speed conditions (Smekens et al., 2005), which
compares well with previously reported values for diesel soot (Amann and Sieglä, 1981; Bérubé et al., 1999; Roessler, 1982).
180 Similar to the observations for aircraft soot, Smekens et al. (2005) reported smaller primary particles when the car was operated
with biodiesel, namely 29 nm (idle) and 26 nm (full speed). More recently, Ferraro et al. (2016) sampled soot particles from a
diesel car engine (Peugeot DV4) drained from the engine oil and reported the majority of particles (91.3 %) to have a mean
primary particle diameter of 25.4 nm, while some particles (8.7 %) had primary particle diameters of 48 nm.

Over the past, many laboratory sources have been developed with the goal to provide relevant analogues for atmospheric soot
185 particles from e.g. car or aircraft engines. In these burners the combustion conditions can be varied in a controllable manner
to generate soot with primary particle diameters between approximately 5 nm to 50 nm (e.g. Cortés et al., 2018; Megaridis and
Dobbins, 1990; and references therein), i.e. covering the size range relevant for ambient soot. Overall soot particles emitted
from different sources and using different fuel types, and engine operating conditions have comparable but not identical
primary particle sizes. In the following, we encompass the relevant range of primary particle sizes and focus our discussion on
190 $10 \text{ nm} \leq D_{pp} \leq 30 \text{ nm}$.

2.2 Overlap between primary particles

The primary particles constituting a soot aggregate are typically not in point contact but overlap partially. Overlap between
primary particles is sometimes referred to as sintering or necking and can result from various processes. For instance, adjacent
monomers can merge (overlap) in high-temperature environments of the flame resulting from a lack of particle rigidity. As
195 another example, primary particles can overlap due to strong attraction forces between them (Brasil et al., 2000). Yet, overlap
can also result from an overall physical compaction of soot aggregates, e.g. during cloud processing (e.g. Bhandari et al., 2019;



China et al., 2015; Mahrt et al., 2020b). The degree by which neighbouring primary particles overlap can be quantified by the overlapping parameter, C_{ov} , introduced by Brasil et al. (1999):

$$C_{ov} = \frac{D_{pp} - D_{ij}}{D_{pp}}, \quad (1)$$

where D_{ij} denotes the distance between the centres of two overlapping/intersecting spheres with diameter D_{pp} . When two adjacent primary particles are in point contact $C_{ov} = 0$, whereas $C_{ov} = 1$ describes the other extreme for two completely overlapping primary particles. Previous studies have reported values for C_{ov} to typically range within 0.05 and 0.29 (Brasil et al., 1999; Ouf et al., 2010, 2019; Wentzel et al., 2003). Wentzel et al. (2003) found values between 0.1 and 0.29 for soot aggregates from diesel emissions. As another example, Cortés et al. (2018) reported values of $0.04 \leq C_{ov} \leq 0.18$ when using TEM to study soot aggregates generated in co-flow diffusion flames using different fuels (ethylene, propane and butane), which is in good agreement with the values (0.11–0.17) of soot aggregates derived from diffusion flames reported in Ouf et al. (2019). The overlap of primary particles in soot aggregates has gained attention because it impacts the radiative properties of the aggregates (e.g. Yon et al., 2015). Below, we demonstrate that C_{ov} also impacts the pore geometry and hence the ability of ice to form via PCF in soot aggregates.

2.3 Soot aggregate size and compaction

A large body of work has been devoted to elucidating the size of soot aggregates from various emission sources, including car engines (e.g. Clague et al., 1999; Harris and Maricq, 2001, 2002; Karjalainen et al., 2014), aircraft turbines (e.g. Delhaye et al., 2017; Lobo et al., 2015; Masiol and Harrison, 2014; Moore et al., 2015), as well as commercial and laboratory generated soot (e.g. Han et al., 2012). For instance, Kinsey et al. (2010) observed the mean soot aggregate diameter to increase from approximately 10 nm to 35 nm, when increasing the thrust from 7 % to 100 %, when sampling engine exhaust plumes during the aircraft particle emission experiments (APEX). Note that this range overlaps with the size range of primary particles rendering it likely that reported sizes refer in the lower limit to single primary particles rather than to aggregates. Similarly, Delhaye et al. (2017) reported the modal diameter of the soot number size distribution of particles emitted from a turbofan aircraft engine (SaM146-1S17) to range from 17 nm to 55 nm, when testing the emissions according to the ICAO Landing and Take-Off (LTO) cycle, corresponding to thrust levels of 7 %, 30 %, 85 % and 100 %. This range is consistent with other measurements (e.g. Liati et al., 2019; Lobo et al., 2015; Mazaheri et al., 2009; Moore et al., 2017). As another example, Mazaheri et al. (2009) investigated aircraft emissions during take-off and landing for four different aircraft engine types and found the majority of the soot to have diameters smaller than 30 nm, with a secondary mode being centred between 40 nm and 100 nm. This secondary mode is in-line with the measurements by Herndon et al. (2008), who observed a mode between 60 nm to 80 nm during take-off. Similar to the primary particle diameter, the soot aggregate size is sensitive to the operation conditions, with larger aggregates being observed at climb conditions compared to idle conditions. For instance, Liati et al. (2019) found 80 % of the aggregates to be smaller than 40 nm in diameter at idle conditions, while at an engine thrust of 85 %, a modal diameter between 40 to 80 nm was observed, accounting for approximately 35 % of the total particles, while 20 %



of the aggregates had diameters between 80 nm to 120 nm and the remaining fraction was larger than 120 nm. Overall, diameters of soot particles (comprising individual primary particles and aggregates) emitted from aircraft engines are mostly
230 in the range between 5 and 100 nm, even though some studies have also reported larger soot aggregates in e.g. contrail residuals (Petzold et al., 1998; Twohy and Gandrud, 1998). Comparable values have been reported for soot emitted from gasoline and diesel vehicles. Number size distributions of particulate matter from vehicle exhaust usually reveal a clear bimodality, with the maximum particle concentration observed in the nucleation mode and the secondary peak located in the accumulation mode.

235 For emissions from diesel engines the mean soot aggregate diameter for the accumulation mode particles is almost always within the range between 60 nm to 120 nm, and is well represented by lognormal distributions with geometric standard deviations of 1.8–1.9 (Burtcher, 2005; Harris and Maricq, 2001). Furthermore, diesel soot aggregate sizes have been reported to be largely independent of the size and type of the engine, as well as the operation conditions (Burtcher, 2005). Soot aggregates from gasoline vehicles are generally smaller and number size distributions tend to be more asymmetric (Harris and
240 Maricq, 2001). Karjalainen et al. (2014) observed a bimodal size distribution for particles emitted from gasoline vehicles, with the modes corresponding to mean diameters below 30 nm and 70 nm, respectively, including small almost spherical soot particles and larger agglomerated soot particles. The latter value falls well within the range between 40 nm to 80 nm reported previously (Harris and Maricq, 2001). Some studies have also reported diesel soot aggregates significantly larger than 200 nm diameter, even reaching supermicron sizes (Hoard et al., 2013). Such particles likely result from flaking particle deposits that
245 build up within the combustion chamber or the exhaust pipe. However, given that such larger particles should be more easily captured by exhaust filters, renders their atmospheric relevance questionable.

In the discussion above, the reported sizes are mostly reported as electrical mobility diameters, D_m , of soot aggregates but comprise in the limit to small sizes also D_m of individual primary particles that have not undergone any aggregation. Only few studies have investigated the relation between the aggregate size and the primary particle size. For instance, Dastanpour and
250 Rogak (2014) reported a positive correlation between primary particle and aggregate size, with larger aggregates containing larger primary particles, based on a TEM analysis of soot from various combustion sources, including particles sampled from aircraft jet engines. The same study revealed that within an individual aggregate, the primary particle size is more uniform compared to an ensemble of aggregates. A similar trend between primary particle size and aggregate size was suggested by Olfert et al. (2017), which can have important implications for the pore number, size and type that can form on individual soot
255 aggregates. Based on these results, Olfert and Rogak (2019) have demonstrated that the primary particle size increases with aggregate size, following a universal scaling law ($D_{pp} \sim D_m^{0.35}$), that is valid for a wide range of soot particles/sources.

2.4 Contact angle

The contact angle of soot particles with a water droplet is a measure to quantify the hydrophilicity/wettability of the particle surface. The maximum contact angle of $\theta_{sw} = 180^\circ$ (non-wetting case) represents the situation of a free spherical water droplet
260 in point contact with the soot substrate. In contrast, if the soot particle were completely covered by a water layer (complete



wetting case), the contact angle between the soot particle surface and the water droplet becomes $\theta_{sw} = 0^\circ$ (Lohmann et al., 2016). For capillary condensation taking place below bulk water saturation, soot-water contact angles below 90° are required, because only if $\theta_{sw} < 90^\circ$, the capillary water exhibits a concave curvature, implying an equilibrium vapour pressure that is above that of bulk water. Early work by Fowkes and Harkins (1940) reported values of $85.3\text{--}85.9^\circ$ for θ_{sw} , which are in good agreement with the values of $\theta_{sw} = 83.9^\circ$, measured by Morcos (1972). However, soot derived from different combustion sources and having undergone different kinds and degrees of atmospheric processing can span a wide range of contact angles. For instance, highly ordered pyrolytic graphite, has been reported to have soot-water contact angles in the range of $75\text{--}91^\circ$ (Shin et al., 2010; Westreich et al., 2007). Persiantseva et al. (2004) investigated the soot-water contact angle for different surrogates of aviation soot, using the sessile drop technique. They tested aircraft combustor soot (AEC) by operating a gas turbine (D30-KU) in an engine test stand (Popovitcheva et al., 2000). When simulating cruise conditions and using TS1 kerosene as fuel, they found $\theta_{sw} = 63^\circ$ for freshly emitted soot. Persiantseva et al. (2004) also investigated soot derived from burning different types of aviation fuels (German kerosene, TC1 and T6) in an oil lamp and reported the soot-water contact angles to range between 70° and 80° , demonstrating that the fuel composition can strongly impact the contact angle of the resulting combustion particles. A lower contact angle than from aviation fuel of $\theta_{sw} = 59^\circ$ was found for lamp black soot, derived from burning lantern fuel in an oil lamp (Persiantseva et al., 2004). Interestingly, Persiantseva et al. (2004) found θ_{sw} to decrease by 17° for TC1 soot, after heating the sample at 300°C for 30 min. An even more pronounced decrease of 35° from the original value was found when outgassing the kerosene soot for 18 h at 200°C , leading to values of $\theta_{sw} = 43^\circ$, which was attributed to a loss of semi-volatile organics and a change in surface composition. This is in good agreement with earlier work demonstrating contact angles on graphite to be as low as $35 \pm 4^\circ$, after evacuating the sample to 10^{-10} Torr, compared to values between 50 to 80° found for the untreated (0001) graphite surface (Schrader, 1975). These results are supported by more recent findings demonstrating that contamination e.g. in the form of hydrocarbon adsorption on the soot particle surface can increase the soot-water contact angle (e.g. Kozbial et al., 2016; Martinez-Martin et al., 2013). Proxies for soot particles from aviation emission were also studied by Kireeva et al. (2009). When burning TS1 kerosene in an oil lamp (diffusion flame), a contact angle of $\theta_{sw} = 59^\circ$ was found. In the same study, Kireeva et al. (2009) also investigated different commercial carbon blacks (lamb black, furnace black, channel black, thermal black, acetylene soot). Using the sessile drop technique, they found contact angles to range from 32° to 47° . Han et al. (2012) investigated the influence of the combustion condition (fuel to oxygen ratio) on the hydrophilicity of laboratory soot surrogates, encompassing particles derived from *n*-hexane, decane and toluene diffusion flames. At fuel-rich burning conditions values of approximately $\theta_{sw} = 120^\circ$ were found, largely independent of the soot type. While the hydrophilicity of toluene was found to be almost insensitive to the fuel to oxygen ratio, the contact angles of *n*-hexane and decane flame soot significantly decreased under fuel-lean conditions, reaching values of 83° . This value is comparable to that observed by Zelenay et al. (2011), reporting $\theta_{sw} = 80 \pm 3^\circ$ for untreated soot produced with a combustion aerosol standard (CAST; under fuel-lean conditions). Interestingly, Zelenay et al. (2011) reported an increase in soot-water contact angle for the CAST soot after exposure to ozone ($\theta_{sw} = 100 \pm 4^\circ$) and ozone and UV-light ($\theta_{sw} = 120 \pm 3^\circ$). These results are in stark contrast to the findings of Wei et al. (2017), who reported a decrease in contact angle due to ozone



295 aging. In their study, they took soot particles from a wood-burning fireplace, different bus engines and a kerosene lantern and aged the pelletized soot by exposure to vapours of ozone, sulfuric acid and nitric acid. They reported the contact angles of fresh, untreated soot to be between 65° to 110° . After 10 days of exposure to 40 ppb ozone all samples revealed a decrease in contact angle up to $\sim 15^\circ$. Aging with nitric acid and sulfuric acid was reported to be less effective.

This survey reveals that contact angles between atmospheric soot particles and water cover a wide range with highest values for fresh soot from fuel-rich flames, which are clearly hydrophobic ($\theta_{sw} > 90^\circ$), and lowest values after strong evacuation ($\theta_{sw} \approx 35^\circ$). Given this wide range, the soot-water contact angle is a highly relevant parameter that strongly affects the efficiency of soot-PCF or even renders it irrelevant (if $\theta_{sw} > 90^\circ$). For simplicity, we assume in this study that the surface of an individual soot aggregate has a uniform contact angle with water and ice.

3 Morphology and pore structure of model soot aggregates

305 To characterize and model the features of soot aggregate porosity, we treat the primary particles as perfect spheres of diameters D_{pp} and allow them to partially overlap as quantified by the overlap coefficient C_{ov} . In order to derive pore structures relevant for PCF, we assume that the primary particles enclosing one specific pore are of uniform size and equal overlap, i.e. one D_{pp} and C_{ov} . Using the concept of grain packing, the primary particles can be stacked in different packing arrangements such as tetrahedral and cubic as shown in Fig. 1a and d. In this study, we use these two packing arrangements and investigate the ability of the associated pore types to form ice via PCF.

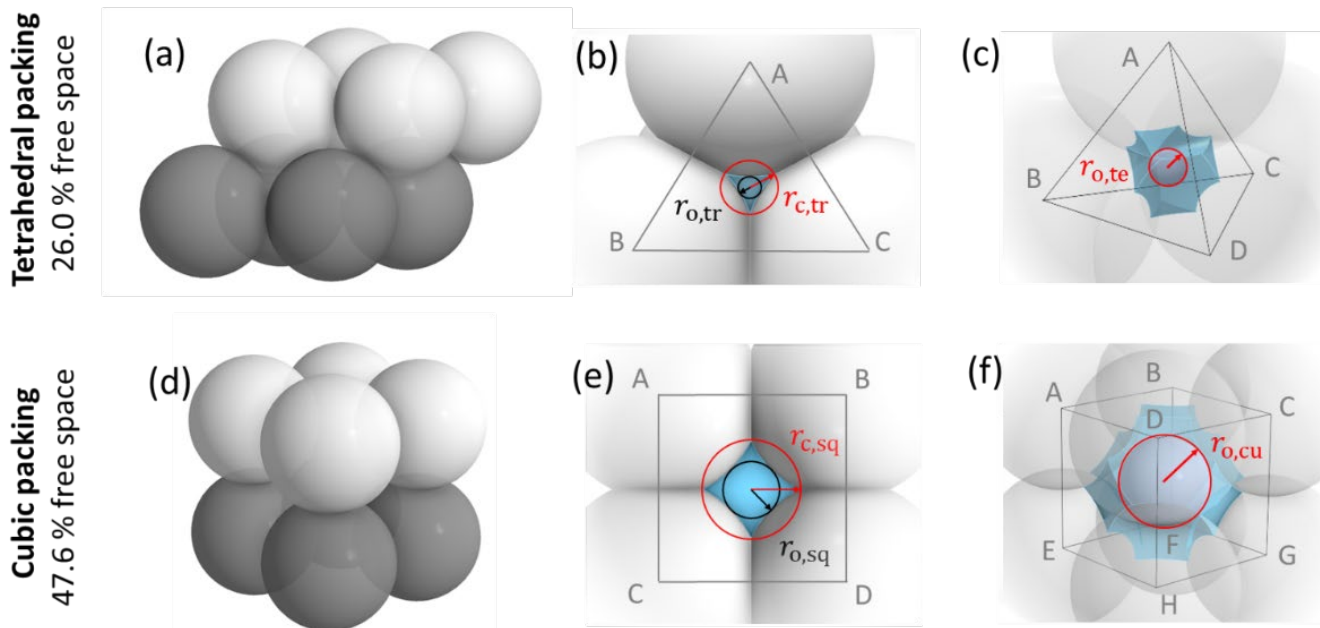
Figure 1 illustrates the pores arising from tetrahedral and cubic packing arrangements. Different types of pores form within one lattice layer or plane of spheres and between two overlaying planes of spheres. Within a single plane, pores form as the annular (ring-like) opening between the three spheres arranged on the corners of the equilateral triangle ABC in the case of the tetrahedral packing arrangement. This pore has the shape of a *concave triangle* (Fig. 1b), and we refer to these voids as *three-membered ring pores*. The dimensions of the three-membered ring pore relevant for PCF are the circumcircle radius, $r_{c,tr}$, and the radius of the circle describing the opening of the concave triangle, $r_{o,tr}$. In the case of the cubic packing arrangement the pore within a single plane is formed as the opening between the four spheres arranged on the corners of the square ABCD and therefore has the shape of a *concave square* (Fig. 1e). We refer to these voids as *four-membered ring pores*. The dimensions relevant for PCF are the circumcircle radius, $r_{c,sq}$, and the radius of the circle describing the opening of the concave square, $r_{o,sq}$. Ring pores are narrowest at the midplane formed by the centres of the spheres making up the ring, and widen with increasing distance from the midplane. In the following, we refer to the narrowest part of the pore as pore neck.

Larger pores form between two overlaying planes of primary particles. In the case of tetrahedral packing, a pore of the shape of a dented, *concave octahedron* forms between four primary particles arranged on the corners ABCD of a regular tetrahedron (Fig. 1c, Fig. A 1b). The four openings of the cavity within the tetrahedral cell, form the three-membered ring pores described above. Its free space can be quantified by the radius of the maximum sphere within it, denoted by $r_{o,te}$. In the case of a cubic arrangement, the inner pore between eight spheres (A–H) across two lattice layers of primary particles has the form of a dented,



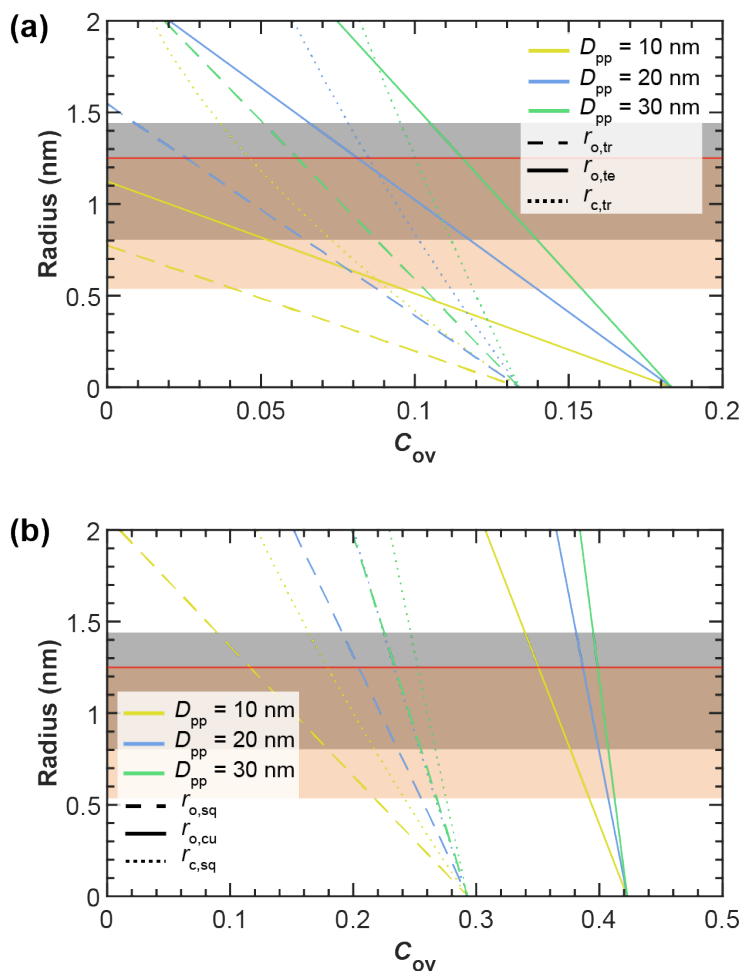
concave cube. Its free space can be quantified by the radius of the maximum sphere within it, denoted by $r_{o,cu}$. The cube formed between the eight primary particles has six openings on the faces of the cube, forming four-membered ring pores (Fig. 1f, Fig. A 2b). A detailed description of the pore geometry along with a derivation of the relevant pore dimensions is given in Appendix A. In Fig. 2, we show the relevant pore dimensions for pores formed between primary particles depending on primary particle diameter, D_{pp} and overlap, C_{ov} . In general, pore radii increase in size with increasing diameters of the primary particles for both the tetrahedral and cubic packing arrangement. In the absence of overlap, pores are very open and become more constrained (narrow) with increasing overlap, thus improving their ability to host water on one hand and reducing the enclosed water volume on the other hand. The overlap at which pores vanish is independent of primary particle diameter (D_{pp}) and just depends on the pore geometry. The opening of the three-membered ring pore vanishes, i.e. $r_{o,tr} = 0$, for $C_{ov} = 0.134$ (dashed lines in Fig. 2a). Conversely, the concave octahedron within the tetrahedral cell persists to $C_{ov} = 0.184$ (solid lines in Fig. 2a), yet, without connection to the surrounding for $C_{ov} > 0.134$, since at this overlap the three-membered ring pores forming the openings of the concave octahedron vanish. For the cubic arrangement, larger overlaps are required for both pore types to disappear compared to the tetrahedral packing arrangement. Specifically, the opening of the four-membered ring pore vanishes for $C_{ov} = 0.293$ ($r_{o,sq} = 0$, dashed lines in Fig. 2b) and the concave cube within the cubic cell vanishes only for $C_{ov} = 0.423$ ($r_{o,cu} = 0$, solid lines in Fig. 2b), as detailed in Appendix A.

In order to contribute to ice formation via PCF, pores need to be small enough to allow water uptake below water saturation and large enough to host a critical embryo along with pore openings that are sufficiently large to allow ice growth out of the pore, so that macroscopic ice crystals can form. In the following, we first derive the size of a critical ice cluster and set it in relation to the pore dimensions shown in Fig. 2. This forms the baseline constraint for any soot pore to be ice active via PCF. We then go on and derive conditions for pore filling and discuss the growth of ice out of the pore.



350

Figure 1: Overview of tetrahedral (a) and cubic (d) packing arrangements along with theoretical porosities when ordering uniform sized spheres into a cubic unit cell, defined as the volume of the voids to the total volume of the sample unit cell. The porosity refers to zero overlap between rigid spheres and is independent of sphere size. Differently coloured spheres indicate spheres in different lattice planes of the arrangements. Panels (b) and (e) present a zoom of the three-membered and four-membered ring pores along with key pore dimensions relevant for PCF and as discussed in the text. Panels (c) and (f) reveal the inner cavities forming a concave octahedron (tetrahedral packing) and concave cube (cubic packing). Please see Figs. A1 and A2 for a more detailed view of panels (c) and (f).



355 **Figure 2:** Overview of the radii of key pore dimensions (see Fig. 1) formed in pores of (a) tetrahedral and (b) cubic packing arrangements
 between equally sized spherical primary particles of indicated diameter, and as a function of primary particle overlap, C_{ov} as defined in Eq.
 (1). A derivation of the indicated pore dimensions can be found in Appendix A. For comparison, the grey and orange shaded regions mark
 the variation of the critical ice embryo radius, r_{crit} , for $200\text{ K} < T < 235\text{ K}$, as calculated based on Eq. (3) using the parameterizations of
 Murray et al. (2010) and Ickes et al. (2015), respectively. The red horizontal line denotes a pore radius of $r = 1.25\text{ nm}$, corresponding to the
 360 smallest investigated pore size, for which ice formation was experimentally observed by David et al. (2020).

4 Ice nucleation in soot pores

4.1 Critical pore size for PCF

The nucleation of the thermodynamically stable phase (ice) within a metastable phase (supercooled liquid water) can be
 described by classical nucleation theory (Farkas, 1927; Fletcher, 1960; Gibbs, 1875). CNT assumes a spherical shape of the
 365 critical ice cluster (ice embryo), because a sphere minimizes the surface area for a fixed volume (Fukuta, 1966; Zaragoza et



al., 2015). CNT describes the change in Gibbs free energy, $\Delta G_{w,i}(T,P)$ for the formation of a critical embryo as the sum of the volume energy released by passing from the thermodynamically metastable liquid to the stable ice phase and the surface energy consumed by forming a new interface (Lohmann et al., 2016; Pruppacher and Klett, 1997):

$$\Delta G_{w,i}(T,P) = \underbrace{\frac{4\pi r^2 \gamma_{iw}(T,P)}{\text{Surface energy}}}_{\text{Surface energy}} + \underbrace{\frac{4\pi r^3}{3v_i(T,P)} \Delta\mu_{iw}}_{\text{Volume energy}}. \quad (2)$$

We include here the absolute pressure dependence, as large negative pressures can be reached in narrow pores below water saturation with strong impact on homogeneous ice nucleation rates (Marcolli, 2020). Here, $\gamma_{iw}(T,P)$ denotes the interfacial tension between the ice and the water phase, r is the radius of the evolving ice cluster, $v_i(T,P)$ is the molecular volume of water in the ice phase, and $\Delta\mu_{iw} = \mu_i(T,P) - \mu_w(T,P)$ represents the difference between the chemical potentials of ice and liquid water. Subcritical ice clusters randomly form within the supercooled liquid and grow continuously once they have passed the critical size (Lohmann et al., 2016). The critical radius $r_{\text{crit}}(T,P)$ of an ice embryo is reached when growth and shrinkage both lead to a decrease of the Gibbs free energy and can be determined by setting $\delta\Delta G_{w,i}(T,P)/\delta r = 0$:

$$r_{\text{crit}}(T,P) = \frac{2\gamma_{iw}(T,P)v_i(T,P)}{-\Delta\mu_{iw}}. \quad (3)$$

The critical embryo radius decreases with decreasing temperature and pressure. Moreover, values depend on the CNT parameterization applied. It ranges between $r_{\text{crit}} = 0.53$ nm at ice saturation ($P = -55$ MPa) at 200 K to $r_{\text{crit}} = 1.25$ nm at water saturation ($P = 0.1$ MPa) at $T = 235$ K, using the pressure dependent parameterization from Ickes et al. (2015) as described in Marcolli (2020). Using the pressure dependent CNT parameterization by Murray et al. (2010) with $n = 0.97$, instead, the range changes to $r_{\text{crit}} = 0.8$ nm at ice saturation at 200 K and $r_{\text{crit}} = 1.43$ nm at water saturation at 235 K (Marcolli, 2020). In Fig. 2, we show these ranges of critical ice embryo radii as shaded regions.

For a soot pore to be suitable for PCF, it must be large enough to host a spherical ice embryo of critical size. Comparison of the critical embryo size with the radii of the different pore types shown in Fig. 2 demonstrates that the pores of soot aggregates with atmospherically realistic primary particle diameters ranging from 10 to 50 nm are sufficiently large to accommodate a critical ice embryo. In particular, it becomes evident that for pores formed in the tetrahedral arrangement low overlap is required to be relevant for PCF. As the overlap coefficient increases, the pores quickly become too narrow (falling outside the shaded region in Fig. 2) to host an ice embryo. Note, that even though the inner cavity within four tetrahedrally arranged spheres is large enough to host a critical embryo, its openings given by the three-membered ring pores may be too small to allow macroscopic ice growth out of the pore. Moreover, a quasi-liquid layer has been shown to form between ice and the pore surface, which further increases the pore size required to host a critical ice embryo. This surface layer thickness has been quantified as about 0.7 nm in narrow (3.2–4.8 nm diameter) hydrophobic cylindrical pores at 200 K (Morishige, 2018), while molecular simulations yielded a half width of 0.37 nm for the water layer adjacent to the hydrophobic surface of cylindrical pores at $T = 190$ K (Moore et al., 2012). Yet, the ability of very narrow pores to host ice has been supported by David et al. (2020), who observed ice growth out of methylated silica particles with average pore diameters of 2.4 nm for temperatures of 223 and 228 K.



Another important aspect to be recognized from Fig. 2 is that the three-membered and four-membered ring pores characterized by $r_{o,lr}$ and $r_{o,sq}$ are sufficient by themselves to host a critical ice embryo. In other words, the relatively larger inner cavities denoted by the concave octahedron (tetrahedral packing) and the concave cube (cubic packing) do not need to fill in order for a soot aggregate to be ice active. We therefore concentrate in the following on n -membered ring pore structures formed by soot aggregates with the main focus on three-membered and four-membered ring pores.

4.2 Nucleation rates at cirrus conditions

Even if a ring pore is wide enough to host ice, the pore water remains liquid when the ice nucleation rate is too low. As soot is a poor ice nucleator in immersion mode (Kanji et al., 2020), we exclude here the possibility of heterogeneous freezing and assume that the pore water needs to freeze homogeneously to form ice via soot-PCF. Numerous experimental studies on micrometre-sized droplets have constrained homogeneous ice nucleation rates in the temperature range from 234 to 238 K to values below $10^{11} \text{ cm}^{-3} \text{ s}^{-1}$ (e.g. Ickes et al., 2015 and references therein). Few experimental studies have explored homogeneous ice nucleation rates at lower temperatures by investigating the freezing of water clusters with radii of a few nanometres (Amaya and Wyslouzil, 2018; Bartell and Chushak, 2003; Manka et al., 2012). These studies report values above $10^{20} \text{ cm}^{-3} \text{ s}^{-1}$ for temperatures between 190 and 225 K. Conversely, Laksmono et al. (2015) only reached homogeneous ice nucleation rates of 10^{11} and $10^{13} \text{ cm}^{-3} \text{ s}^{-1}$ between 226 and 231 K investigating larger volumes by increasing the cooling rate to 10^6 – 10^7 K s^{-1} . Since the water volume within soot pores hardly exceeds the critical size to produce an ice embryo, the nucleation rates need to be in the range of $10^{20} \text{ cm}^{-3} \text{ s}^{-1}$ to freeze water within 1 s. Thus, the rates reported for $T = 234$ – 238 K by numerous studies and for $T = 226$ – 231 K by Laksmono et al. (2015) are too low for pore water to freeze within atmospherically relevant time scales. Yet, water within the cylindrical pores ($D_p \approx 2$ – 10 nm) of mesoporous silica particles was able to grow into ice crystals within few seconds ($\sim 10 \text{ s}$) at 228 K but not at 233 K (David et al., 2019, 2020), implying that homogeneous ice nucleation rates have been high enough at 228 K but not at 233 K. Also, soot particles proved to freeze according to a PCF mechanism at 228 K but not at 233 K (Mahrt et al., 2018). In both cases, nucleation rates have been enhanced due to the negative pressure within the pores that develops below water saturation (Marcolli, 2017a, 2020). At 228 K, the negative pressure of $P = -43 \text{ MPa}$ at ice saturation increases the homogeneous ice nucleation rate by five orders of magnitude from $\sim 10^{15} \text{ cm}^{-3} \text{ s}^{-1}$ to $\sim 10^{20} \text{ cm}^{-3} \text{ s}^{-1}$, using the pressure dependent parameterization by Murray et al. (2010) for $n = 0.97$.

Based on these findings, we can estimate a temperature range where freezing is immediate once the water volume is large enough to host a critical ice embryo, namely for $T \leq 228 \text{ K}$, an intermediate temperature range where freezing is not immediate and strongly depends on RH ($228 < T < 233 \text{ K}$), and a range where homogeneous ice nucleation rates are too low to trigger ice formation via PCF ($T > 233 \text{ K}$). However, more dedicated experiments are needed to better constrain these ranges. In the following, we concentrate on the cirrus temperature range below $T < 228 \text{ K}$, where it is safe to assume that freezing of pore water is immediate once its volume is large enough to host a critical ice embryo.



5 Capillary condensation within soot aggregates

Water vapour can condense in capillaries below bulk water saturation, leading to the formation of water surfaces with concave curvature. The radius of the curvature is related to the equilibrium vapour pressure above the curved surface through the Kelvin equation (Kelvin, 1904; Thomson, 1871). The Kelvin equation in turn relies on the Young-Laplace equation that quantifies the pressure in liquids with curved surfaces (see Appendix B). In soot particles, as in any porous medium, capillary condensation of water starts within the narrowest pore segments and gradually fills widening pores as the ambient RH increases. Capillary condensation of water within soot aggregates has been discussed in previous studies (e.g. Persiantseva et al., 2004). The narrowest and simplest cavity consists of the slit between two adjacent primary particles (see Fig. B 3), where liquid water surrounds the contact point of the two spheres forming a pendular ring (see Fig. B 3b), referred to as pendular state (e.g. Afrassiabian et al., 2016; Urso et al., 1999). In case of wetting surfaces (negligible contact angle with water), pendular rings form concave water surfaces with curvatures that are symmetric about the line connecting the centres of the two particles (Huang et al., 2015). Note that the curvature of the water surface switches from concave to convex with increasing pore filling angle for $\theta_{sw} > 0$. Pendular rings can be described by two principal radii of curvature related to the height and the width of the water (pendular ring) above the plane connecting the centres of the two particles (filling level). Considering these two principal radii, the Kelvin equation describing the equilibrium vapour pressure over the curved surface formed by a pendular water ring can be expressed as (see Appendix B2 for details):

$$\frac{p}{p_w} = \exp\left(\frac{\gamma_{vw}(T)\left(\frac{2}{D_{pp}\sin \varepsilon} + \frac{2\cos(\theta_{sw} + \varepsilon)}{-D_{ij} + D_{pp}\cos \varepsilon}\right)v_w(T)}{kT}\right). \quad (4)$$

Here, p and p_w describe the water vapour pressure and the equilibrium water vapour pressure with respect to water, respectively, and their ratio $p/p_w = S_w$ denotes the saturation ratio with respect to water. Moreover, k is the Boltzmann constant, $v_w(T)$ is the molecular volume of liquid water and $\gamma_{vw}(T)$ is the interfacial tension between liquid water and water vapour. Finally, the angles θ_{sw} and ε correspond to the soot-water contact angle and the slit filling angle, respectively.

The pendular rings of water between neighbouring particles may also be the starting point for pore filling in ring pores. As the pendular rings of water grow in height with increasing RH , the rings on neighbouring particles will finally meet, eventually leading to full coalescence of the individual water rings. We refer to this pathway as pore filling via pendular rings of water (Fig. 3a). For the three-membered ring pore, gathering of the three water rings takes place at a slit filling angle of $\varepsilon = 30^\circ$. For four-membered ring pores, $\varepsilon = 45^\circ$ is required as illustrated in Figs. 3a and 3c. These threshold values are independent of the size of the spheres in between which the pores are formed (Afrassiabian et al., 2016). Further increase in the RH leads to a continuous growth of the water phase, ultimately causing complete filling of the ring pore. The state when a sufficient amount of liquid is available to fill the inter-particle space (pore neck) is considered the capillary state (Urso et al., 1999).

In Fig. 4 we show the RH_w conditions for filling of three-membered and four-membered ring pores via pendular rings as a function of soot-water contact angle as dashed lines. Filling conditions were calculated with Eq. (4), using fixed values of $\varepsilon =$



30° (three-membered ring pore) and $\varepsilon = 45^\circ$ (four-membered ring pore), for different primary particle diameters and overlap coefficients for a typical cirrus temperature of $T = 220$ K. Relatively high RH_w values are required for filling of a three-membered ring pore via pendular water rings. The RH_w required for pore filling decreases for decreasing contact angles and for increasing overlap coefficients. For instance, a perfectly wettable ($\theta_{sw} = 0^\circ$) three-membered ring pore formed between three particles of $D_{pp} = 20$ nm is filled at 66 % RH_w (rose dashed line) for minimal overlap of $C_{ov} = 0.01$, but already at 14 % RH_w for $C_{ov} = 0.1$ (purple dashed line). Hence, in this case, an overlap of $C_{ov} = 0.1$ can decrease the RH_w required for pore filling by ~52 %. However, the RH_w for pore filling quickly rises with increasing contact angle. Three-membered ring pores can only fill at conditions below bulk water saturation for soot-water contact angles below 56° , as indicated by the intercept of the dashed lines and the horizontal black line for $p/p_w = 1$ (see also Fig. B 4). The RH_w conditions for filling of a four-membered ring pore are shown in Fig. 4d-f in a similar fashion as for the three-membered ring pore. The criterion of $\varepsilon = 45^\circ$ for complete filling limits filling of four-membered ring pores to particles with soot-water contact angles below 37° (intercept of the dashed lines and the horizontal black line for $p/p_w = 1$ in Fig. 4d-f, see also Fig. B 4).

In conclusion, the filling of ring pores (e.g. three-membered or four-membered) via pendular rings of water is strongly constrained by the contact angle, i.e. wettability of the pore material. These results suggest that ring pore filling via (coalescence of) pendular water rings is likely not an important mechanism for atmospheric soot particles, which tend to have higher contact angles (see Section 2.4). Yet, if the soot-water contact angles are too high for n -membered pore ring structures to become completely filled via coalescence of pendular water rings, complete pore filling can still take place through *direct pore filling*. This filling mechanism is illustrated in Fig. 3b and d for the three-membered and four-membered ring pores, respectively. Direct filling starts from random fluctuations of adsorbed water patches resulting in spontaneous condensation of water at the pore neck (narrowest part of a ring pore, which is located at the midplane formed by the centres of the spheres making up the ring) as illustrated in Fig. 3b and d). The Kelvin equation describing the equilibrium vapour pressure over the curved surface for direct filling of three-membered ring pores with liquid water is given by (Appendix B4):

$$\frac{p}{p_w} = \exp \left(\frac{\gamma_{vw}(T) \left(\frac{4\sqrt{3} \cos(\theta_{sw} + \varepsilon)}{-2D_{ij} + \sqrt{3}D_{pp} \cos \varepsilon} \right) v_w(T)}{kT} \right). \quad (5)$$

In Eq. (5) the shape of the curvature of the water surface is described by only one principal radius. This is because non-orthogonal, unequal radii of curvature will equalize and minimize the surface energy at equilibrium, so that the hydrostatic pressure within the capillary condensate is always isotropic. This is consistent with the results of previous studies addressing the shape of capillary surfaces in non-circular geometries. For instance, Feng and Rothstein (2011) studied the equilibrium shape of curved surfaces in capillaries with n -sided, polygonal cross-sectional areas, finding the shape of the curved surface to be spherical. A change in cross-sectional geometry is essentially equivalent to a change in the contact angle between the pore wall and the fluid. This is in-line with more recent results from Son et al. (2016), who modelled the menisci formed in



triangular and square tubes, equivalent to our three-membered and four-membered ring pores, and reporting the liquid surface to form a hemisphere at equilibrium.

In case of four-membered ring pores, the Kelvin equation describing the equilibrium water vapour for direct pore filling is given by (Appendix B5):

$$\frac{p}{p_w} = \exp \left(\frac{\gamma_{vw}(T) \left(\frac{4 \cos(\theta_{sw} + \varepsilon)}{-\sqrt{2}D_{ij} + D_{pp}\cos\varepsilon} \right) v_w(T)}{kT} \right). \quad (6)$$

490 The RH_w conditions required for direct filling of three-membered and four-membered ring pores, as calculated with Eqs. (5) and (6), are shown in Fig. 4 as solid lines. Obviously, direct pore filling requires significantly lower RH_w compared to pore filling via pendular water rings for both types of ring pores considered here (compare dashed and solid lines in Fig. 4). As an example, at $T = 220$ K, the RH_w required for filling of a three-membered ring pore with $D_{pp} = 20$ nm and $C_{ov} = 0.01$ assuming a contact angle of $\theta_{sw} = 0^\circ$ (60°), is ~ 66 % (119 %) for pore filling via pendular rings of water, and ~ 31 % (55 %) for direct filling (rose dashed and solid lines, respectively). If the primary particles with $D_{pp} = 20$ nm forming the three-membered ring pore overlap with $C_{ov} = 0.1$, capillary condensation within the three-membered ring pore via direct filling can already take place at $RH_w < 5$ % for $\theta_{sw} = 0^\circ$ and at $RH_w \approx 12$ % for $\theta_{sw} = 60^\circ$. Thus, soot aggregates with appropriate pore properties can take up water not only in clouds but potentially throughout the troposphere, where RH_w frequently cycles from ~ 20 % to 80 % (Wallace and Hobbs, 2011). Comparing the conditions for direct filling of a three-membered ring pore (Fig. 4a, b and c) to those of a four-membered ring pore (Fig. 4d, e and f), it is evident that direct filling of four-membered ring pores requires higher RH_w . This is due to the larger size of the opening formed between four compared to three spheres, as discussed in Sect. 3 (see also Fig. 2). In contrast to pore filling via the pendular water rings, direct pore filling exhibits a weaker dependence on the soot-water contact angle and remains effective below water saturation for $0 \leq \theta_{sw} \leq 90^\circ$ (see Fig. 4). For contact angles of $\theta_{sw} > 90^\circ$ the condensed liquid exhibits a convex curvature, which goes along with an equilibrium vapour pressure that is higher than that of bulk liquid water.

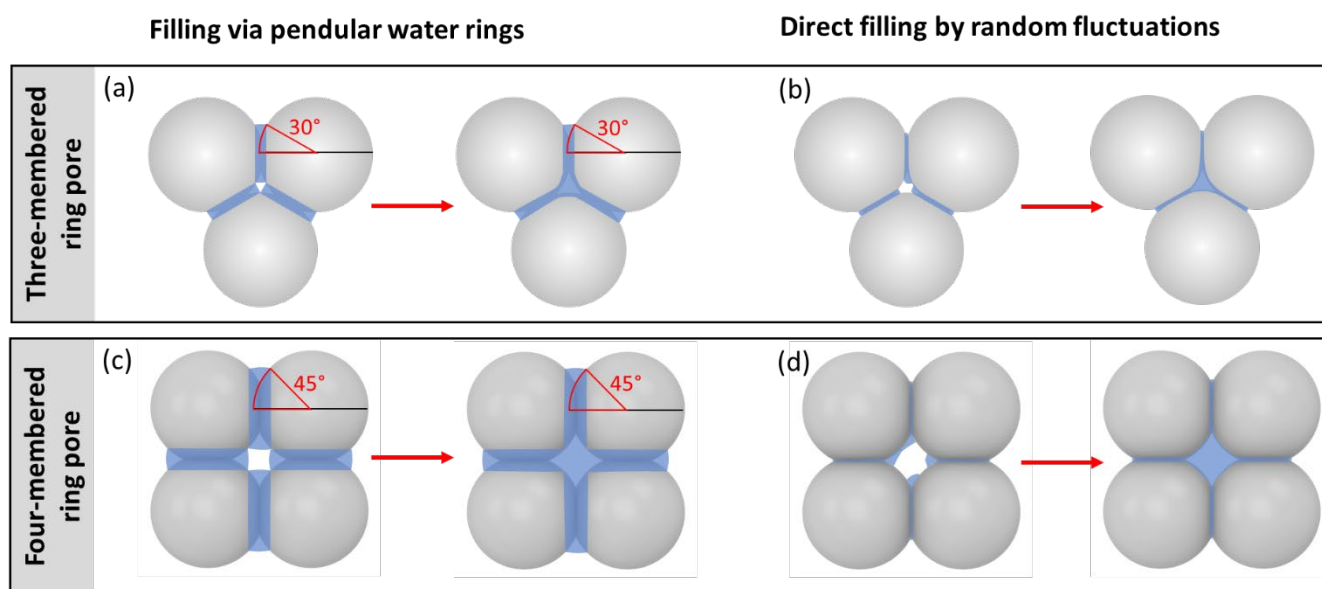
500 The solid lines in Fig. 4 denote the conditions for the formation of a continuous liquid water phase at the pore neck. However, in order to contribute to ice formation via PCF, the water volume within a pore must be sufficiently large to host a critical ice germ, as discussed in Section 4.1. We take this into account by calculating the RH_w required for direct filling of the ring pores with water up to a filling level of h_{fr} , denoting the height that the water needs to extend vertically in both directions from the midplane (pore neck), for freezing of the capillary condensate. A value of $h_{fr} = 1.25$ nm is an approximate value that was chosen based on the experimental observations of David et al. (2020), and theoretical considerations taking calculated critical embryo size and quasi-liquid layer width into account as discussed in Sect. 4.1. The RH_w required to reach a filling level of h_{fr} are given by the dotted lines in Fig. 4. For each set of dotted and solid lines, the RH_w required to just fill the neck of the ring pore is lower compared to filling the ring pore up to a level of h_{fr} . This difference becomes larger with increasing soot-water contact angle, as can be seen from the diverging solid and dotted lines in Fig. 4 for each set of curves. Moreover, the difference

515



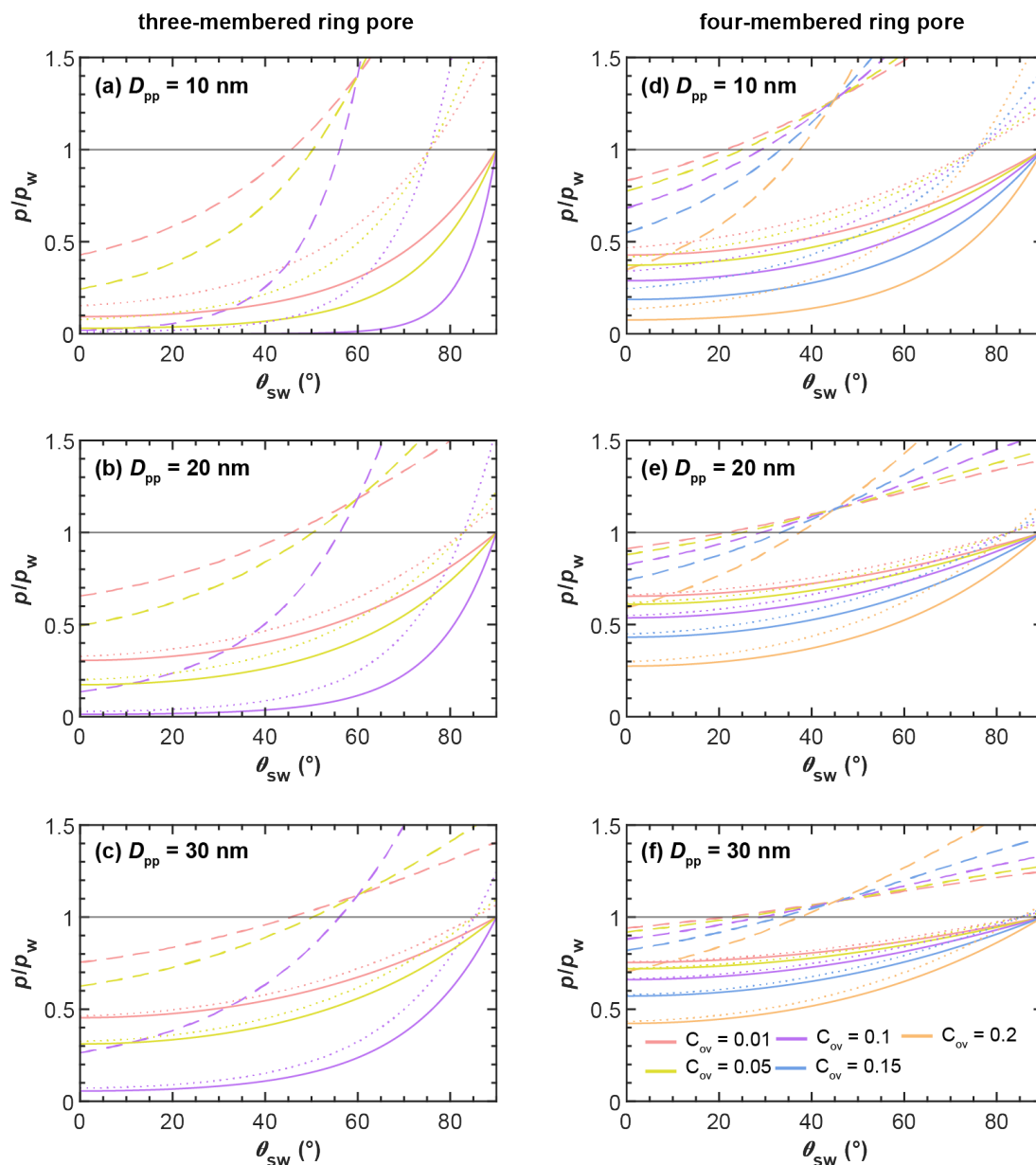
520

in RH_w required for direct filling and direct filling up to h_{fr} becomes more distinct for increasing overlap coefficients and decreasing primary particle diameters. It should be noted that in the absence of overlap h_{fr} cannot be reached. On the whole, we conclude that direct filling gives a realistic pathway of pore condensation for ring pores in soot aggregates that are characterized by considerable contact angles, while the pathway via pendular rings of water strongly overestimates the RH required for pore filling.



525

Figure 3: Illustration of the filling scenarios for (a, b) three-membered and (c, d) four-membered ring pores formed between spheres in a tetrahedral and cubic packing arrangement assuming $\theta_{sw} = 60^\circ$. In the three-membered and four-membered ring pore case, uptake of liquid water is either considered as *filling via the pendular rings of water* (a, c) or as *direct filling* (b, d). Direct filling starts at the pore neck, defined as the narrowest point of the ring pore opening located at the midplane between the centres of the spheres. In case of filling via the pendular water rings slit filling angles of $\varepsilon = 30^\circ$ and $\varepsilon = 45^\circ$ need to be reached for pendular rings to gather together and coalesce. Note that for $\theta_{sw} = 60^\circ$, the water surface has a convex curvature at a filling angle of $\varepsilon = 45^\circ$. If the RH is further increased, further filling of the ring pore as well as the inner cavity (concave octahedron and concave cube) takes place.



530 **Figure 4:** Pore filling conditions for three-membered ring pores (tetrahedral packing, **a, b, c**) and four-membered ring pores (cubic packing, **d, e, f**) showing the saturation ratio with respect to water ($p/p_w = S_w$) required for filling of ring pores as a function of the soot-water contact angle (θ_{sw}) at $T = 220$ K. The different rows correspond to ring pores formed for spheres with different diameters (D_{pp}). In each panel the S_w needed for capillary condensation of water in the ring-pore is compared for different filling mechanisms: Slit-filling up to $\varepsilon = 30^\circ$ (three-membered ring-pore) and $\varepsilon = 45^\circ$ (four-membered ring-pore) via pendular rings of water, followed by coalescence of water-rings and complete filling of the ring pore is shown by the dashed lines. Direct filling of the ring pore neck is shown by the solid lines. Direct filling of the ring pore up to a height of $h_f = 1.25$ nm, required for freezing is shown by the dotted lines. The set of lines within each panel corresponds to different values for the overlap coefficient, C_{ov} , as indicated in the legend. The expressions for the Kelvin equations describing the conditions for pore filling for the various filling mechanisms are given in Appendix B.

535



6 Ice growth out of the soot ring pores

540 In Section 5 we have shown that direct filling of ring pores with liquid water up to the freezing level (h_{fr}) may take place at RH_w well below bulk water saturation. In this section, we determine the ice supersaturation required for the growth of the pore ice out of the ring pores into a macroscopic ice crystal.

In the following, we assume rigid soot pore structures that cannot facilitate ice growth out of narrow pore openings by expanding upon ice growth. We describe ice growth out of the pore by the same governing equations (see Appendix B) as for
 545 filling with water, treating the ice growth as continuous filling of the pore throat with ice. The RH_i of water vapour in equilibrium with the growing ice phase can then be obtained by evaluating Eq. (B 15) with respect to ice:

$$\frac{p}{p_i} = \exp\left(\frac{\gamma_{vi}(T) \left(\frac{4\sqrt{3} \cos(\theta_{si} + \varepsilon)}{-2D_{ij} + \sqrt{3}D_{pp} \cos \varepsilon}\right) v_i(T)}{kT}\right). \quad (7)$$

Here, p and p_i are the water vapour pressure and the equilibrium water vapour pressure with respect to ice, respectively, and their ratio yields the saturation ratio with respect to ice (S_i). Moreover, $\gamma_{vi}(T)$ is the interfacial tension between ice and water vapour, $v_i(T)$ is the molecular volume of water in ice, and θ_{si} is the contact angle between ice and water vapour. Similarly,
 550 evaluating Eq. (B 19) with respect to ice, the Kelvin equation describing the equilibrium vapour pressure for ice growth out of a four-membered ring pore is given by:

$$\frac{p}{p_i} = \exp\left(\frac{\gamma_{vi}(T) \left(\frac{4 \cos(\theta_{si} + \varepsilon)}{-\sqrt{2}D_{ij} + D_{pp} \cos \varepsilon}\right) v_i(T)}{kT}\right). \quad (8)$$

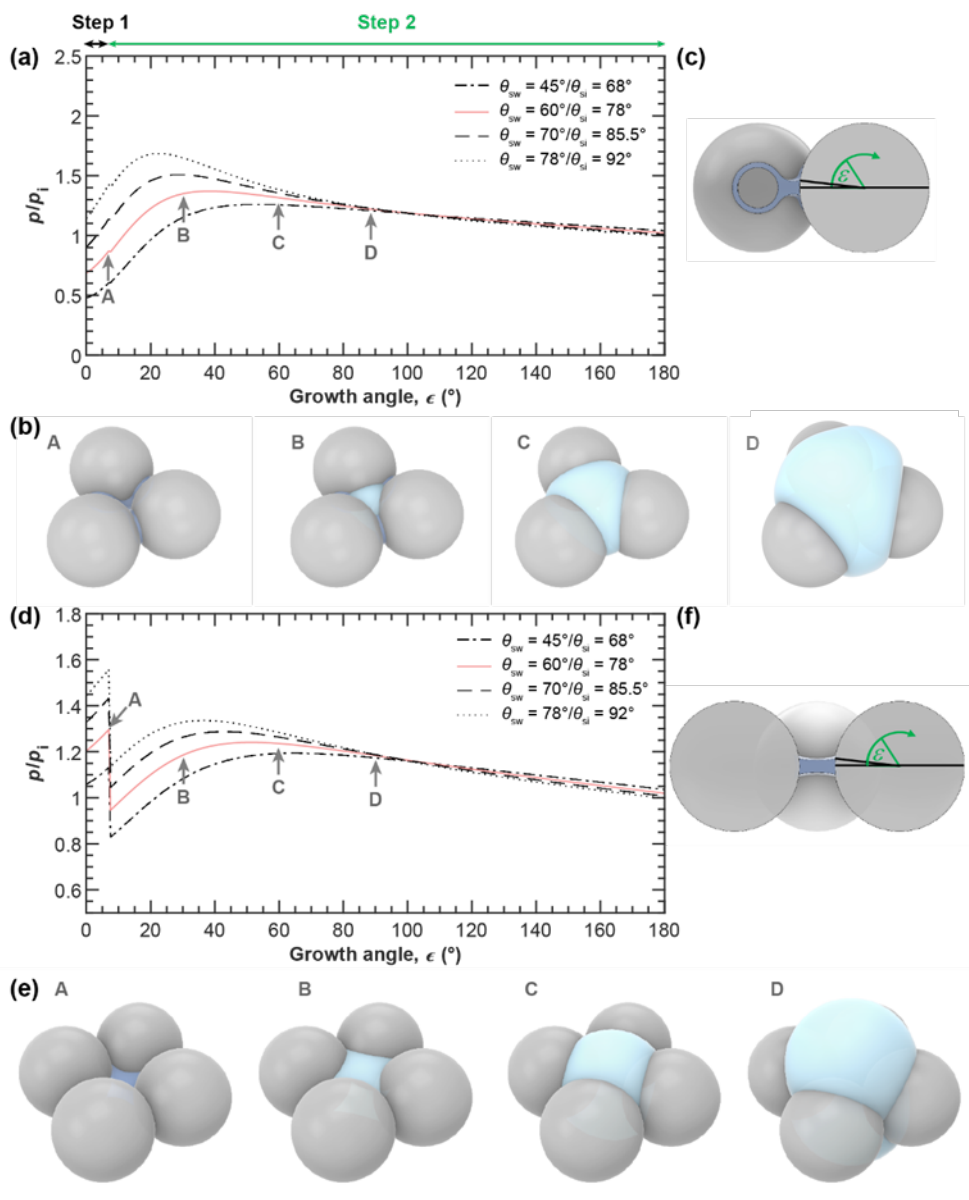
The interfacial tension between ice and vapour is not well known. Following previous studies, we assume a quasi-liquid layer to form on the ice surface (Gelman Constantin et al., 2018; Wettlaufer, 1999). Then an upper limit of the interfacial tension of ice and water vapour is given by the sum of the interfacial tensions of water and vapour and ice and water: $\gamma_{vi}(T) = \gamma_{vw}(T) +$
 555 $\gamma_{iw}(T)$, following David et al. (2019). Their molecular dynamics simulation showed an ordered arrangement of an ice phase growing out of a silica pore, that can be interpreted as a contact angle between the two solid phases of the ice and the silica particle. This approach allows to substitute $\gamma_{vi}(T)$ in Eqs. (7) and (8) by the sum of $\gamma_{vw}(T)$ and $\gamma_{iw}(T)$. Similarly, the contact angle between ice and soot is not well constrained by measurements and an upper limit can be estimated by assuming a quasi-liquid layer between pore ice and the soot surface, as described in Appendix C. The presence of a quasi-liquid layer between
 560 pore ice and the (hydrophobic) pore wall material has been confirmed by measurements (Morishige, 2018) and molecular simulations (Moore et al., 2012).

Figures 5a and d show the equilibrium vapour pressure with respect to ice, $p/p_i = S_i$, above the condensing water and growing ice phases during PCF in three-membered and four-membered ring pores as a function of growth angle ε as illustrated in panels c and f and evaluated using Eqs. (5)–(8). In panels b and e, PCF is exemplified for ring pores with $D_{pp} = 20$ nm and contact



565 angles of $\theta_{sw}(\theta_{si}) = 60^\circ (78^\circ)$ with $C_{ov} = 0.05$ for the three-membered ring pore, and $C_{ov} = 0.1$ for the four-membered ring
pore. The curves for capillary condensation and pore ice growth for these pores are shown as rose, solid lines in panels a and
d (Fig. 5). Curves for other contact angle values are given as dashed lines for comparison. The curves start at the p/p_i required
for direct pore filling by water followed by an increase in p/p_i up to the point where a filling level of $h_{fl} = h_{fr} = 1.25$ nm is
reached. Once h_{fr} is reached ice nucleation of the pore water takes place and the governing (growth) equations have to be
570 evaluated with respect to ice to describe further growth. The switch from water to ice growth is marked by the kink in the
curves. During this first step of water condensation and condensational growth, the slit filling angle increases from $\varepsilon = 0^\circ$ to ε
 $= \varepsilon_{fr}$. The second step of ice growth by water vapour deposition is described by a further increase of the growth angle from ε_{fr}
to $\varepsilon = 180^\circ$. Using ε as growth coordinate assumes that the contact angle between ice and soot is maintained throughout the
ice growth, determining the ice surface curvature. This growth coordinate is able to capture the specific characteristics of the
575 ice growth although it neglects deviations from the prescribed curvature that occur when the ice caps growing out of the two
opposite openings merge as it is the case for the three-membered ring pores (see panel b, frame D). During ice growth, p/p_i
again increases and passes through a maximum before it transforms to depositional growth of an ice crystal. Inspection of Fig.
5 shows that the maximum in the ice growth curves is for $\varepsilon < 30^\circ$, i.e. for ice growth within the pore, implying that it is the
local pore geometry that determines the supersaturation required for PCF of soot and not the overall aggregate structure. Along
580 each curve, the filling or growth step that is associated with the highest S_i (global maximum) is the limiting step and determines
the critical supersaturation for soot-PCF. For the cases shown in Fig. 5, PCF for the three-membered ring pore is limited by
ice growth while for the four-membered pore it is limited by water condensation up to $h_{fr} = 1.25$ nm. More specifically, the
maximum RH_i of the filling and growth steps of the three-membered ring pore are 86 % and 137 %, respectively (solid, rose
line in Fig. 5a). Conversely, the filling-limited four-membered ring pore has maxima of 129% RH_i and 124 % RH_i , for the
585 filling and ice growth steps, respectively (solid, rose line in Fig. 5d).

Figures D1 and D2, show additional PCF curves for other primary particle sizes and overlaps. This overview shows that soot-
PCF is sensitive to contact angles, primary particle size and overlap. Overall, the narrower three-membered ring pores tend to
be ice growth limited, while the wider four-membered ring pores are rather limited by water condensation. Increasing overlap
and decreasing primary particle size both shift the limiting step of soot-PCF from capillary condensation to pore ice growth.
590 With increasing contact angle, the RH required for both, pore condensation and ice growth shift to higher values. For instance,
for a given contact angle of $\theta_{sw}(\theta_{si}) = 45^\circ (68^\circ)$, the onset of soot-PCF is expected already at $S_i \approx 1.15$ (for four-membered
ring pores with $D_{pp} = 30$ nm and $C_{ov} = 0.2$). This onset shifts to $S_i \approx 1.21$ for $\theta_{sw}(\theta_{si}) = 60^\circ (78^\circ)$, to $S_i \approx 1.27$ for $\theta_{sw}(\theta_{si}) = 70^\circ$
(85.5°), and to $S_i \approx 1.35$ for $\theta_{sw}(\theta_{si}) = 78^\circ (92^\circ)$.



595 **Figure 5:** PCF by three-membered (a – c) and four-membered (d – e) ring pores. (a, d) Saturation ratio with respect to ice (S_i) required for
 (step 1) direct filling of the ring pore up to a filling level $h_f = h_f^* = 1.25$ nm, followed by (step 2) growth of pore ice as a function of the
 growth angle ϵ , as illustrated in the side views (panels c and f). The 3D renderings illustrate the water growth up to $h_f = 1.25$ nm (A: darker
 blue, $\epsilon = 7.18^\circ$) and ice growth (light blue, $\epsilon = 30^\circ$ (B), 60° (C), and 90° (D)) for a three-membered ring pore with $D_{pp} = 20$ nm, $C_{ov} = 0.05$,
 and θ_{sw} (θ_{si}) = 60° (78° , panel b) and a four-membered ring pore with $D_{pp} = 20$ nm, $C_{ov} = 0.1$, and θ_{sw} (θ_{si}) = 60° (78° , panel e). All soot-PCF
 600 curves were calculated for $T = 220$ K, $D_{pp} = 20$ nm, and different contact angles as indicated in the legend. See Figs. D 1 and D 2 for soot-
 PCF curves encompassing different primary particle sizes and overlaps.



7 Constraints on stability of pore ice and pre-activation

The ability of aerosol particles to form macroscopic ice crystals at lower relative humidities and/or higher temperatures compared to their intrinsic ice nucleation efficiency after prior having experienced an ice nucleation event or low temperatures is called pre-activation (Fukuta, 1966; Mason, 1950; Mossop, 1956; Pruppacher and Klett, 1997). Many or even most observations of pre-activation can be explained by pore ice that has nucleated in a preceding activation step/cloud cycle (Marcolli, 2017b), allowing ice crystal formation by pure depositional growth when the particles re-encounter ice supersaturation. Yet, some observations of pre-activation may also be explained by the contact of soot aggregates with ice or liquid water changing their (pore) morphology or modifying surface functionalization (Bhandari et al., 2019; China et al., 2015; Colbeck et al., 1990; Ma et al., 2013; Miljevic et al., 2012; Zuberi et al., 2005), and thus enhancing their ice nucleation activity in subsequent cloud cycles, even in the absence of ice pockets preserved in pores (Mahrt et al., 2020b). Here, we focus on pre-activation through ice preserved in pores. This pre-activation mechanism is most effective when the ice nucleation rate is low and the presence of pore ice enables bypassing the nucleation step. This is the case when pore ice that formed through homogeneous ice nucleation at low temperatures persists to temperatures above the HNT enabling growth to macroscopic ice when (re-)encountering ice supersaturated conditions. Soot proved to be susceptible to this pre-activation mechanism in a study by Wagner et al. (2016). Specifically, they found soot, which was not ice active at temperatures above the HNT, to produce a small ice fraction even up to $T = 250$ K, after having undergone an initial cloud processing cycle at 228 K, i.e. well below the HNT.

Ring pores have the potential to show pre-activation as ice may persist in the pore necks at RH well below ice saturation and, when ice supersaturation is reached, grow out of the pore. Inspection of the soot-PCF curves displayed in Figs. 5, D1 and D2 shows that the ability of a pore to show pre-activation depends on the pore type (three-membered or four-membered), primary particle size and overlap, as well as contact angle of soot with water and ice. For ice preserved in narrow pores with high contact angles, growth is only expected at RH above water saturation, implying that cloud droplet activation should precede ice crystal growth. This was indeed observed by Wagner et al. (2016), where the majority of the pre-activated soot particles that produced ice at $T = 250$ K froze in condensation mode. Note, that the critical embryo size increases with increasing temperature. Therefore, the soot-PCF curves shown in Figs. 5, D1 and D2 must be re-calculated at the ice growth temperature to judge whether the ice is able to persist in the pore. Indeed, pre-activation to temperatures well above the HNT relevant for glaciation of MPCs requires large cavities with small openings that need to open up to release the ice contained in them during cloud droplet activation. Thus, the larger inner cavities between four tetrahedrally or eight cubic arranged primary particles (see Fig. 1 for cavity shapes and Fig. 2 for their radii) are the ones that are likely best suited to preserve ice to higher temperatures.

At cirrus conditions, when ice nucleation rates are high, pre-activation is not expected to increase the fraction of ice active soot aggregates, but its main effect is to reduce the supersaturation required for soot-PCF to result in macroscopic ice crystals. When homogeneous ice nucleation rates are high, PCF is either limited by water condensation or ice crystal growth. In case



635 of pre-activation, since the pores are already filled with ice, the supersaturation required for pore condensation is irrelevant
and ice growth becomes the limiting step. Thus, in cases where soot-PCF is ice growth limited, pre-activation has no effect.
Conversely, in cases where capillary condensation of pore water constitutes the limiting step of soot-PCF, pre-activation lowers
the supersaturation required for soot-PCF to the value for ice growth. Moreover, for pre-activation, pore ice needs to remain
thermodynamically stable at $RH_i < 100\%$, so that it can grow by vapour deposition upon (re-)encountering ice supersaturation.
640 Whenever n -membered ring pores in soot aggregates fulfil both conditions, i.e. soot-PCF is capillary condensation limited and
ice remains in pores to $RH_i < 100\%$, pre-activation should be relevant. Figs. 5, D1 and D2 exemplify for which combinations
of primary particle diameters, overlap coefficients and contact angles these conditions are met. It can be seen that pre-activation
has a limit to high contact angles, as for $\theta_{si} > 85.5^\circ$ pore ice is not preserved at $RH_i < 100\%$ for any three-membered or four-
membered ring pore considered here. Since three-membered ring pores tend to be narrow, PCF is for most of them constrained
645 by ice growth and pre-activation has only a marginal or no effect at all. The only exceptions are combinations of large primary
particles ($D_{pp} > 30$ nm) and small overlap ($C_{ov} \leq 0.05$). Pre-activation in four-membered ring pores is more prevalent and may
occur when $D_{pp} > 20$ nm and/or $C_{ov} \leq 0.2$ and is able to reduce the supersaturation required for macroscopic ice growth by up
to 40 % RH_i at $T = 220$ K. Yet, ice in ring pores for which soot-PCF is limited by water condensation is only preserved to 80–
90 % RH_i . To keep pore ice to lower RH , larger pores need to fill with ice, such as the larger inner cavities between four
650 tetrahedrally or eight cubic arranged primary particles. However, these cavities are rarer and require larger soot aggregate
sizes. Nonetheless, we note that by taking into account the complex pore morphology of fractal soot aggregates, the framework
presented herein is able to capture the hysteresis of soot particles between water uptake and release as previously reported (e.g.
Dubinin, 1980; Mahrt et al., 2018; Popovicheva et al., 2008), which cannot be described by approximating soot pores as
cylindrical cavities that lack hysteresis.
655 Overall, pre-activation is most important when particles that were activated under cirrus conditions reach MPC conditions and
the ice preserved in pores can grow to macroscopic ice crystals. Moreover, our results suggest that pre-activation at cirrus
conditions is less relevant than previously estimated (e.g. Zhou and Penner, 2014), as it does not increase the number of ice-
nucleating soot particles, but just reduces the supersaturation required for activation for a minor fraction of the soot particles.
This confirms that the increased ice nucleation activity at cirrus conditions after cloud processing as observed by e.g. Mahrt et
660 al. (2020b) is due to changes in the surface functionalization and morphology of soot aggregates (compaction) and not caused
by pre-activation through ice preserved in pores.

8 Parameterizing soot-PCF for ice nucleation of soot aggregates

In the previous sections we have shown that n -membered ring pores form cavities that are able to provide ice nucleation activity
to soot aggregates. We now use these findings to explain ice nucleation experiments performed with different soot types. In
665 Fig. 6 we show activated fractions (AF) as a function of RH of size-selected soot particles as determined in a continuous flow
diffusion chamber (Mahrt et al., 2018, 2020b). The AF describes the cumulative fraction of total soot particles of a given size



that formed macroscopic ice crystals larger than 1 μm (optical) diameter within the ice chamber at given RH and T conditions, as counted with an optical particle counter (see Mahrt et al., 2018 for details). We constrain ourselves to data obtained from two soot types with vastly different properties, namely FW200, taken from Mahrt et al. (2018), and miniCAST black soot
670 taken from Mahrt et al. (2020b). FW200 is a commercially available soot (Orion Engineered Carbons GmbH, Frankfurt, Germany) with average primary particle diameter of $D_{pp} = 22 \pm 3.9$ nm and fractal dimension of $D_f = 2.35$, as measured by Mahrt et al. (2018). The miniCAST black soot is a propane flame soot, generated in a diffusion flame under fuel-lean conditions with average $D_{pp} = 31 \pm 5.9$ nm and $D_f = 1.86$ (Mahrt et al., 2018). Furthermore, the water sorption measurements by Mahrt et al. (2018) indicate that the water uptake capacity of the miniCAST black is significantly lower compared to that of the FW200
675 soot. Thus, miniCAST black should represent a soot with higher soot-water contact angle compared to FW200 (Mahrt et al., 2018). Both soot types taken together cover a wide range of properties relevant for ambient soot particles (see Section 2.1). In Fig. 6 we show the AF as a function of both RH_i and RH_w , for aggregates with electrical mobility diameters between $D_m = 400$ nm and $D_m = 100$ nm, and for typical cirrus temperatures of $T = 223$ K (crosses) and $T = 218$ K (circles). Interestingly, for miniCAST black, the AF curves for $T = 218$ K and $T = 223$ K collapse onto the same line when plotted as a function of RH_w
680 (see Fig. 6b), but are clearly offset when plotted as a function of RH_i . This behaviour suggests that the filling of the ring pore structures with water is the limiting step for miniCAST black particles for soot-PCF (see Section 6). This is consistent with our prediction that critical supersaturations for three-membered and four-membered ring pores with comparable primary particle size of $D_{pp} = 30$ nm tend to be determined by capillary condensation (see bottom row in Figs. D 1 and D 2). Conversely, the AF curves of the 400, 300, and 100 nm aggregates of the FW200 soot at $T = 218$ K and $T = 223$ K do not overlap when
685 plotted as a function of RH_w , while the curves clearly overlap when plotting them as a function of RH_i . The only exception are the 200 nm aggregates, which show deviations in both scales. This demonstrates that soot-PCF by the ring pores of the FW200 soot is not limited by filling with liquid water but by ice growth out of the pores instead. Considering our predictions for pore filling and ice growth in three-membered and four-membered ring pores formed between particles with $D_{pp} = 20$ nm suggest that the PCF activity of FW200 soot results primarily from three-membered ring pores, since four-membered ring pores tend
690 to be limited by water uptake into the pores (i.e. the filling step; see Figs. D1 and D2). The onset of freezing for both soot types is clearly above ice saturation, as is expected for pore surfaces with rather high contact angles to water and ice. Since the detection limit for this experimental setup is reached at $AF = 10^{-4}$ – 10^{-3} as evidenced by the increased scatter, we consider the RH when values above this AF -range are reached as onset. In a recent study, David et al. (2020) observed a shift of freezing onsets from about 115 % RH_i to 120–135 % RH_i when the surface of hydroxylated mesoporous silica particles ($\theta_{sw} = 41$ – 45°)
695 was methylated ($\theta_{sw} = 75$ – 80°). Inspection of Figs. D1 and D2 shows that the freezing onset of 400 nm miniCAST black aggregates of about 125 % RH_i is in accordance with approximately θ_{sw} (θ_{si}) of 70° (85.5°) while a freezing onset of about 116 % RH_i as observed for 400 nm FW200 aggregates conforms with a contact angle of approximately θ_{sw} (θ_{si}) $< 60^\circ$ (78°). Overall, the theoretical framework developed here allows to describe ice formation on soot aggregates and helps to explain differences in the ice nucleation ability of soot particles reported in the literature.



700 In order to use the new framework to predict soot-PCF via n -membered ring pores, the abundance of such pore structures within soot aggregates needs to be considered. For this reason, we have developed an equation to quantify the ice active fraction (AF) as a function of RH that reflects aggregate and pore properties:

$$AF = 1 - (1 - P_N(RH))^{((N_p - n_m)^{D_f})} \quad (9)$$

Here, $P_N(RH)$ is the probability of a primary particle to be part of a ring pore that induces ice nucleation and growth at RH in a deterministic fashion, N_p denotes the number of primary particles within the soot aggregate and D_f is the fractal dimension.

705 The active-site probability function $P_N(RH)$ can be derived from first principles to reflect the properties (contact angle, primary particle size and overlap) of a specific soot type (e.g. aviation or diesel car emissions) or it can be treated as a fit function to bring the AF -parameterization in agreement with measured datasets. Depending on the soot properties and the ice nucleation data, $P_N(RH)$ can be parameterized in terms of relative humidity with respect to ice ($P_N(RH_i)$) or water ($P_N(RH_w)$). We note that even if $P_N(RH)$ is determined through fitting to an existing dataset, it can be used along with Eq. (9) to predict the ice

710 nucleation activity of soot particles with different properties (fractal dimension, number and size of primary particles).

To obtain the fraction of soot aggregates with ring pores, the probability of a primary particle to be part of a ring pore is potentiated by the number of primary particles contained within the soot aggregate ($N_p - n_m$). N_p in turn can be calculated from defining relations of fractal aggregates based on the primary particle size and the fractal dimensions (see Appendix E). Furthermore, the number of neighboring spheres surrounding a primary particle is considered in terms of the fractal dimension

715 D_f . To account for the minimum number of primary particles required to form a ring pore, n_m is subtracted from the total number of primary particles within the aggregate, N_p . In case of three-membered and four-membered-ring pores the value of n_m is 2 and 3, respectively. The value of n_m is relevant to correctly represent the smallest soot aggregates that still may contain a pore and ensures AF to be nonzero even for small number of primary particles within an aggregate, as long as ring pores can be formed. The inclusion of primary particle number and compaction in Eq. (9) allows to parameterize the ice nucleation

720 activity of differently sized soot aggregates using the same active site probability function.

Because soot properties such as the primary particle size and the fractal dimension can readily be measured, this soot-PCF framework can directly be compared to and constrained by experimental data. The lines shown in Fig. 6 are based on Eq. (9) using the experimental soot characterization and the ice nucleation data as explained in Appendix E. The number of primary particles in soot aggregates as a function of their aggregate size are detailed in Table E1, while Table E2 lists the parameters

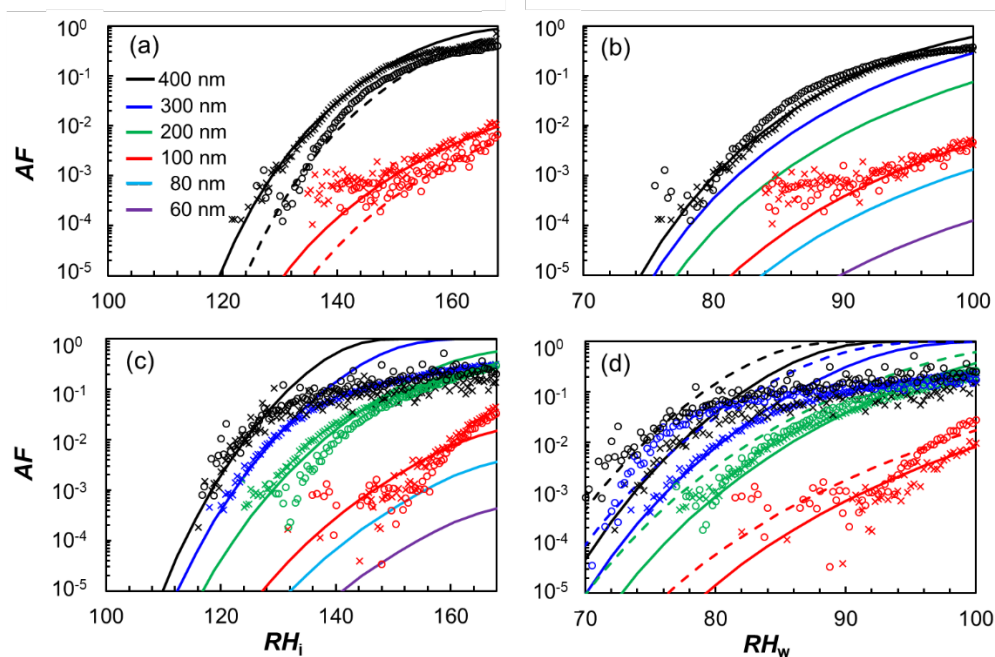
725 that were used in Eq. (9) to model the AF data. Since for FW200, activated fractions measured at 218 K and 223 K collapse on one line when plotted as a function of RH_i , we parameterized the active-site probability as a function of RH_i . Since the conversion from RH_i to RH_w is temperature dependent, AF splits into two separate curves, one for 218 K and one for 223 K when plotted as a function of RH_w . Conversely, since AF at 218 K and 223 K of miniCAST black coincide when plotted as a function of RH_w , we parameterized the active-site probability as a function of RH_w .

730 The differently colored curves shown in Fig. 6 denote activated fractions of soot aggregates with different mobility sizes. Since the activated fraction of aggregates from a given soot type rely on the same active-site probability function ($P_N(RH)$), AF



735 curves for mobility diameters that have not been measured can be derived from Eq. (9). Thus, activated fractions for lower supersaturation ratios and smaller soot aggregate sizes than have been measured, e.g. because they were below the detection limit, can be derived as long as data for larger aggregates and/or higher supersaturations are available. Moreover, a parameterization can be established even in the absence of ice nucleation data, when a soot sample has been characterized with respect to the aggregate size and compaction, the primary particle diameter and overlap, and the contact angle with water and ice (see Appendix E). The active-site probability (fit) function depends on the soot particle properties, and measurements thereof are often associated with some degree of uncertainty. For instance, Anderson et al. (2017) quantified the uncertainty of a single measurement of the mean soot primary particle diameter derived from TEM to be $\pm 14\%$. We note that Eq. (9) can easily be adapted to consider different primary particle diameters to describe the same AF curves of the different soot aggregate sizes shown in Fig. 6, again using a single fit function ($P_N(RH)$). For example, assuming a lower mean primary particle diameter increases the number of primary particles within a soot aggregate, and allows smaller soot aggregates to be active via soot-PCF. In this case, a fit to the data is achieved by lowering the probability of a primary particle to be part of a ring pore that induces PCF at a specific RH . Conversely, the spacing between the soot-PCF curves of differently sized aggregates in Fig. 6 is not a free parameter but determined by the fractal dimension of the soot aggregates. Therefore, complying with the AF curve measured for 100 nm FW200 particles implies full activation ($AF = 1$) for $D_m = 300$ nm at $RH_i \approx 155\%$ for $T = 223$ K, or at lower saturation ratios for larger soot aggregates. This suggests that the levelling off observed for the experimental data points at $AF \approx 0.2$ results from instrumental limitations, and in the case depicted in Fig. 6 could result from divergence of particles out of the region of highest RH conditions (aerosol-lamina). Overall, the good agreement of the parameterized curves with the measured data shown in Fig. 6 is compelling evidence that the active-site probability function provides an excellent means to describe PCF on soot aggregates of different sizes when combined with relevant aggregate and pore properties. This is an advantage over previously proposed parameterizations that often rely on datasets that were specific to an aggregate size and/or a single emission source.

740
745
750



755 **Figure 6:** Fraction of soot particles that nucleate ice, termed activated fraction (AF), at temperatures of $T = 218$ K (circles) and $T = 223$ K
crosses), as a function of relative humidity with respect to ice (RH_i ; left) and water (RH_w ; right) for (a, b) miniCAST black soot and (c, d)
760 FW200 soot. The different colours denote soot aggregates of different electrical mobility diameter D_m as indicated in the legend. Data is
taken from Mahrt et al. (2018) for FW200 and from Mahrt et al. (2020b) for miniCAST black. The solid and dashed lines show the
parameterization for 223 K and 218 K, respectively. Note that in case of miniCAST black the curves at 218 K and 223 K coincide when
plotted as a function of RH_w , while in case of FW200 the curves coincide when plotted as a function of RH_i . See Appendix E for details.

9 Atmospheric implications

The framework presented here links the ice nucleation ability of soot with its physicochemical properties, namely primary particle size and overlap, aggregate size, and contact angle with water and ice and by that provides a physical basis to uniformly describe the ice nucleation mechanism by pore condensation and freezing for soot.

765 Given that the ice nucleation activity of soot particles is linked to pores that form between primary particles, the framework
presented here allows to better constrain the properties required for atmospheric soot particles to form ice via PCF. For instance,
at least three primary particles are required to form the smallest conceivable pore (the three-membered ring pore). Hence, the
minimum soot particle (aggregate) size to nucleate ice via PCF should exceed the average primary particle size of a soot
sample. Moreover, soot spherules need to be arranged in a closed loop to form a ring pore or even be more closely packed to
770 form an inner cavity. Thus, having three primary particles in a soot aggregate is not a sufficient condition for PCF. The soot
aggregate needs some degree of compaction to generate closed loops along a chain of soot spherules. This explains the role
that cloud processing plays in increasing the ice nucleation activity of soot as observed by e.g. Mahrt et al. (2020b), who found
the ice nucleation ability of processed, compacted soot particles to be significantly higher compared to unprocessed, more



775 fractal soot. This is further supported by recent result of Zhang et al. (2020), who investigated different laboratory analogues of soot and found the largest ice nucleation activity to be associated with the most spherical, i.e. compacted soot type. Since evaporating water or ice exert a tension on the surrounding soot spherules (e.g. China et al., 2015; Ma et al., 2013), these are attracted to each other and open loops can close giving rise to ring pores and larger cavities.

We focused our analysis on three-membered and four-membered ring pores as these should be the pores most relevant for soot-PCF on soot particles with $10 \leq D_{pp} \leq 30$ nm. The results presented in Sect. 8 corroborate that this is a valid assumption and provides guidance for assessing the ice nucleation activity of atmospheric soot particles with similar properties. For PCF on soot aggregates characterized by smaller primary particles, five-membered or six-membered ring pores or even larger and more complex pore structures and cavities may become relevant. Indeed, Möhler et al. (2005a) showed that GSG soot with particle diameters of 70–140 nm and primary particle diameters as small as 4–8 nm proved to be efficient INPs around 210–220 K with freezing onsets as low as 110 % RH_i .

785 Soot-PCF requires pore space available for water to condense. Hydrophobic coatings can fill the pores and make them unavailable for PCF, as has been demonstrated recently for soot coated with different types of secondary organic material (Zhang et al., 2020). Similarly, ice nucleation by soot generated from propane flames was found to shift to higher ice supersaturation and eventually vanish with increasing organic carbon content (Crawford et al., 2011; Mahrt et al., 2018; Möhler et al., 2005b). More hydrophilic coatings such as strongly oxidized secondary organic material (Zhang et al., 2020) and sulfuric acid (Möhler et al., 2005b, 2005a) had a less prohibiting effect on the ice nucleation activity but nevertheless increased freezing onsets to higher relative humidity. At the same time, sulfuric acid aging can oxidize and/or remove organic material residing within the soot pores and thus enhance their susceptibility to take up water by capillary condensation and soot-PCF (Mahrt et al., 2020a). While the soot-PCF framework points to the relevance of the mixing state and coatings for the ice nucleation ability of soot, our present knowledge about these effects on soot-PCF is insufficient to draw final conclusions. The delicate dependency of soot-PCF on soot (pore) properties may indeed be the reason for the large uncertainties associated with the ice nucleation ability of soot and explain seemingly contradictory results between laboratory studies, when ice nucleation experiments with soot from various sources are compared. Additional studies are crucial to better constrain the effect of coatings depending on their thickness and hydrophobicity.

795 With its physical basis, the proposed soot-PCF framework has the potential to predict ice nucleation by soot based on physicochemical particle properties. For soot particles that are emitted from a variety of combustion sources, these properties indeed strongly depend on the fuel type and the combustion conditions (e.g. Atiku et al., 2016). Highly refined fuels used in road traffic (gasoline, diesel) and aircraft jet engines (kerosene) mostly contain hydrogen and carbon. When freshly emitted particles from these sources can be regarded as uncoated soot agglomerates, soot-PCF can be applied without restriction. However, soot particles from road traffic are emitted at ground level and need to be lifted to cirrus altitudes, throughout which condensation of semi-volatile organic material can occur, limiting or even preventing the applicability of soot-PCF. In case of thick coatings, immersion freezing should be the prevailing ice nucleation pathway, which has been shown to be ineffective in case of soot (Kanji et al., 2020; Schill et al., 2016). Conversely, aviation emissions constitute an in-situ source of high



number concentrations of soot particles in the upper troposphere where cirrus conditions prevail. Persistent contrails and the contrail cirrus clouds evolving from them, forming from water activation of aircraft-emitted soot particles and subsequent homogeneous freezing, are responsible for a major part of the radiative forcing from aviation (Kärcher, 2018). While their direct radiative forcing is relatively well represented in global climate models, little is known about the indirect effect, i.e. the potential of aircraft emitted soot particles to trigger or alter cirrus formation (Lee et al., 2020). After the contrail has dissipated under dry ambient conditions, processed and compacted soot aggregates are left behind, with an increased susceptibility to soot-PCF. Such soot particles may impact ice crystal number concentration and crystal size of cirrus clouds, in turn affecting cloud coverage, lifetime, and radiative forcing. A key uncertainty of previous estimates of aircraft-soot cirrus interactions is the ice nucleation efficiency of soot particles (Kärcher et al., 2007), both as a function of soot type and depending on aggregate size. In combination with a detailed cirrus cloud model, the soot-PCF framework presented here provides a physically based description of the ice nucleation ability and mechanism of soot with improved predictive capabilities, and as such opens up new avenues to address and reduce these uncertainties.

Because biomass is a chemically complex fuel, it produces particles of higher heterogeneity in terms of particle morphology and chemical composition compared to highly refined fuels. For instance, biomass burning usually emits soot together with large shares of organic combustion products, so that immediate internal mixing is likely, resulting in particles that are frequently mixed with inorganic species, mostly potassium salts (Li et al., 2003; Liu et al., 2017; Posfai et al., 2003) resulting in complex chemical composition (e.g. Liang et al., 2020). Nonetheless, under flaming conditions biomass burning has been found to emit relatively pure soot particles (Li et al., 2003; Posfai et al., 2003), that may form ice via soot-PCF. Given that combustion of biomass globally denotes an important source of carbonaceous particles, which are furthermore frequently found at cirrus level in the upper troposphere (Schill et al., 2020b), more studies are required to establish the share of sufficiently pure soot particles for soot-PCF to be effective.

10 Summary and conclusions

In this work, we have developed a new theoretical framework to describe ice nucleation by atmospherically relevant soot particles through PCF at cirrus conditions. Soot-PCF is a three-step process, where water is first taken up into the pores of soot aggregates, followed by homogeneous nucleation of the supercooled pore water, and subsequent growth of the pore ice into a macroscopic ice crystal, which can ultimately impact cloud-microphysics and radiative properties.

While previous work has inferred the susceptibility of soot to PCF from the dependence of freezing efficiency on temperature and relative humidity, the soot-PCF framework presented here goes a step further as it derives the ice nucleation activity of soot from particle properties, namely the aggregate size and compaction, the primary particle diameter and overlap coefficient, as well as the contact angle with water and ice (pore wettability). We find that n -membered ring pores are the dominant pore structures for soot-PCF, as they are common features of soot aggregates and have a suitable geometry for both, filling with water and growing ice below water saturation. We focused our analysis on three-membered and four-membered ring pores as



840 they are of the right size for PCF assuming primary particle sizes typical for atmospherically relevant soot. For these pores,
we have derived equations that describe the conditions for all three steps of soot-PCF, namely pore filling, ice nucleation, and
ice growth. We demonstrated that pore filling occurs via spontaneous gathering of pore water in the pore neck, which we
referred to as direct filling. For cirrus conditions, we assume that ice nucleation occurs immediately after the condensed water
volume is large enough to host a critical ice embryo, which has been shown to be the case when $T \leq 228$ K (David et al., 2019;
845 Mahrt et al., 2018, 2020b). Ice growth out of the pore sets a second thermodynamic barrier to PCF. While the critical
supersaturation for soot-PCF in narrow pores is limited by ice growth, the limiting step switches to capillary condensation for
wider pores. The width of ring pores increases with increasing primary particle size and decreases with increasing overlap.
Overall, the narrower three-membered ring pores tend to be ice growth limited, while the wider four-membered ring pores
tend to be limited by capillary condensation of water. With increasing hydrophobicity, both, capillary condensation and ice
850 growth shift to higher ice saturation ratios, making the contact angle between soot and water/ice a key parameter for soot-PCF.
Based on the characteristics of three-membered and four-membered ring pores, we have developed a framework to
parameterize the fraction of ice active soot particles. A key feature of the new parameterization is its capability to extrapolate
activated fractions measured for one mobility diameter to other aggregate sizes, and to predict ice activity of a soot sample
based on its physicochemical characterization. As such, we believe that it is of great advantage over previously reported
855 parameterizations, as it significantly reduces the complexity of the parameters and processes that need to be represented and
incorporated into climate models, by relying on a single fit function to represent the ice nucleation activity of differently sized
soot aggregates from the same emission source, i.e. with the same contact angle. The applicability of this framework is
supported by the excellent agreement of the derived parameterization and experiments, when simulating previously measured
laboratory data of ice formation by soot at cirrus temperatures. Our analysis further revealed that pre-activation by ice preserved
860 in soot pores is of limited relevance under cirrus conditions, because, when ice nucleation rates are high, its only effect is to
decrease the ice supersaturation required to activate those soot particles whose limiting step for PCF is capillary condensation.
However, when soot particles that have been pre-activated below the HNT encounter ice supersaturated conditions above the
HNT, the presence of pore ice allows to bypass the nucleation step enabling ice crystal formation from soot particles with no
intrinsic ice nucleation activity at MPC conditions. Ring pores have a limited potential to exhibit pre-activation, because the
865 pore ice is not preserved to low relative humidity and high temperatures. In contrast, the inner cavities between four
tetrahedrally or eight cubic arranged primary particles also described herein, are able to preserve ice to higher temperatures
and lower relative humidity because the large volume of the inner cavity prevents the ice from melting and the narrow pore
opening protects it from evaporation.

Overall, the soot-PCF framework provides strong constraints on the extent to which atmospheric soot particles depending on
870 their physicochemical properties contribute to ice nucleation. Consideration of this framework and incorporation of the new
parameterization in future modelling studies may vastly improve attempts to quantify the impact of soot-PCF on cirrus
microphysical properties and provide guidance to predict the radiative impact of soot via soot-cirrus interactions. Although we
only studied a number of idealized pore types formed between equally sized primary particles, the presented framework is able



875 to link previously reported ice nucleation experiments with the pore characteristics of the soot samples. Nonetheless, we
acknowledge that there remain a number of challenges for future studies to address. Arguably, uncertainties arise from the
soot-ice contact angle, and its relation to the soot-water contact angle. Future studies that aim at measuring contact angles on
soot surfaces should take into account surface structure, chemical composition and contact angle hysteresis. Further
uncertainties arise from the critical volume required for ice nucleation depending on temperature and relative humidity, and
the abundance of ring pores in soot aggregates in relation to their size and compaction. Moreover, we focused our investigation
880 on three-membered and four-membered ring pores made of equally sized primary particles. Analysis of other pore types
including pores between unequally sized primary particles might improve the assessment of ice activity of soot aggregates
depending on their size and compaction. While we have used available literature data to constrain our framework, further
experimental exploration is required, in particular on ambient soot particles.



885 Appendix A Pore geometry

A1 Pore geometry in tetrahedral packing arrangement

We start by analysing the pores formed between four primary soot particles out of a tetrahedral packing arrangement as illustrated in Fig. A 1. The centres A, B, C, and D of the four primary particles form the corners of an equilateral tetrahedron. This arrangement gives rise to two types of pores, namely the three-membered ring pore enclosed by the spheres making up
890 the triangle (ABC), whose dimensions we denote with the subscript tr , and the concave octahedron, the void in-between the tetrahedron enclosed by the spheres A, B, C, and D, whose dimensions we denote by the subscripts te . In the following we only consider pores formed between spheres of equal diameter.

Three-membered-ring pore

The three-membered-ring pore has the shape of a concave triangle (see Fig. A 1). The radii of its circumcircle, $r_{c,tr}$, and its
895 incircle, $r_{i,tr}$, can be determined from the diameter of the primary particles, D_{pp} , and the distance D_{ij} between the centres of two (overlapping) spheres. We start out by calculating the height, h_{tr} , of the equilateral triangle ABC:

$$h_{tr} = \frac{\sqrt{3}}{2} D_{ij}. \quad (\text{A } 1)$$

The radius of the circumcircle of the *concave* triangle, $r_{c,tr}$, can be expressed as a function of the incircle of the triangle ABC ($r_{i,tr}$) and the height of the overlap between the primary particles, h_{ov} , as illustrated in Fig. A 1:

$$r_{c,tr} = r_{i,tr} - h_{ov}. \quad (\text{A } 2)$$

The radius of the incircle is given by:

$$r_{i,tr} = \frac{1}{2\sqrt{3}} D_{ij}. \quad (\text{A } 3)$$

900 The height of the overlap, h_{ov} , can be expressed as a function of the angle ε_{ov} :

$$h_{ov} = \frac{\sin \varepsilon_{ov} D_{pp}}{2}. \quad (\text{A } 4)$$

Making use of the “trigonometric Pythagoras”, $\sin \varepsilon_{ov}$ can be expressed as:

$$\sin \varepsilon_{ov} = \sqrt{1 - \left(\frac{D_{ij}}{D_{pp}}\right)^2}. \quad (\text{A } 5)$$

Inserting Eq. (A 3) – (A 5) into Eq. (A 2) yields:

$$r_{c,tr} = \frac{1}{2\sqrt{3}} D_{ij} - \frac{D_{pp}}{2} \sqrt{1 - \left(\frac{D_{ij}}{D_{pp}}\right)^2}. \quad (\text{A } 6)$$

The radius of the circumcircle $r_{c,tr}$ coincides with the radius of the incircle in the absence of overlap of the primary particles. The radius of the opening of the concave triangle, $r_{o,tr}$, can be derived from the height of the triangle ABC, the radius of the
905 circumcircle of the concave triangle, and the primary particle diameter as:

$$r_{o,tr} = h_{tr} - r_{i,tr} - \frac{D_{pp}}{2} = \frac{\sqrt{3}}{2} D_{ij} - \frac{1}{2\sqrt{3}} D_{ij} - \frac{1}{2} D_{pp} = \frac{1}{\sqrt{3}} D_{ij} - \frac{1}{2} D_{pp}. \quad (\text{A } 7)$$



Setting Eq. (A 7) to zero yields $D_{ij} = \frac{\sqrt{3}}{2} D_{pp}$, which can be set into Eq. (1) to derive the overlap coefficient, for which the opening of the three-membered ring pore vanishes:

$$C_{ov} = \frac{D_{pp} - D_{ij}}{D_{pp}} = 1 - \frac{\sqrt{3}}{2} = 0.134. \quad (\text{A } 8)$$

Concave octahedron

910 The pore enclosed by the four primary particles located on the corners of the tetrahedron has the shape of a concave octahedron as depicted in Fig. A1. The height of the regular tetrahedron, h_{te} , with apices given by the centres of the spheres A, B, C, and D is given by:

$$h_{te} = \sqrt{\frac{2}{3}} D_{ij}. \quad (\text{A } 9)$$

The sphere with its origin at the centre of the tetrahedral cell reaches its maximum size when it comes in contact with the bodies of the primary particles. This maximum radius can be expressed as:

$$r_{o,te} = h_{te} - r_{i,te} - \frac{D_{pp}}{2}, \quad (\text{A } 10)$$

where $r_{i,te}$ is the radius of the insphere that is tangent to the faces of the regular tetrahedron given as:

$$r_{i,te} = \frac{D_{ij}}{\sqrt{24}} \quad (\text{A } 11)$$

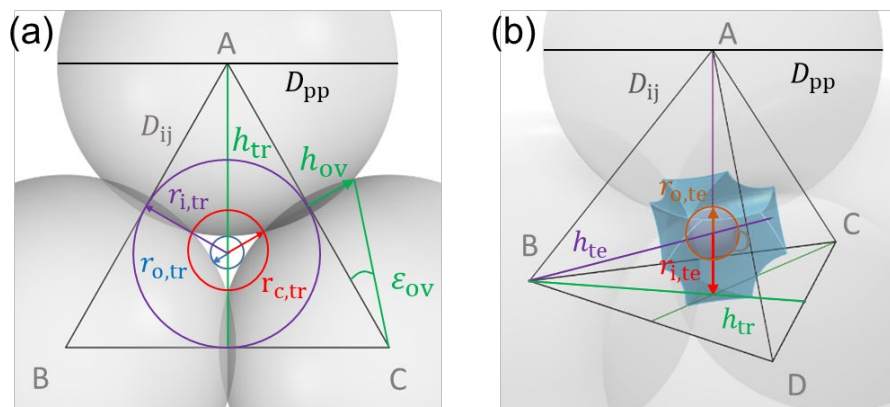
915 Inserting Eqs. (A 9) and (A 11) into Eq. (A 10) yields:

$$r_{o,te} = h_{te} - r_{i,te} - \frac{D_{pp}}{2} = \sqrt{\frac{2}{3}} D_{ij} - \frac{1}{\sqrt{24}} D_{ij} - \frac{D_{pp}}{2} = \frac{3D_{ij}}{\sqrt{24}} - \frac{D_{pp}}{2}. \quad (\text{A } 12)$$

Again, setting Eq. (A 12) to zero yields $D_{ij} = \sqrt{\frac{2}{3}} D_{pp}$, which can be inserted into Eq. (1) to yield the overlap coefficient for which the pore within the concave octahedron disappears:

$$C_{ov} = \frac{D_{pp} - D_{ij}}{D_{pp}} = 1 - \sqrt{\frac{2}{3}} = 0.184. \quad (\text{A } 13)$$

An overview of the pore dimensions formed for the case of a tetrahedral packing arrangement is given in Fig. 2a, showing $r_{o,tr}$, $r_{c,tr}$ and $r_{o,te}$ for different sphere (primary particle) sizes as a function of overlap.



925 **Figure A 1:** Dimensions of the different pore types formed in the case of a tetrahedral packing arrangement, where four overlapping spheres of diameter D_{pp} are arranged on the corners of a regular tetrahedron, indicated by A, B, C, and D. **(a)** Top view of the three-membered ring pore that forms between the three spheres with centres at the corners of the triangle A, B and C. **(b)** The inner cavity formed within the tetrahedral cell with apices at the centres of the spheres A, B, C and D has the form of a concave octahedron.

A2 Pore geometry in tetrahedral packing arrangement

The case of a cubic packing arrangement of overlapping spherical particles is depicted in Fig. A 2, showing in panel (a) the top view of four overlapping particles forming a square with corners A, B, C, and D, that denote the centers of neighbouring spheres within the same lattice layer (plane). In this packing arrangement the centres of spheres among different lattice layers are aligned with each other across the different layers. The cubic packing gives rise to two types of pores. Four-membered ring pores arise as the cavity formed between the spheres making up the square ABCD. We use the subscript *sq* to refer to the dimensions within this pore type. Another type of pores originates as the concave cube, i.e. the void in-between eight spheres formed between two sets of four neighbouring spheres in adjacent lattice layers, and we denote the dimensions of this pore by the subscript *cu*.

935 Four-membered ring pore

The four-membered ring pore has the shape of a concave square. The radii of its circumcircle, $r_{c,sq}$, and its incircle, $r_{i,sq}$, can be calculated from the diameter of the primary particles, D_{pp} , and the distance between the centres of the overlapping spheres, D_{ij} , similar to the case of the three-membered ring pore. The radius of the circumcircle of the concave square can be expressed as a function of the incircle of the square ABCD and the height of the overlap between two adjacent spheres, as shown in Fig. A

$$940 \quad r_{c,sq} = r_{i,sq} - h_{ov}. \quad (\text{A } 14)$$

Here, the radius of the incircle of the square ABCD, $r_{i,sq}$, is directly given by the half-width of the distance along the centres of two overlapping spheres as:

$$r_{i,sq} = \frac{1}{2} D_{ij}. \quad (\text{A } 15)$$



The height of the overlap can be calculated from the angle ε_{ov} , analogously to the case of the three-membered ring pore and is given by Eq. (A 4). Based on this, the radius of the circumcircle can be expressed as:

$$r_{c,sq} = \frac{1}{2}D_{ij} - h_{ov} = \frac{1}{2}D_{ij} - \frac{\sin \varepsilon_{ov} D_{pp}}{2} = \frac{1}{2}D_{ij} - \frac{D_{pp}}{2} \sqrt{1 - \left(\frac{D_{ij}}{D_{pp}}\right)^2}. \quad (\text{A } 16)$$

945 The radius of the circumcircle of the concave square, $r_{c,sq}$, coincides with the radius of the incircle of the square ABCD, $r_{i,sq}$, in the absence of overlap, i.e. $h_{ov} = 0$. The radius of the incircle of the concave square, $r_{o,sq}$, describing the radius of the pore opening, is given by:

$$r_{o,sq} = \frac{\sqrt{2}}{2}D_{ij} - \frac{1}{2}D_{pp}. \quad (\text{A } 17)$$

Here, $\sqrt{2}/2D_{ij}$ is the half-length of the diagonal of the square ABCD (see Fig. A 2). Setting Eq. (A 17) to zero yields $\sqrt{2}D_{ij} = \frac{1}{\sqrt{2}}D_{pp}$, which can be inserted into Eq. (1) to obtain the value of the overlap coefficient for which the pore opening of the four-

950 membered ring pore vanishes:

$$C_{ov} = \frac{D_{pp} - D_{ij}}{D_{pp}} = 1 - \frac{1}{\sqrt{2}} = 0.293. \quad (\text{A } 18)$$

Concave cube

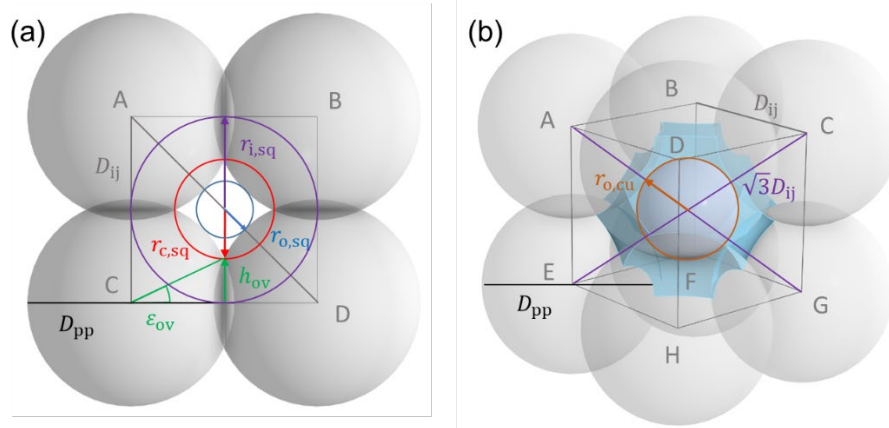
Considering two adjacent layers of the cubic packing arrangement, a cavity is formed between eight primary particles arranged on the corners of a cube (A – H, see Fig. A 2b). The enclosed pore has the shape of a concave cube. The center of a sphere that can be placed within this concave cubic cell is located along the space diagonal of the cube spanned by the eight spheres, given
955 by $\sqrt{3}D_{ij}$. Accordingly, the radius of the sphere that is in point contact with the bodies of the primary particles is given by:

$$r_{o,cu} = \sqrt{3}D_{ij} - D_{pp}. \quad (\text{A } 19)$$

Setting Eq. (A 19) to zero yields $D_{ij} = \frac{1}{\sqrt{3}}D_{pp}$ and consequently the overlap for which the pore in the dented concave cube disappears becomes:

$$C_{ov} = \frac{D_{pp} - D_{ij}}{D_{pp}} = 1 - \frac{1}{\sqrt{3}} = 0.423. \quad (\text{A } 20)$$

An overview of the various pore dimensions formed for the case of a cubic packing arrangement is given in Fig. 2b, showing $r_{o,sq}$, $r_{c,sq}$ and $r_{o,cu}$ for different sphere (primary particle) sizes and as a function of overlap.



960

Figure A 2: Dimensions of the different pore types formed in the case of a cubic packing arrangement of overlapping spheres with diameter D_{pp} . (a) Top view of the four-membered ring pore that forms between the four spheres with centres at the corners of the square A, B, C, D. (b) The inner cavity formed within the cubic cell between eight neighbouring spheres of two lattice layers has the form of a concave cube (blue shading).

965 Appendix B Pore filling with liquid water and ice

B1 Kelvin equation for conical and cylindrical pores

Water in capillaries exhibits a curved surface, a so-called meniscus that stabilizes it with respect to bulk water. Similarly, the stabilization of ice in narrow pores can be described by its surface curvature. The radius of the curvature is related to the equilibrium vapour pressure above the curved surface through the Kelvin equation (Kelvin, 1904; Thomson, 1871). The Kelvin equation relies on the Young-Laplace equation (Laplace et al., 1829; Young, 1805), which describes the pressure difference, ΔP , across the interface between the curved surface and the surrounding water vapour. In its general form the Young-Laplace equation can be written as:

970

(B 1)

$$\Delta P = P - P_0 = \gamma(T) C = \gamma(T) \left(\frac{1}{r_{c1}} + \frac{1}{r_{c2}} \right),$$

where $\gamma(T)$ is the interfacial tension between the condensed phase (water or ice) and water vapour (in case of liquid water: $\gamma_{vw}(T)$; in case of ice: $\gamma_{vi}(T)$), P is the absolute pressure within the condensed phase, P_0 the standard pressure and ΔP the difference in pressure. C denotes the curvature of the interface, which can be expressed by r_{c1} and r_{c2} describing the principal radii of curvature of the condensate. Concave curvatures of the condensed surface (negative radii of curvature) are indicative of a negative absolute pressure within the condensed phase. In contrast, in the case of spherical droplets (or minuscule ice crystals), the convex surface (positive radius of curvature) goes along with positive (increased) absolute pressure within the droplet (ice crystal).

975

980 The Kelvin equation in its general form is given as (see e.g. Appendix A2 in Marcolli, 2020, for a detailed derivation):

$$\frac{p}{p_{w/i}}(T) = \exp \left(\frac{\gamma_{vw/i}(T) \left(\frac{1}{r_{c1}} + \frac{1}{r_{c2}} \right) v_{w/i}(T)}{kT} \right). \quad (\text{B } 2)$$



Here, the subscript w/i can either refer to w (liquid water) or i (ice), to indicate the Kelvin equation with respect to liquid water or ice, respectively. Hence, $p/p_{w/i}(T) = S_{w/i}$, with p and $p_{w/i}$ describing the water vapour pressure and the equilibrium water/ice vapour pressure, k is the Boltzmann constant, and $v_{w/i}(T)$ is the molecular volume of liquid water/ice. If the two principal radii of curvature are identical, i.e. $r_{c1} = r_{c2} = r_c$, the term in the nominator describing the curvature of the interface becomes $2/r_c$.

985 Cylindrical pores

In the case of cylindrical and conical pores, there is only one principal axis of curvature describing the concave water or ice surface of capillary condensates (Fig. B 1). The shape of the water/ice surfaces formed in such pore geometries is a classical problem (de Gennes, 1985). In addition to the pore geometry, capillary condensation also depends on the wettability of the material making up the pore given by the contact angle $\theta_{sw/i}$, describing the angle between the water/ice surface and the pore wall (i.e. substrate (s) surface). For cylindrical pores with constant pore diameter D_p , as shown in Fig. B 1 a, pore filling occurs at a concave water/ice surface with radius:

$$r_c = \frac{-D_p}{2 \cos \theta_{sw/i}}, \quad (\text{B } 3)$$

and the *RH* of pore filling can be calculated as:

$$\frac{p}{p_{w/i}} = \exp \left(- \frac{\gamma_{vw/i}(T) \left(\frac{4 \cos \theta_{sw/i}}{D_p} \right) v_{w/i}(T)}{kT} \right). \quad (\text{B } 4)$$

The dependence of pore filling on the pore diameter and the contact angle is illustrated in Fig. B 2 a and b, for the case of water condensation, showing the saturation ratio with respect to water, S_w , calculated from Eq. (B 4). For a given pore diameter, cylindrical pores with lower contact angle fill at lower RH_w compared to pores with higher contact angle. We reiterate that for $\theta_{sw/i} > 90^\circ$ the pore water or ice exhibits a convex curvature, associated with an equilibrium vapour pressure that is larger than the bulk vapour pressure.

Conical pores

While cylindrical pores fill completely when the *RH* of pore filling is reached, conical pores fill gradually. Their filling level depends on the pore diameter at the level of the water/ice surface, the pore opening angle, δ , which is constant for conical pores (see Fig. B 1 b), and the contact angle:

$$r_c = \frac{-D_p}{2 \cos(\theta_{sw/i} + \delta)}. \quad (\text{B } 5)$$

Thus, pore filling takes place up to the pore diameter $D_p = -2r_c \cos(\theta_{sw/i} + \delta)$. Accordingly, the Kelvin equation for conical pores is given by:



(B 6)

$$\frac{p}{p_{w/i}} = \exp\left(-\frac{\gamma_{vw/i}(T)(4 \cos(\theta_{sw/i} + \delta))v_{w/i}(T)}{D_p kT}\right).$$

1005 Figure B 2 illustrates the effect of the pore opening angle on the water saturation ratio required for pore filling for the example
 of a pore of 8 nm diameter. For $\delta = 0^\circ$, the geometries of cylindrical and conical pores are the same, and consequently the pore
 filling conditions are the same. For a given contact angle, increasing the pore opening angles causes the RH_w for pore filling
 to increase, as the radius of the concave meniscus increases. Similar to the case of the cylindrical pore, the RH_w required for
 pore filling decreases with decreasing contact angle. Inspection of Eq. B 5 reveals that an increase of the pore opening angle
 has the same effect on r_c as an increase of the contact angle by the same amount, since the two angles add up within the cosine.

1010

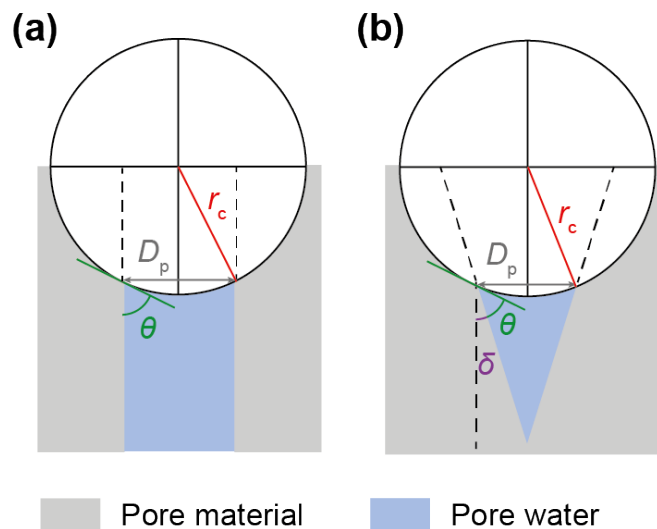
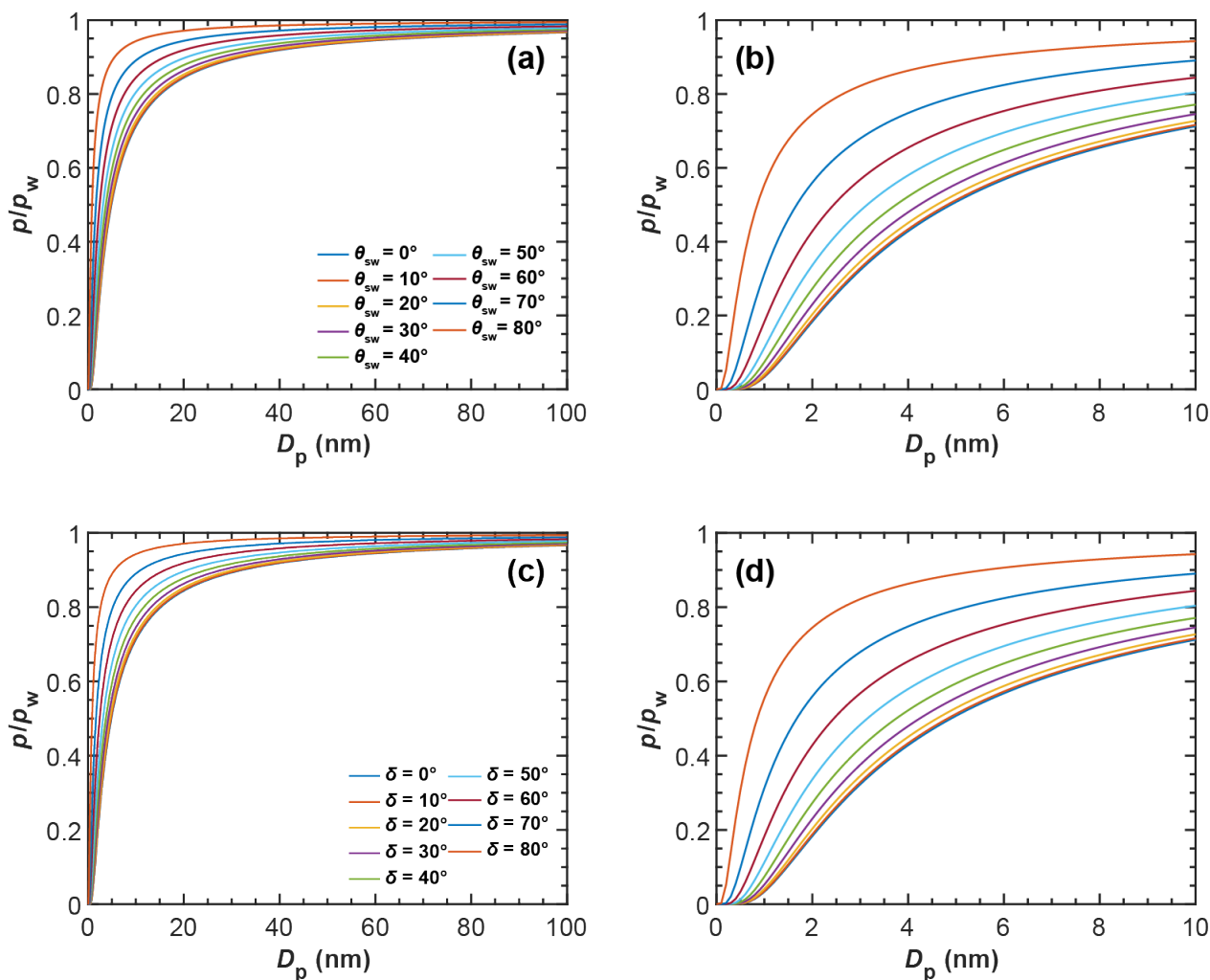


Figure B 1: Illustration of radius of curvature r_c of (a) cylindrical and (b) conical pores with pore diameter D_p , contact angle θ_{sw} , and pore opening angle δ . For the cylindrical pore, $\delta = 0^\circ$.



1015

Figure B 2: Influence of contact angle and pore opening on pore filling for cylindrical and conical pores. **(a, b)** Saturation ratio with respect to water (p/p_w) required to fill cylindrical pores with different water-soot contact angles (θ_{sw}), as a function of the pore diameter (D_p). **(c, d)** Saturation ratio with respect to water required to fill a conical pore with different opening angles (δ) to the level D_p , for a fixed value of $\theta_{sw} = 0^\circ$. Panels (b) and (d) are zooms of panels (a) and (c), respectively. All lines are calculated for $T = 220$ K. The relation between the water-soot and ice-soot contact angle is given in Appendix C.

1020



B2 Slit filling between two adjacent primary particles with liquid water

1025 The slit forming between two neighboring, overlapping primary particles is shown in Fig. B 3. The water meniscus takes the form of a pendular ring with two principle radii of curvature, that can be related to the height and the width of the filling level of the slit, h_{fl} and d_{fl} , respectively (e.g. Gladkikh and Bryant, 2003; Huang et al., 2015; Persiantseva et al., 2004), which are independent of each other. The height of slit filling, h_{fl} , can be expressed as a function of the primary particle diameter D_{pp} and the slit filling angle ε as depicted in Fig. B 3a:

$$h_{fl} = \frac{D_{pp}}{2} \sin \varepsilon. \quad (\text{B } 7)$$

The height of the filling level, h_{fl} , corresponds to the radius of the pendular ring of water condensed within the slit between the two particles and consequently yields a convex (positive) curvature:

$$r_{c1} = \frac{D_{pp} \sin \varepsilon}{2}. \quad (\text{B } 8)$$

1030 As the pendular ring is closed in itself, there is no contact angle to be considered.

The expression for the second principal radius of curvature can be derived from evaluating the width of the pendular ring where it contacts the surface of the spherical particles given as $d_{fl} = D_{ij} - D_{pp} \cos \varepsilon$. Since the water surface along this axis spans a “bridge” between the two primary particles, the radius of curvature depends on the contact angle and the pore opening angle δ , which coincides with the slit filling angle ε , i.e. $\delta = \varepsilon$:

$$r_{c2} = \frac{-D_{ij} + D_{pp} \cos \varepsilon}{2 \cos(\theta_{sw} + \varepsilon)}. \quad (\text{B } 9)$$

1035 Thus, unlike the pore opening angle of conical pores, the slit opening angle is not constant but increases with increasing slit filling. As a consequence, the radius of curvature r_{c2} switches from concave to convex during pore filling when $(\theta_{sw} + \varepsilon) > 90^\circ$. Inserting Eqs. (B 8) and (B 9) into the general expression of the Kelvin equation given in Eq. (B 2) finally yields the Kelvin equation describing the filling of the slit-shaped pore formed between two neighboring, spherical particles via a pendular water ring:

$$\frac{p}{p_w} = \exp \left(\frac{\gamma_{vw}(T) \left(\frac{2}{D_{pp} \sin \varepsilon} + \frac{2 \cos(\theta_{sw} + \varepsilon)}{-D_{ij} + D_{pp} \cos \varepsilon} \right) v_w(T)}{kT} \right). \quad (\text{B } 10)$$

1040

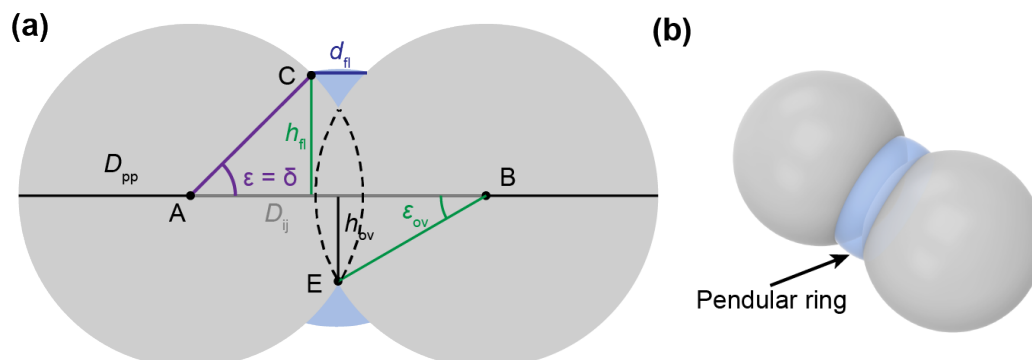


Figure B 3: (a) Two dimensional illustration of the slit-shaped pore formed between two overlapping spherical particles of the diameter D_{pp} . The liquid water phase forms a pendular ring of water. The two principal radii of curvature of the pendular water ring are given by r_{c1} and r_{c2} that are related to h_{fi} and d_{fi} , respectively (see text for details). (b) The three dimensional shape of the pendular ring can be obtained by revolving the slit-shaped water phase (blue) about the axis described by the line between points A and B. Represented in panel (b) is a ring corresponding with a contact angle of $\theta_{sw} = 60^\circ$.

B3 Pore filling via pendular rings for three-membered and four-membered ring pores

Ring pores form between circles of primary particles that are in contact with each other. Figure 1 in the main text depicts the pore opening of three-membered and four-membered ring pores. At each of the contacts between the primary particles, pendular rings of water form as RH increases. As discussed above, each pendular ring is described by the two principal radii of curvature given in Eqs. (B 8) and (B 9), that are related to the height and the width of the filling level, respectively. As the RH increases the pendular water ring increases in volume, continuously rising from the narrowest part of the pore slit (see Fig. B 3) according to an increase of the slit filling angle, ε . In the case of three-membered ring pores, coalescence of the three pendular rings and complete filling of the ring pore is assumed to take place when $\varepsilon = 30^\circ$ is reached, while water filling up to $\varepsilon = 45^\circ$ is assumed for four-membered ring pores to fill.

Figure B 4 shows the filling levels of the slits as a function of the slit filling angle, ε , for increasing saturation ratio with respect to water (p/p_w) for primary particle diameters of $D_{pp} = 10, 20$ and 30 nm and different soot-water contact angles, θ_{sw} . The lines in Fig. B 4 are calculated using Eq. (B 10) assuming overlaps of $C_{ov} = 0.01, 0.05$, and 0.1 . We stress that water uptake only starts for $\varepsilon > \varepsilon_{ov}$. Comparison of the different panels in Fig. B 4 reveals that the curves of the water uptake become steeper with increasing overlap. Figure B 4 clearly shows that in order to reach the conditions for three-membered ring-pore filling ($\varepsilon = 30^\circ$) and four-membered ring-pore filling ($\varepsilon = 45^\circ$) below water saturation, relatively low soot-water contact angles are required. Specifically, soot-water contact angles of $\theta_{sw} < 50^\circ$ for three-membered ring pores and $\theta_{sw} < 30^\circ$ for four-membered ring pores are needed for pore filling via pendular water rings. This makes the filling of ring pores via pendular rings an ineffective process for porous aerosol particles with (rather) high contact angles such as soot aggregates.

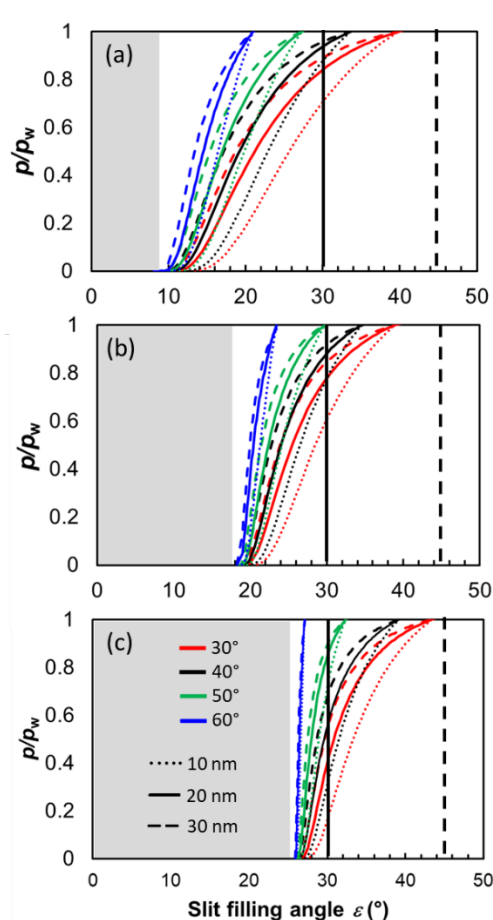


Figure B 4: Saturation ratio with respect to water ($S_w = p/p_w$) required for filling of three-membered and four-membered ring pores as a function of slit-filling angle ε at $T = 220$ K for **(a)** $C_{ov} = 0.01$, **(b)** $C_{ov} = 0.05$, and **(c)** $C_{ov} = 0.1$. Primary particle diameters $D_{pp} = 10$ – 30 nm and soot-water contact angles $\theta_{sw} = 30$ – 60° are shown as indicated in the legend. For a slit-filling of $\varepsilon = 30^\circ$ (solid black vertical line) and $\varepsilon = 45^\circ$ (dashed black vertical line), the pendular water rings coalesce resulting in complete filling of the pore opening for the three-membered and four-membered ring pores, respectively. The grey shaded area indicates the range of overlap between primary particles which extends to $\varepsilon_{ov} = 8.11^\circ$ for $C_{ov} = 0.01$, $\varepsilon_{ov} = 18.19^\circ$ for $C_{ov} = 0.05$, and $\varepsilon_{ov} = 25.84^\circ$ for $C_{ov} = 0.1$.

B4 Direct filling of three-membered ring pore (tetrahedral arrangement)

The side view in Fig. B 5 shows that the three-membered ring pore is constrained towards all sides up to the end of the overlap given by the height h_{ov} . It widens with increasing distance from the midplane as the radii of the spherical layers (i.e. D_n) decrease, hence the size of the concave triangle increases. Capillary condensation by direct filling is expected to start at the narrowest part, which we refer to as the pore neck. First pore filling originates from random fluctuating slit water and water patches that coalesce spontaneously when the RH for pore filling is reached. As the ambient RH further increases, the filling level (h_n) gradually raises. Once the water has frozen, ice growth occurs along the same coordinate, so that the filling of the three-membered ring-pore with either liquid water or ice can be described the same way. We track the filling level as a function of ε as depicted in Fig. B 5b. As the pore has a three-fold symmetry, there is only one independent radius of curvature describing



the interface between the condensed phase (either liquid or ice) and the vapour phase. We assume that the radius $r_{fl,tr}$ and the contact angle between soot and the condensed phase determine the filling level as a function of RH . From the side view shown in Fig. B 5b the radius of the pore opening at height h_{fl} above the midplane can be written as:

$$r_{fl,tr} = h_{tr} - r_{i,tr} - \frac{D_{fl}}{2}. \quad (B 11)$$

1085 D_{fl} can be expressed as a function of ε :

$$D_{fl} = D_{pp} \cos \varepsilon. \quad (B 12)$$

Note, that the slit-filling angle ε and the filling level, h_{fl} as given in Eq. (B 7), are related via $\varepsilon = \arcsin 2h_{fl}/D_{pp}$.

The expressions for h_{tr} and $r_{i,tr}$ are given in Eqs. (A 1) and (A 3), respectively, such that:

$$r_{fl,tr} = \frac{\sqrt{3}D_{ij}}{2} - \frac{D_{ij}}{2\sqrt{3}} - \frac{D_{pp} \cos \varepsilon}{2} = \frac{2D_{ij} - \sqrt{3}D_{pp} \cos \varepsilon}{2\sqrt{3}}. \quad (B 13)$$

To obtain the radius of curvature of the water/ice surface of three-membered ring pores, the contact angle and the pore opening angle need to be considered additionally, leading to the principal radius of curvature, $r_{c,fl,tr}$:

$$r_{c,fl,tr} = \frac{-2D_{ij} + \sqrt{3}D_{pp} \cos \varepsilon}{2\sqrt{3} \cos(\theta_{sw/i} + \varepsilon)}. \quad (B 14)$$

1090 Finally, inserting Eq. (B 14) into Eq. (B 2), the general form of the Kelvin equation describing the equilibrium vapour pressure over the surface of the filled three-membered ring pore yields:

$$\frac{p}{p_{w/i}} = \exp \left(\frac{\gamma_{vw/i}(T) \left(\frac{4\sqrt{3} \cos(\theta_{sw/i} + \varepsilon)}{-2D_{ij} + \sqrt{3}D_{pp} \cos \varepsilon} \right) v_{w/i}(T)}{kT} \right). \quad (B 15)$$

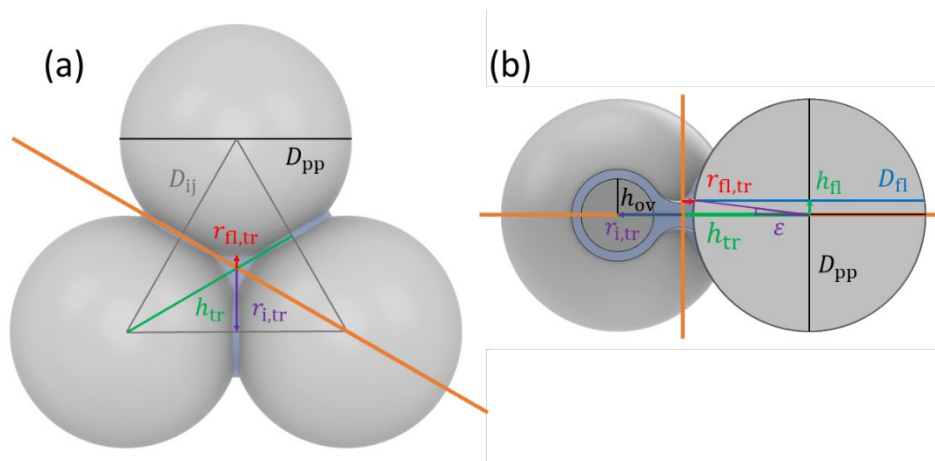


Figure B 5: Illustration of filling of a three-membered ring pore in (a) top view and (b) side view. The orange line indicates the cross section shown in panel (b). The pore filling is illustrated for a liquid water filling level to $h_f = 1.25$ nm, but the same geometry also applies for filling the pore with ice.

1095

B5 Direct filling of four-membered ring pore (cubic arrangement)

In analogy to Appendix B4, in this section we derive expressions for the conditions of a four-membered ring pore to fill with liquid water or ice. Similar to the three-membered ring pore, the filling level will gradually rise with increasing RH . Again, the ambient RH and the contact angle of soot and the condensed phase (water or ice) determine the filling level and hence the radius of curvature of the interface. The four-membered ring pore shown in Fig. B 6a has a four-fold symmetry. Since non-orthogonal radii of curvature equalize, a surface of constant curvature will form. This surface can be described by one principal radius of curvature analogously to the case of the three-membered ring pore. Considering the side view shown in Fig. B 6b an expression for the radius of the pore opening at height h_{fl} above the midplane is given by:

1100

(B 16)

$$r_{fl,sq} = \frac{\sqrt{2}}{2} D_{ij} - \frac{D_{fl}}{2},$$

with $\sqrt{2}D_{ij}$ describing the diagonal of the square between the centres of the spheres ABCD and D_{fl} denoting the diameter of a cross section of a spherical particle at the filling height h_{fl} above the midplane. Using Eq. (B 12) $r_{fl,sq}$ is given by:

1105

(B 17)

$$r_{fl,sq} = \frac{\sqrt{2}}{2} D_{ij} - \frac{D_{fl}}{2} = \frac{\sqrt{2}D_{ij}}{2} - \frac{D_{pp}\cos\epsilon}{2}$$

With Eq. (B 3) the principal radius of curvature is given by:

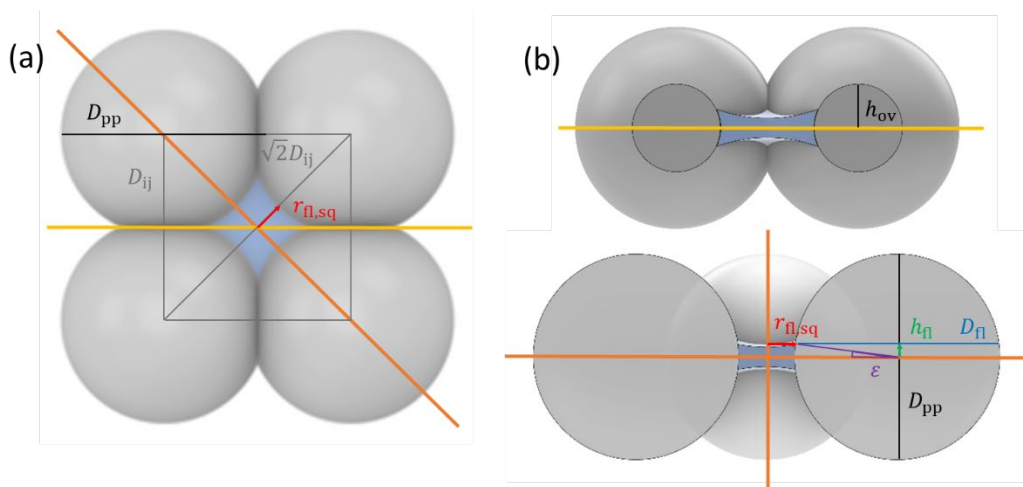
(B 18)

$$r_{c,fl,sq} = \frac{-\sqrt{2}D_{ij} + D_{pp}\cos\epsilon}{2\cos(\theta_{sw/i} + \epsilon)}.$$

Finally, inserting the expression for $r_{c,fl,sq}$ into Eq. (B 2) we obtain the general form of the Kelvin equation that can be used to calculate the RH of filling of the four-membered ring pore given by:



$$\frac{p}{p_{w/i}} = \exp \left(\frac{\gamma_{vw/i}(T) \left(\frac{4 \cos(\theta_{sw/i} + \varepsilon)}{-\sqrt{2} D_{ij} + D_{pp} \cos \varepsilon} \right) v_{w/i}(T)}{kT} \right). \quad (\text{B } 19)$$



1110

Figure B 6: Illustration of filling of a four-membered ring pore in (a) top view and (b) side views. Bright and dark orange lines indicate the cross sections shown in the side views depicted in panel (b). The pore filling is illustrated for a liquid water filling level to $h_f = 1.25$ nm, but the same geometry also applies for filling the pore with ice.

Appendix C Water soot and ice soot contact angles

1115 The contact angle between soot and water, θ_{sw} , is illustrated in Fig. C 1a and can be written as:

$$\cos \theta_{sw}(T) = \frac{\gamma_{vs}(T) - \gamma_{sw}(T)}{\gamma_{vw}(T)}, \quad (\text{C } 1)$$

where $\gamma_{vs}(T)$, $\gamma_{sw}(T)$ and $\gamma_{vw}(T)$ denote the interfacial tensions between water vapour and soot, soot and water and water vapour and water, respectively. The contact angle between ice and water, θ_{iw} , can be written as:

$$\cos \theta_{iw}(T) = \frac{\gamma_{vw}(T) - \gamma_{iw}(T)}{\gamma_{vi}(T)}, \quad (\text{C } 2)$$

where $\gamma_{iw}(T)$ and $\gamma_{vi}(T)$ are the interfacial tensions between ice and water, and water vapour and ice, respectively. In a similar manner, the contact angle between soot and ice can be expressed as:

$$\cos \theta_{si}(T) = \frac{\gamma_{vs}(T) - \gamma_{si}(T)}{\gamma_{vi}(T)}, \quad (\text{C } 3)$$

1120 where $\gamma_{si}(T)$ and $\gamma_{vi}(T)$ are the interfacial tensions between soot and ice and water vapour and ice, respectively. While the surface tension of water can be readily measured (e.g. Wei et al., 2017), the surface tension of ice is not well known. Here, we follow the approach of David et al. (2019) and assume a quasi-liquid-layer to form on the ice surface (Nenow and Traynov, 1986). In this case, an upper limit for the interfacial tension between water vapour and ice can be approximated by (David et al., 2019):

$$\gamma_{vi}(T) = \gamma_{vw}(T) + \gamma_{iw}(T). \quad (\text{C } 4)$$



1125 Similarly, we assume an upper limit for the surface tension of the soot-ice interface to be given by:

$$\gamma_{si}(T) = \gamma_{sw}(T) + \gamma_{iw}(T). \quad (\text{C } 5)$$

Making use of Eqs. (C 4) and (C 5) we can express the ice-soot contact angle in Eq. (C 3) as a function of the soot-water contact angle:

$$\cos \theta_{si}(T) = \frac{\gamma_{vs}(T) - \gamma_{sw}(T) - \gamma_{iw}(T)}{\gamma_{vi}(T)} = \frac{\gamma_{vw}(T) \cos \theta_{sw}(T) - \gamma_{iw}(T)}{\gamma_{vi}(T)}. \quad (\text{C } 6)$$

In Fig. C 1 the expression in Eq. (C 6) is evaluated, for a range of cirrus relevant temperatures. Here, $\gamma_{vw}(T)$ was calculated using the parameterization given in Hrubry et al. (2014), that is based on the work of Vargaftik et al. (1983), and $\gamma_{iw}(T)$ was

1130 calculated using the parameterization given in Ickes et al. (2015).

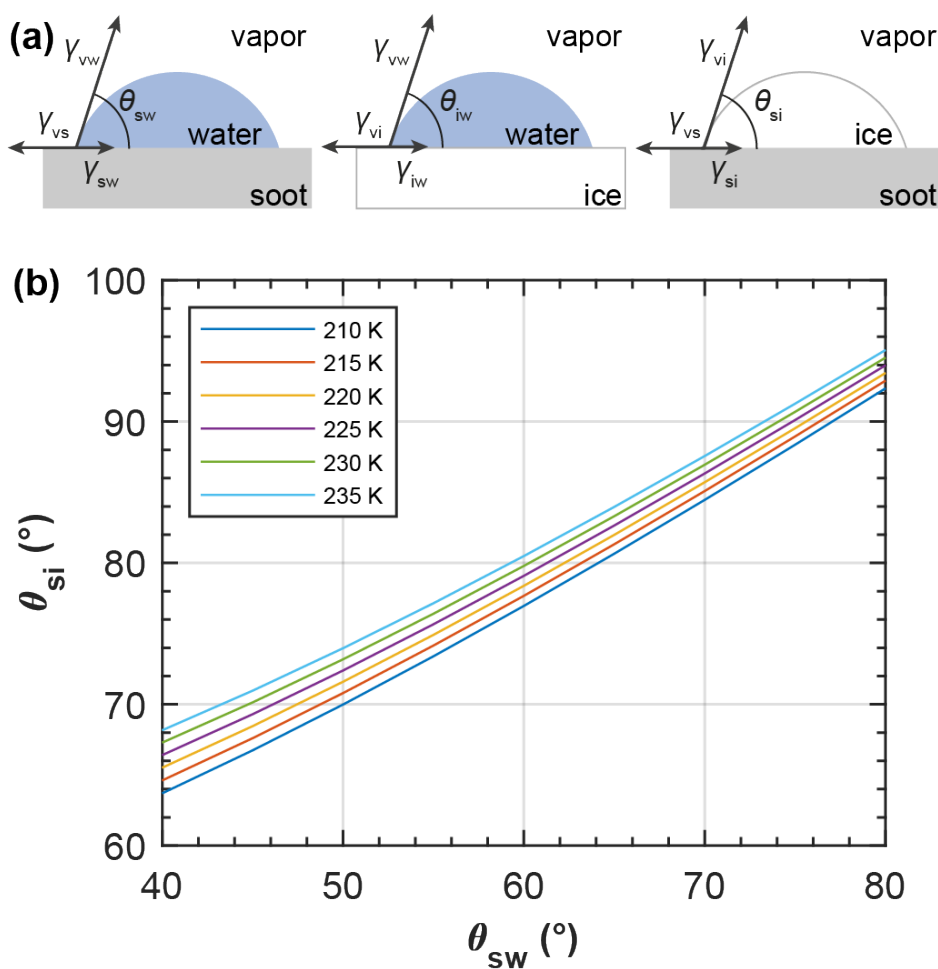


Figure C 1: (a) Illustration of the contact angles of water on soot (θ_{sw}), ice on water (θ_{iw}), and ice on soot (θ_{si}). (b) Soot-ice contact angle as a function of the soot-water contact angle for different temperatures, as indicated in the legend, calculated using Eq. (C 6).



1135 Appendix D Ice growth out of ring pores

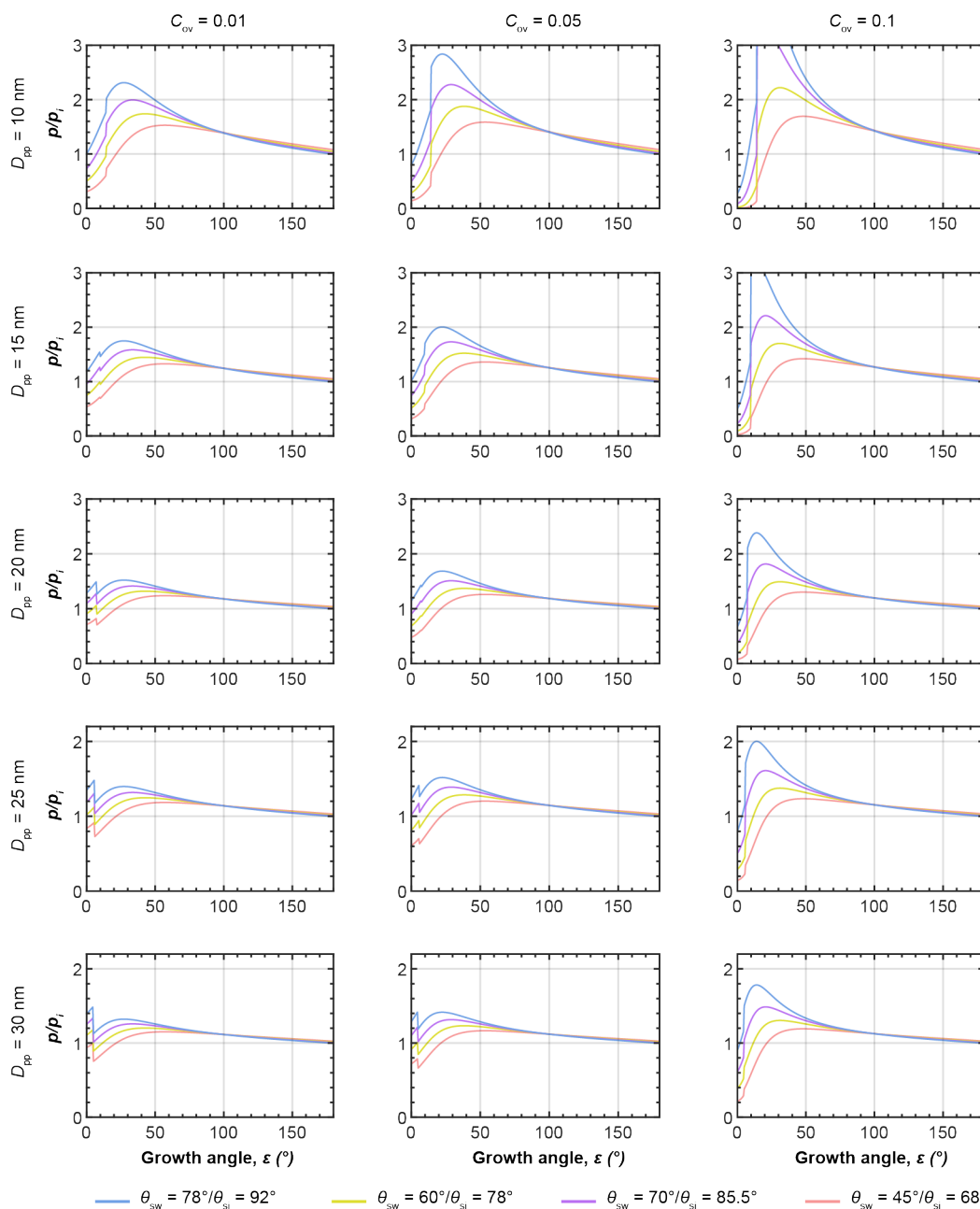


Figure D 1: Saturation ratio with respect to ice ($S_i = p/p_i$) required for (1) filling of three-membered ring pores, followed by (2) growth of pore ice up to the top of the sphere and beyond the height of the three-membered ring pore structure, as detailed in Fig. 5 and described in the main text. The individual panels correspond to different values of the overlap coefficient (C_{ov} , columns) and primary particle diameters (D_{pp} , rows). Within each panel the curves correspond to different values for the contact angle between soot and water (θ_{sw}) and soot and ice (θ_{si}), as indicated in the legend. All calculations were performed for $T = 220$ K.

1140

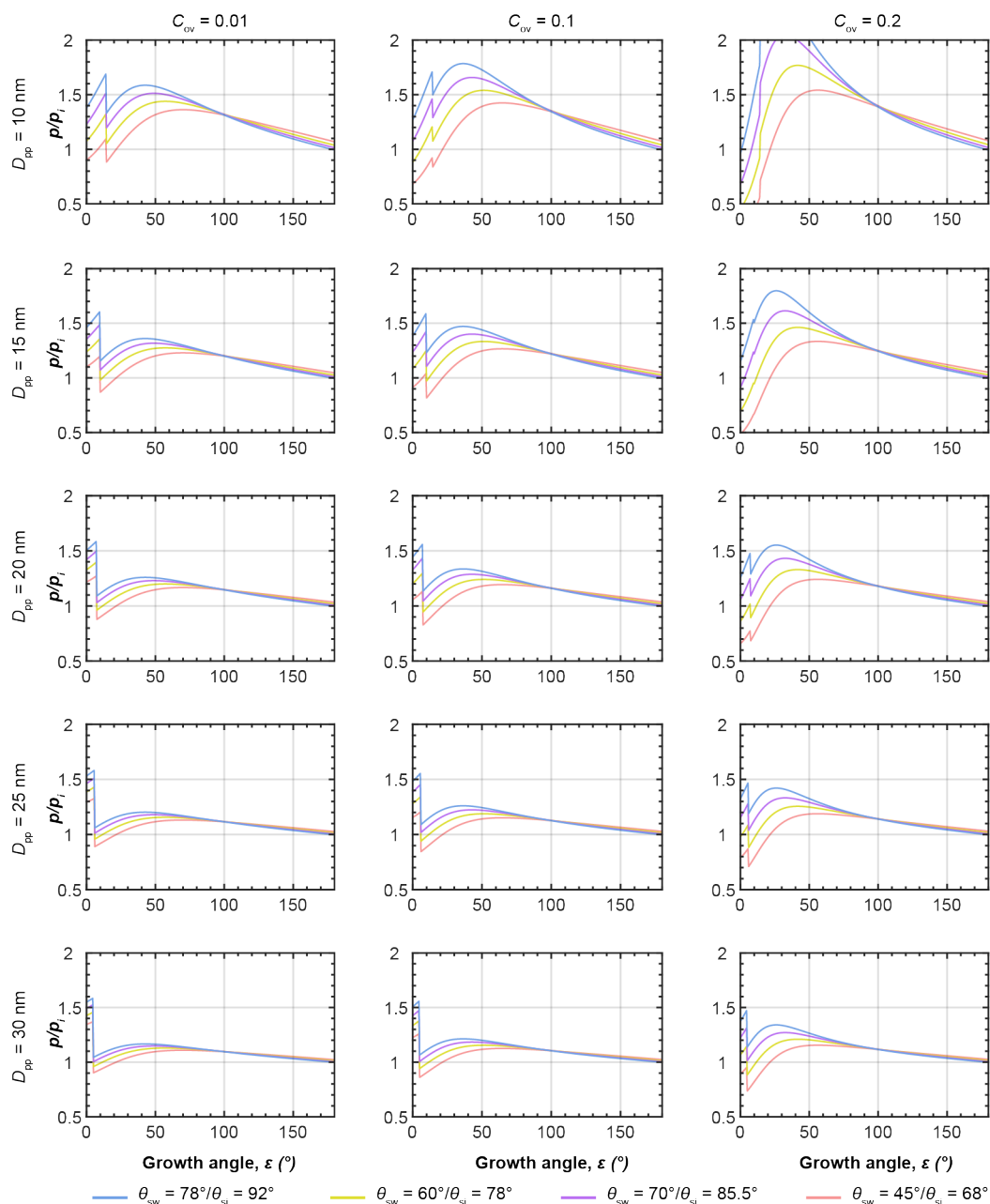


Figure D2: Saturation ratio with respect to ice ($S_i = p/p_i$) required for (1) filling of four-membered ring pores, followed by (2) growth of pore ice up to the top of the sphere and beyond the height of the four-membered ring pore structure, as detailed in Fig. 5 and described in the main text. The individual panels correspond to different values of the overlap coefficient (C_{ov} , columns) and primary particle diameters (D_{pp} , rows). Within each panel the curves correspond to different values for the contact angles between soot and water (θ_{sw}) and soot and ice (θ_{si}), as indicated in the legend. All calculations were performed for $T = 220$ K.

1145



Appendix E Soot-PCF parameterization for ice active fraction of soot aggregates

1150 The ability of a soot aggregate to nucleate ice via PCF depends on the availability of pores and the type (ring-structure) of pores present in a soot aggregate. The number of pores in a soot aggregate in turn increases with the number of primary particles within an aggregate and the degree of compaction, which can be described by the fractal dimension. To calculate the number of primary particles, N_p , in soot aggregates, we follow Sorensen (2011):

$$N_p = k_0 \left(\frac{2R_g}{D_{pp}} \right)^{D_f} \quad (\text{E } 1)$$

1155 Here k_0 is the scaling pre-factor, D_{pp} is the median primary particle size of an aggregate, D_f is the fractal dimension. Previous work has shown that soot aggregates formed through diffusion limited cluster aggregation (Meakin, 1987; e.g. Witten and Sander, 1983) from different combustion sources exhibit $D_f \approx 1.78 \pm 0.1$ and $k_0 = 1.3 \pm 0.2$ (Sorensen, 2011, and references therein). R_g denotes the radius of gyration of the soot aggregate. The radius of gyration can be related to the more readily measured mobility diameter, D_m , by (Sorensen, 2011):

$$\beta = \frac{D_m}{2R_g}, \quad (\text{E } 2)$$

which in the single particle limit, is given by (Sorensen, 2011):

$$\beta = \sqrt{\frac{5}{3}} = 1.29. \quad (\text{E } 3)$$

1160 The power law given in Eq. (E 1) is still valid when the primary particles are sintered, i.e. overlap to some degree as demonstrated by Oh et al. (1997). Furthermore, the factors $D_f \approx 1.78 \pm 0.1$ and $k_0 = 1.3 \pm 0.2$ lead to a good description of soot aggregates that formed through diffusion limited cluster aggregation, when primary particles overlap, although the values of D_f and k_0 increase slightly with increasing overlap coefficient (Oh and Sorensen, 1997).

1165 For the parametrization of the experimental data by Mahrt et al. (2018, 2020b) shown in Fig. 6, we rely on the soot characterization presented in Mahrt et al. (2018), who determined primary particle sizes of $D_m = 31$ nm and $D_m = 22$ nm, for miniCAST black and FW200, respectively, and fractal dimensions of $D_f = 1.86$ for miniCAST black and $D_f = 2.35$ for FW200. With these values, the number of primary particles as a function of mobility diameter of the soot aggregates can be determined using Eq. (E 1)–(E 3). The thus obtained values listed in Table 1 show that for the same aggregate size, the number of primary particles is higher for FW200 than for miniCAST black, owed to both, the smaller primary particle size and the higher fractal dimension of FW200.

1170



Table 1 Number of primary particles in soot aggregates as a function of soot aggregate mobility diameters D_m .

D_m	Number of primary particles, N_p	
	FW200	miniCAST black
400 nm	501	94
300 nm	255	55
200 nm	98	26
100 nm	19	7
80 nm	11	5
60 nm	6	3

1175 The number of primary particles is required as a parameter in Eq. (9) together with the fractal dimension to determine the probability that a soot aggregate contains a ring pore. Assuming that three-membered ring pores contribute to PCF, we use $n_m = 2$. For FW200, we determined the active-site probability as a function of RH_i because the experimental data acquired at 223 K and 218 K overlap when plotted as a function of RH_i suggesting that PCF is ice growth limited. We found good agreement to experimental AF for all aggregate sizes by choosing the following active-site probability function:

$$1180 \quad P_N(RH_i) = 10^{(a-bRH_i)^{-1}} \quad (\text{E } 4)$$

For miniCAST black, the experimental data acquired at 223 K and 218 K overlap when plotted as a function of RH_w , indicating that PCF is capillary condensation limited. Therefore, we determined the active-site probability function for this soot as a function of RH_w :

$$P_N(RH_w) = 10^{(a-bRH_w)^{-1}} \quad (\text{E } 5)$$

1185 The parameters used for the parameterizations are detailed in Table 2.

Table 2 Parameters used in Eq. 9 to calculate active fraction AF

	D_{pp}	D_f	k_0	n_m	a	b
FW200	22 nm	2.35	1	2	0.1544	0.002208
miniCAST black	31 nm	1.86	1.3	2	0.3374	0.006091



Appendix F List of Symbols and Abbreviations

<i>Symbol</i>	<i>Unit</i>	<i>Description</i>
AF	-	Activated fraction
C_{ov}	-	Primary particle overlap coefficient
CNT	-	Classical nucleation theory
d_{fl}	m	Width of the water slit in conical pores at the height of filling level (h_{fl})
D_f	-	Fractal dimension
D_{fl}	m	Diameter of cross-section of a spherical particle at the filling height h_{fl} above the midplane.
D_{ij}	m	Distance between centres of two overlapping spheres
D_m	m	Mobility diameter of soot aggregate
D_p	m	Diameter of pore
D_{pp}	m	Diameter of primary particle of soot
h_{fl}	m	Height of filling level
h_{fr}	m	Minimum height of capillary condensate in pore opening to allow for freezing to take place
h_{te}	m	Height of regular tetrahedron with apices at the centres of four neighbouring spheres
h_{tr}	m	Height of equilateral triangle formed between the centres of three spherical particles
h_{ov}	m	Height of overlap between two spheres
HEFA	-	Hydro-processed esters and fatty acids biofuel
HNT	K	Homogeneous nucleation temperature of water
INP	-	Ice nucleating particle
k	$J K^{-1}$	Boltzmann constant
k_0	-	Scaling pre-factor
MPC	-	Mixed-phase cloud
n_m	-	Indicator for pore type, i.e. ring structure type: $n_m = 3$ (four-ring), $n_m = 2$ (three-ring)
N_p	-	Number of (equally sized) primary particles in a soot aggregate
p	Pa	Water vapour pressure
$p_{w/i}$	Pa	Saturation vapour pressure with respect to water or ice
P	MPa	Absolute pressure within liquid phase
P_N	-	Active site probability fit function
P_0	MPa	Standard pressure (0.1 MPa)
ΔP	MPa	Pressure difference across water-water vapor interface of curved surface
PCF	-	Pore condensation and freezing



r	m	Radius of spherical ice cluster
r_c	m	Radius of curvature of the water surface
r_{crit}	m	Radius of critical ice germ
$r_{c,fl,tr}$	m	Principle radius of curvature of the meniscus at filling level (h_{fl}) in three-membered ring pore
$r_{c,fl,sq}$	m	Principle radius of curvature of the meniscus at filling level (h_{fl}) in four-membered ring pore
$r_{c,tr}$	m	Radius of circumcircle around three-membered ring pore
$r_{c,sq}$	m	Radius of circumcircle around four-membered ring pore
$r_{i,sq}$	m	Radius of incircle of square with apices at the centres of four neighbouring spheres (cubic packing arrangement)
$r_{i,te}$	m	Radius of sphere within concave octahedron (tetrahedral packing arrangement)
$r_{i,tr}$	m	Radius of incircle tangent to the sides of the equilateral triangle with corners at the centres of three nearest neighbour spheres.
$r_{o,cu}$	m	Radius of sphere between eight spheres arranged on the corners of a cube
$r_{o,sq}$	m	Radius of opening of four-membered ring pore
$r_{o,tr}$	m	Radius of opening of three-membered ring pore
$r_{o,te}$	m	Radius of sphere within concave octahedron (tetrahedral packing arrangement)
$r_{fl,tr}$	m	Radius of three-membered ring pore at filling level
$r_{fl,sq}$	m	Radius of four-membered ring pore at filling level
r_{c1}, r_{c2}	m	Principal radii of curvature of curved water surface
R_g	m	Radius of gyration
RH_i	%	Relative humidity with respect to ice
RH_w	%	Relative humidity with respect to water
S_i	-	Saturation ratio with respect to ice
S_w	-	Saturation ratio with respect to water
T	K	Absolute temperature
TEM	-	Transmission electron microscopy
$v_i(T)$	m ³	Molecular volume of water in the ice phase
$v_w(T)$	m ³	Molecular volume of liquid water
β	-	Ratio of mobility radius to radius of gyration of soot aggregate
$\gamma(T)$	Nm ⁻¹	General interfacial tension between two phases
$\gamma_{iw}(T)$	Nm ⁻¹	Interfacial tension between ice and water
$\gamma_{si}(T)$	Nm ⁻¹	Interfacial tension between soot and ice



$\gamma_{sw}(T)$	Nm^{-1}	Interfacial tension between soot and water
$\gamma_{vi}(T)$	Nm^{-1}	Interfacial tension between water vapor and ice
$\gamma_{vw}(T)$	Nm^{-1}	Interfacial tension between water vapor and water
$\gamma_{vs}(T)$	Nm^{-1}	Interfacial tension between water vapor and soot
δ	$^{\circ}$	Pore opening angle for conical pores
$\Delta G_{w,i}(T,P)$	J	Change in Gibbs free energy of homogeneous ice nucleation within supercooled liquid water
ε	$^{\circ}$	Slit filling angle/growth angle
ε_{ov}	$^{\circ}$	Angle of primary particle overlap, describing the angle between the center line between the particle centers and the height of the overlap
θ	$^{\circ}$	General contact angle
θ_{iw}	$^{\circ}$	Contact angle between ice and water
θ_{si}	$^{\circ}$	Contact angle between soot and ice
θ_{sw}	$^{\circ}$	Contact angle between soot and water
$\mu_i(T,P)$	J	Chemical potential of ice
$\mu_w(T,P)$	J	Chemical potential of water

1190

Data availability: The data used for the parameterization of soot-PCF can be found in Mahrt et al. (2018) and in Mahrt et al. (2020b).

1195

Competing interests: The authors declare that there is no conflict of interest.

Acknowledgements: We thank Kyeni S. Mbiti for constructing and rendering the 3D figures. This project has received funding from the European Union's Horizon 2020 research and innovation programme under the Marie Skłodowska-Curie grant agreement No 890200 (FM). We thank Franz Friebel and Zamin A. Kanji for reading the manuscript and for helpful comments.

1200

Author contributions: C.M. conceived the idea for the study. The theoretical soot-PCF framework was developed by C.M. and F.M., who also prepared the figures and wrote the manuscript with contributions from B.K. All authors were involved in discussions of results and data interpretation.



References

- 1205 Afrassiabian, Z., Leturia, M., Benali, M., Guessasma, M. and Saleh, K.: An overview of the role of capillary condensation in wet caking of powders, *Chem. Eng. Res. Des.*, 110, 245–254, doi:10.1016/j.cherd.2016.03.020, 2016.
- Alcala-Jornod, C., van den Bergh, H. and Rossi, M. J.: Reactivity of NO₂ and H₂O on soot generated in the laboratory: a diffusion tube study at ambient temperature, *Phys. Chem. Chem. Phys.*, 2(24), 5584–5593, doi:10.1039/B007235O, 2000.
- Amann, C. A. and Siegl, D. C.: Diesel Particulates—What They Are and Why, *Aerosol Sci. Technol.*, 1(1), 73–101, doi:10.1080/02786828208958580, 1981.
- 1210 Amaya, A. J. and Wyslouzil, B. E.: Ice nucleation rates near ~225 K, *J. Chem. Phys.*, 148(8), 084501, doi:10.1063/1.5019362, 2018.
- Ammann, M., Kalberer, M., Jost, D. T., Tobler, L., Rössler, E., Piguet, D., Gägeler, H. W. and Baltensperger, U.: Heterogeneous production of nitrous acid on soot in polluted air masses, *Nature*, 395(6698), 157–160, doi:10.1038/25965, 1998.
- 1215 Anderson, P. M., Guo, H. Q. and Sunderland, P. B.: Repeatability and reproducibility of TEM soot primary particle size measurements and comparison of automated methods, *J. Aerosol Sci.*, 114, 317–326, doi:10.1016/j.jaerosci.2017.10.002, 2017.
- Andreae, M. O. and Crutzen, P. J.: Atmospheric aerosols: Biogeochemical sources and role in atmospheric chemistry, *Science*, 276(5315), 1052–1058, doi:10.1126/science.276.5315.1052, 1997.
- 1220 Atiku, F. A., Mitchell, E. J. S., Lea-Langton, A. R., Jones, J. M., Williams, A. and Bartle, K. D.: The Impact of Fuel Properties on the Composition of Soot Produced by the Combustion of Residential Solid Fuels in a Domestic Stove, *Fuel Process. Technol.*, 151, 117–125, doi:10.1016/j.fuproc.2016.05.032, 2016.
- Bartell, L. S. and Chushak, Y. G.: Nucleation of Ice in Large Water Clusters: Experiment and Simulation, in *Water in Confining Geometries*, edited by V. Buch and J. P. Devlin, pp. 399–424, Springer, Berlin, Heidelberg, 2003.
- 1225 Bérubé, K. A., Jones, T. P., Williamson, B. J., Winters, C., Morgan, A. J. and Richards, R. J.: Physicochemical characterisation of diesel exhaust particles: Factors for assessing biological activity, *Atmos. Environ.*, 33(10), 1599–1614, doi:10.1016/S1352-2310(98)00384-7, 1999.
- Bescond, A., Yon, J., Ouf, F. X., Ferry, D., Delhaye, D., Gaffie, D., Coppalle, A. and Roze, C.: Automated Determination of Aggregate Primary Particle Size Distribution by TEM Image Analysis: Application to Soot, *Aerosol Sci. Technol.*, 48(8), 831–841, doi:10.1080/02786826.2014.932896, 2014.
- 1230 Bhandari, J., China, S., Chandrakar, K. K., Kinney, G., Cantrell, W., Shaw, R. A., Mazzoleni, L. R., Giroto, G., Sharma, N., Gorkowski, K., Gilardoni, S., Decesari, S., Facchini, M. C., Zanca, N., Pavese, G., Esposito, F., Dubey, M. K., Aiken, A. C., Chakrabarty, R. K., Moosmüller, H., Onasch, T. B., Zaveri, R. A., Scarnato, B. V., Fialho, P. and Mazzoleni, C.: Extensive Soot Compaction by Cloud Processing from Laboratory and Field Observations, *Sci. Rep.*, 9(1), 11824, doi:10.1038/s41598-019-48143-y, 2019.
- 1235 Bond, T. C. and Bergstrom, R. W.: Light Absorption by Carbonaceous Particles: An Investigative Review, *Aerosol Sci. Technol.*, 40(1), 27–67, doi:10.1080/02786820500421521, 2006.



- 1240 Bond, T. C., Doherty, S. J., Fahey, D. W., Forster, P. M., Bernsten, T., DeAngelo, B. J., Flanner, M. G., Ghan, S., Kaercher, B., Koch, D., Kinne, S., Kondo, Y., Quinn, P. K., Sarofim, M. C., Schultz, M. G., Schulz, M., Venkataraman, C., Zhang, H., Zhang, S., Bellouin, N., Guttikunda, S. K., Hopke, P. K., Jacobson, M. Z., Kaiser, J. W., Klimont, Z., Lohmann, U., Schwarz, J. P., Shindell, D., Storelvmo, T., Warren, S. G. and Zender, C. S.: Bounding the role of black carbon in the climate system: A scientific assessment, *J. Geophys. Res.-Atmospheres*, 118(11), 5380–5552, doi:10.1002/jgrd.50171, 2013.
- 1245 Bové, H., Bongaerts, E., Slenders, E., Bijmens, E. M., Saenen, N. D., Gyselaers, W., Eyken, P. V., Plusquin, M., Roeffaers, M. B. J., Ameloot, M. and Nawrot, T. S.: Ambient black carbon particles reach the fetal side of human placenta, *Nat. Commun.*, 10(1), 1–7, doi:10.1038/s41467-019-11654-3, 2019.
- Brasil, A. M., Farias, T. L. and Carvalho, M. G.: A RECIPE FOR IMAGE CHARACTERIZATION OF FRACTAL-LIKE AGGREGATES, *J. Aerosol Sci.*, 30(10), 1379–1389, doi:10.1016/S0021-8502(99)00026-9, 1999.
- 1250 Brasil, A. M., Farias, T. L. and Carvalho, M. G.: Evaluation of the Fractal Properties of Cluster Cluster Aggregates, *Aerosol Sci. Technol.*, 33(5), 440–454, doi:10.1080/02786820050204682, 2000.
- Burtscher, H.: Physical characterization of particulate emissions from diesel engines: a review, *J. Aerosol Sci.*, 36(7), 896–932, doi:10.1016/j.jaerosci.2004.12.001, 2005.
- 1255 China, S., Kulkarni, G., Scarnato, B., V., Sharma, N., Pekour, M., Shilling, J., E., Wilson, J., Zelenyuk, A., Chand, D., Liu, S., C. Aiken, A., Dubey, M. K., Laskin, A., Zaveri, R., A. and Mazzoleni, C.: Morphology of diesel soot residuals from supercooled water droplets and ice crystals: implications for optical properties, *Environ. Res. Lett.*, 10(11), 114010, 2015.
- Chou, C., Kanji, Z. A., Stetzer, O., Tritscher, T., Chirico, R., Heringa, M. F., Weingartner, E., Prevot, A. S. H., Baltensperger, U. and Lohmann, U.: Effect of photochemical ageing on the ice nucleation properties of diesel and wood burning particles, *Atmospheric Chem. Phys.*, 13(2), 761–772, doi:10.5194/acp-13-761-2013, 2013.
- 1260 Christenson, H. K.: Two-step crystal nucleation via capillary condensation, *Crystengcomm*, 15(11), 2030–2039, doi:10.1039/c3ce26887j, 2013.
- Clague, A. D. H., Donnet, J., Wang, T. K. and Peng, J. C. M.: A comparison of diesel engine soot with carbon black, *Carbon*, 37(10), 1553–1565, doi:10.1016/s0008-6223(99)00035-4, 1999.
- Colbeck, I., Appleby, L., Hardman, E. J. and Harrison, R. M.: The optical properties and morphology of cloud-processed carbonaceous smoke, *J. Aerosol Sci.*, 21(4), 527–538, doi:10.1016/0021-8502(90)90129-L, 1990.
- 1265 Cortés, D., Morán, J., Liu, F., Escudero, F., Consalvi, J.-L. and Fuentes, A.: Effect of Fuels and Oxygen Indices on the Morphology of Soot Generated in Laminar Coflow Diffusion Flames, *Energy Fuels*, 32(11), 11802–11813, doi:10.1021/acs.energyfuels.8b01301, 2018.
- 1270 Crawford, I., Moehler, O., Schnaiter, M., Saathoff, H., Liu, D., McMeeking, G., Linke, C., Flynn, M., Bower, K. N., Connolly, P. J., Gallagher, M. W. and Coe, H.: Studies of propane flame soot acting as heterogeneous ice nuclei in conjunction with single particle soot photometer measurements, *Atmospheric Chem. Phys.*, 11(18), 9549–9561, doi:10.5194/acp-11-9549-2011, 2011.
- Cziczo, D. J. and Froyd, K. D.: Sampling the composition of cirrus ice residuals, *Atmospheric Res.*, 142, 15–31, doi:10.1016/j.atmosres.2013.06.012, 2014.



- 1275 Cziczo, D. J., Thomson, D. S., Thompson, T. L., DeMott, P. J. and Murphy, D. M.: Particle analysis by laser mass spectrometry (PALMS) studies of ice nuclei and other low number density particles, *Int. J. Mass Spectrom.*, 258(1–3), 21–29, doi:10.1016/j.ijms.2006.05.013, 2006.
- Cziczo, D. J., Froyd, K. D., Hoose, C., Jensen, E. J., Diao, M., Zondlo, M. A., Smith, J. B., Twohy, C. H. and Murphy, D. M.: Clarifying the Dominant Sources and Mechanisms of Cirrus Cloud Formation, *Science*, 340(6138), 1320–1324, doi:10.1126/science.1234145, 2013.
- 1280 Dastanpour, R. and Rogak, S. N.: Observations of a Correlation Between Primary Particle and Aggregate Size for Soot Particles, *Aerosol Sci. Technol.*, 48(10), 1043–1049, doi:10.1080/02786826.2014.955565, 2014.
- Dastanpour, R., Boone, J. M. and Rogak, S. N.: Automated primary particle sizing of nanoparticle aggregates by TEM image analysis, *Powder Technol.*, 295, 218–224, doi:10.1016/j.powtec.2016.03.027, 2016.
- 1285 David, R. O., Marcolli, C., Fahrni, J., Qiu, Y. Q., Sirkin, Y. A. P., Molinero, V., Mahrt, F., Bruhwiler, D., Lohmann, U. and Kanji, Z. A.: Pore condensation and freezing is responsible for ice formation below water saturation for porous particles, *Proc. Natl. Acad. Sci. U. S. A.*, 116(17), 8184–8189, doi:10.1073/pnas.1813647116, 2019.
- David, R. O., Fahrni, J., Marcolli, C., Mahrt, F., Brühwiler, D. and Kanji, Z. A.: The role of contact angle and pore width on pore condensation and freezing, *Atmospheric Chem. Phys.*, 20(15), 9419–9440, doi:https://doi.org/10.5194/acp-20-9419-2020, 2020.
- 1290 Delhaye, D., Ouf, F.-X., Ferry, D., Ortega, I. K., Penanhoat, O., Peillon, S., Salm, F., Vancassel, X., Focsa, C., Irimiea, C., Harivel, N., Perez, B., Quinton, E., Yon, J. and Gaffie, D.: The MERMOSE project: Characterization of particulate matter emissions of a commercial aircraft engine, *J. Aerosol Sci.*, 105, 48–63, doi:10.1016/j.jaerosci.2016.11.018, 2017.
- DeMott, P. J.: An Exploratory Study of Ice Nucleation by Soot Aerosols, *J. Appl. Meteorol.*, 29(10), 1072–1079, doi:10.1175/1520-0450(1990)029<1072:AESOIN>2.0.CO;2, 1990.
- 1295 Diehl, K. and Mitra, S. K.: A laboratory study of the effects of a kerosene-burner exhaust on ice nucleation and the evaporation rate of ice crystals, *Atmos. Environ.*, 32(18), 3145–3151, doi:10.1016/s1352-2310(97)00467-6, 1998.
- Dubinin, M. M.: Water-vapor adsorption and the microporous structures of carbonaceous adsorbents, *Carbon*, 18(5), 355–364, doi:10.1016/0008-6223(80)90007-x, 1980.
- 1300 Dymarska, M., Murray, B. J., Sun, L. M., Eastwood, M. L., Knopf, D. A. and Bertram, A. K.: Deposition ice nucleation on soot at temperatures relevant for the lower troposphere, *J. Geophys. Res.-Atmospheres*, 111(D4), n/a-n/a, doi:10.1029/2005jd006627, 2006.
- Farkas, L.: Keimbildungsgeschwindigkeit in übersättigten Dämpfen (“The speed of germinative formation in over saturated vapours”), *Z. Für Phys. Chem. -Stoichiometrie Verwandtschaftslehre*, 125(3/4), 236–242, 1927.
- 1305 Feng, J. and Rothstein, J. P.: Simulations of novel nanostructures formed by capillary effects in lithography, *J. Colloid Interface Sci.*, 354(1), 386–395, doi:10.1016/j.jcis.2010.10.030, 2011.
- Ferraro, G., Fratini, E., Rausa, R., Fiaschi, P. and Baglioni, P.: Multiscale Characterization of Some Commercial Carbon Blacks and Diesel Engine Soot, *Energy Fuels*, 30(11), 9859–9866, doi:10.1021/acs.energyfuels.6b01740, 2016.
- Fisher, L. R., Gamble, R. A. and Middlehurst, J.: The Kelvin equation and the capillary condensation of water, *Nature*, 290(5807), 575–576, doi:10.1038/290575a0, 1981.



- 1310 Fletcher, N. H.: Ice crystal nucleation by aerosol particles, *Discuss. Faraday Soc.*, (30), 39–45, 1960.
- Fowkes, F. M. and Harkins, W. D.: The state of monolayers adsorbed at the interface solid-aqueous solution, *J. Am. Chem. Soc.*, 62, 3377–3386, doi:10.1021/ja01869a029, 1940.
- Friedman, B., Kulkarni, G., Beranek, J., Zelenyuk, A., Thornton, J. A. and Cziczo, D. J.: Ice nucleation and droplet formation by bare and coated soot particles, *J. Geophys. Res.-Atmospheres*, 116, doi:10.1029/2011jd015999, 2011.
- 1315 Fukuta, N.: Activation of Atmospheric Particles as Ice Nuclei in Cold and Dry Air, *J. Atmospheric Sci.*, 23(6), 741–750, doi:10.1175/1520-0469(1966)023<0741:aoapai>2.0.co;2, 1966.
- Gelman Constantin, J., Gianetti, M. M., Longinotti, M. P. and Corti, H. R.: The quasi-liquid layer of ice revisited: the role of temperature gradients and tip chemistry in AFM studies, *Atmospheric Chem. Phys.*, 18(20), 14965–14978, doi:https://doi.org/10.5194/acp-18-14965-2018, 2018.
- 1320 de Gennes, P. G.: Wetting: statics and dynamics, *Rev. Mod. Phys.*, 57(3), 827–863, doi:10.1103/RevModPhys.57.827, 1985.
- Gibbs, J. W.: *On the equilibrium of heterogeneous substances*, Published by the academy, New Haven., 1875.
- Gladkikh, M. and Bryant, S.: Prediction of interfacial areas during imbibition in simple porous media, *Adv. Water Resour.*, 26(6), 609–622, doi:10.1016/S0309-1708(03)00034-4, 2003.
- Gorbunov, B., Baklanov, A., Kakutkina, N., Toumi, R. and Windsor, H. L.: Ice nucleation on soot particles, *J. Aerosol Sci.*, 29, S1055–S1056, doi:10.1016/S0021-8502(98)90710-8, 1998.
- 1325 Gorbunov, B., Baklanov, A., Kakutkina, N., Windsor, H. L. and Toumi, R.: Ice nucleation on soot particles, *J. Aerosol Sci.*, 32(2), 199–215, doi:10.1016/S0021-8502(00)00077-X, 2001.
- Grishin, I., Thomson, K., Migliorini, F. and Sloan, J. J.: Application of the Hough transform for the automatic determination of soot aggregate morphology, *Appl. Opt.*, 51(5), 610–620, doi:10.1364/AO.51.000610, 2012.
- 1330 Han, C., Liu, Y. C., Liu, C., Ma, J. Z. and He, H.: Influence of Combustion Conditions on Hydrophilic Properties and Microstructure of Flame Soot, *J. Phys. Chem. A*, 116(16), 4129–4136, doi:10.1021/jp301041w, 2012.
- Harris, S. J. and Maricq, M. M.: Signature size distributions for diesel and gasoline engine exhaust particulate matter, *J. Aerosol Sci.*, 32(6), 749–764, doi:10.1016/S0021-8502(00)00111-7, 2001.
- 1335 Harris, S. J. and Maricq, M. M.: The role of fragmentation in defining the signature size distribution of diesel soot, *J. Aerosol Sci.*, 33(6), 935–942, doi:10.1016/S0021-8502(02)00045-9, 2002.
- Herndon, S. C., Jayne, J. T., Lobo, P., Onasch, T. B., Fleming, G., Hagen, D. E., Whitefield, P. D. and Miake-Lye, R. C.: Commercial Aircraft Engine Emissions Characterization of in-Use Aircraft at Hartsfield-Jackson Atlanta International Airport, *Environ. Sci. Technol.*, 42(6), 1877–1883, doi:10.1021/es072029+, 2008.
- 1340 Hess, W. M. and McDonald, G. C.: Improved Particle Size Measurements on Pigments for Rubber, *Rubber Chem. Technol.*, 56(5), 892–917, doi:10.5254/1.3538171, 1983.
- Higuchi, K. and Fukuta, N.: Ice in capillaries of solid particles and its effect on their nucleating ability, *J. Atmospheric Sci.*, 23(2), 187–190, doi:10.1175/1520-0469(1966)023<0187:iitcos>2.0.co;2, 1966.



- Hoard, J., Chafekar, T., Abarham, M., Schwader, R., Upplegger, S. and Styles, D.: Large Particles in Modern Diesel Engine Exhaust, pp. 521–530, American Society of Mechanical Engineers Digital Collection., 2013.
- 1345 Hruby, J., Vins, V., Mares, R., Hykl, J. and Kalova, J.: Surface Tension of Supercooled Water: No Inflection Point down to -25 degrees C, *J. Phys. Chem. Lett.*, 5(3), 425–428, doi:10.1021/jz402571a, 2014.
- Huang, J., Christ, J. A., Goltz, M. N. and Demond, A. H.: Modeling NAPL dissolution from pendular rings in idealized porous media, *Water Resour. Res.*, 51(10), 8182–8197, doi:10.1002/2015WR016924, 2015.
- 1350 ICAO Report: The World of Air Transport - Annual Report 2018, [online] Available from: <https://www.icao.int/annual-report-2018/Pages/default.aspx> (Accessed 23 April 2020), 2018.
- Ickes, L., Welti, A., Hoose, C. and Lohmann, U.: Classical nucleation theory of homogeneous freezing of water: thermodynamic and kinetic parameters, *Phys. Chem. Chem. Phys.*, 17(8), 5514–5537, doi:10.1039/C4CP04184D, 2015.
- 1355 Ikhenazene, R., Pirim, C., Noble, J. A., Irimiea, C., Carpentier, Y., Ortega, I. K., Ouf, F.-X., Focsa, C. and Chazallon, B.: Ice Nucleation Activities of Carbon-Bearing Materials in Deposition Mode: From Graphite to Airplane Soot Surrogates, *J. Phys. Chem. C*, 124(1), 489–503, doi:10.1021/acs.jpcc.9b08715, 2020.
- Jacobson, M. Z.: Strong radiative heating due to the mixing state of black carbon in atmospheric aerosols, *Nature*, 409(6821), 695–697, doi:10.1038/35055518, 2001.
- 1360 Janssen, N. A. H., Gerlofs-Nijland, M., Lanki, T., Salonen, R. O., Cassee, F., Hoek, G., Fischer, P., Brunekreef, B. and Krzyzanowski, M.: Health Effects of Black Carbon, World Health Organization, Copenhagen, Denmark. [online] Available from: <http://www.euro.who.int/pubre> (Accessed 14 April 2020), 2012.
- Kanji, Z. A. and Abbatt, J. P. D.: Laboratory studies of ice formation via deposition mode nucleation onto mineral dust and n-hexane soot samples, *J. Geophys. Res.-Atmospheres*, 111(D16), doi:10.1029/2005jd006766, 2006.
- Kanji, Z. A., Welti, A., Corbin, J. C. and Mensah, A. A.: Black Carbon Particles Do Not Matter for Immersion Mode Ice Nucleation, *Geophys. Res. Lett.*, 47(11), e2019GL086764, doi:10.1029/2019GL086764, 2020.
- 1365 Kärcher, B.: Cirrus Clouds and Their Response to Anthropogenic Activities, *Curr. Clim. Change Rep.*, 3(1), 45–57, doi:10.1007/s40641-017-0060-3, 2017.
- Kärcher, B.: Formation and radiative forcing of contrail cirrus, *Nat. Commun.*, 9(1), 1824, doi:10.1038/s41467-018-04068-0, 2018.
- 1370 Kärcher, B., Mohler, O., DeMott, P. J., Pechtl, S. and Yu, F.: Insights into the role of soot aerosols in cirrus cloud formation, *Atmospheric Chem. Phys.*, 7(16), 4203–4227, doi:10.5194/acp-7-4203-2007, 2007.
- Karjalainen, P., Pirjola, L., Heikkilä, J., Lähde, T., Tzamkiozis, T., Ntziachristos, L., Keskinen, J. and Rönkkö, T.: Exhaust particles of modern gasoline vehicles: A laboratory and an on-road study, *Atmos. Environ.*, 97, 262–270, doi:10.1016/j.atmosenv.2014.08.025, 2014.
- 1375 Kelvin, W. T.: Baltimore lectures on molecular dynamics and the wave theory of light, London: C. J. Clay and sons; Baltimore, Publication agency of the Johns Hopkins university. [online] Available from: <http://archive.org/details/baltimorelecture00kelviala> (Accessed 24 April 2020), 1904.



- Kilchhofer, K., Mahrt, F. and Kanji, Z. A.: The Role of Cloud Processing for the Ice Nucleating Ability of Organic Aerosol and Coal Fly Ash Particles, *J. Geophys. Res.-Atmospheres*, 2020.
- 1380 Kim, W., Kim, S. H., Lee, D. W., Lee, S., Lim, C. S. and Ryu, J. H.: Size Analysis of Automobile Soot Particles Using Field-Flow Fractionation, *Environ. Sci. Technol.*, 35(6), 1005–1012, doi:10.1021/es001329n, 2001.
- Kinsey, J. S., Dong, Y., Williams, D. C. and Logan, R.: Physical characterization of the fine particle emissions from commercial aircraft engines during the Aircraft Particle Emissions eXperiment (APEX) 1–3, *Atmos. Environ.*, 44(17), 2147–2156, doi:10.1016/j.atmosenv.2010.02.010, 2010.
- 1385 Kireeva, E. D., Popovicheva, O. B., Persiantseva, N. M., Khokhlova, T. D. and Shonija, N. K.: Effect of black carbon particles on the efficiency of water droplet freezing, *Colloid J.*, 71(3), 353–359, doi:10.1134/s1061933x09030090, 2009.
- Kiselev, A., Bachmann, F., Pedevilla, P., Cox, S. J., Michaelides, A., Gerthsen, D. and Leisner, T.: Active sites in heterogeneous ice nucleation—the example of K-rich feldspars, *Science*, doi:10.1126/science.aai8034, 2016.
- 1390 Koehler, K. A., DeMott, P. J., Kreidenweis, S. M., Popovicheva, O. B., Petters, M. D., Carrico, C. M., Kireeva, E. D., Khokhlova, T. D. and Shonija, N. K.: Cloud condensation nuclei and ice nucleation activity of hydrophobic and hydrophilic soot particles, *Phys. Chem. Chem. Phys.*, 11(36), 7906–7920, doi:10.1039/b905334b, 2009.
- Köylü, Ü. Ö. and Faeth, G. M.: Structure of overfire soot in buoyant turbulent diffusion flames at long residence times, *Combust. Flame*, 89(2), 140–156, doi:10.1016/0010-2180(92)90024-J, 1992.
- Köylü, U. O., Faeth, G. M., Farias, T. L. and Carvalho, M. G.: Fractal and projected structure properties of soot aggregates, *Combust. Flame*, 100(4), 621–633, doi:10.1016/0010-2180(94)00147-k, 1995.
- 1395 Kozbial, A., Zhou, F., Li, Z., Liu, H. and Li, L.: Are Graphitic Surfaces Hydrophobic?, *Acc. Chem. Res.*, 49(12), 2765–2773, doi:10.1021/acs.accounts.6b00447, 2016.
- 1400 Kulkarni, G., China, S., Liu, S., Nandasiri, M., Sharma, N., Wilson, J., Aiken, A. C., Chand, D., Laskin, A., Mazzoleni, C., Pekour, M., Shilling, J., Shutthanandan, V., Zelenyuk, A. and Zaveri, R. A.: Ice nucleation activity of diesel soot particles at cirrus relevant temperature conditions: Effects of hydration, secondary organics coating, soot morphology, and coagulation, *Geophys. Res. Lett.*, 43(7), 3580–3588, doi:10.1002/2016GL068707, 2016.
- Laksmono, H., McQueen, T. A., Sellberg, J. A., Loh, N. D., Huang, C., Schlesinger, D., Sierra, R. G., Hampton, C. Y., Nordlund, D., Beye, M., Martin, A. V., Barty, A., Seibert, M. M., Messerschmidt, M., Williams, G. J., Boutet, S., Amann-Winkel, K., Loerting, T., Pettersson, L. G. M., Bogan, M. J. and Nilsson, A.: Anomalous Behavior of the Homogeneous Ice Nucleation Rate in “No-Man’s Land,” *J. Phys. Chem. Lett.*, 6(14), 2826–2832, doi:10.1021/acs.jpcclett.5b01164, 2015.
- 1405 Laplace, P. S., Bowditch, N. and Bowditch, N. I. (Nathaniel I.: *Mécanique céleste*, Boston: Hillard, Gray, Little, and Wilkins. [online] Available from: <http://archive.org/details/mcaniquecles04laprich> (Accessed 24 April 2020), 1829.
- Laumbach, R. J. and Kipen, H. M.: Respiratory health effects of air pollution: Update on biomass smoke and traffic pollution, *J. Allergy Clin. Immunol.*, 129(1), 3–11, doi:10.1016/j.jaci.2011.11.021, 2012.
- 1410 Lee, D. S., Fahey, D. W., Skowron, A., Allen, M. R., Burkhardt, U., Chen, Q., Doherty, S. J., Freeman, S., Forster, P. M., Fuglestad, J., Gettelman, A., De León, R. R., Lim, L. L., Lund, M. T., Millar, R. J., Owen, B., Penner, J. E., Pitari, G., Prather, M. J., Sausen, R. and Wilcox, L. J.: The contribution of global aviation to anthropogenic climate forcing for 2000 to 2018, *Atmos. Environ.*, 117834, doi:10.1016/j.atmosenv.2020.117834, 2020.



- Li, J., Posfai, M., Hobbs, P. V. and Buseck, P. R.: Individual aerosol particles from biomass burning in southern Africa: 2, Compositions and aging of inorganic particles, *J. Geophys. Res.-Atmospheres*, 108(D13), doi:10.1029/2002jd002310, 2003.
- 1415 Liang, Y., Jen, C. N., Weber, R. J., Misztal, P. K. and Goldstein, A. H.: Chemical Composition of PM_{2.5} in October 2017 Northern California Wildfire Plumes, *Atmospheric Chem. Phys. Discuss.*, 1–33, doi:<https://doi.org/10.5194/acp-2020-910>, 2020.
- Liati, A., Brem, B. T., Durdina, L., Vöggtli, M., Arroyo Rojas Dasilva, Y., Dimopoulos Eggenschwiler, P. and Wang, J.: Electron Microscopic Study of Soot Particulate Matter Emissions from Aircraft Turbine Engines, *Environ. Sci. Technol.*, 48(18), 10975–10983, doi:10.1021/es501809b, 2014.
- 1420 Liati, A., Schreiber, D., Alpert, P. A., Liao, Y., Brem, B. T., Corral Arroyo, P., Hu, J., Jonsdottir, H. R., Ammann, M. and Dimopoulos Eggenschwiler, P.: Aircraft soot from conventional fuels and biofuels during ground idle and climb-out conditions: Electron microscopy and X-ray micro-spectroscopy, *Environ. Pollut.*, 247, 658–667, doi:10.1016/j.envpol.2019.01.078, 2019.
- 1425 Liu, L., Kong, S., Zhang, Y., Wang, Y., Xu, L., Yan, Q., Lingaswamy, A. P., Shi, Z., Lv, S., Niu, H., Shao, L., Hu, M., Zhang, D., Chen, J., Zhang, X. and Li, W.: Morphology, composition, and mixing state of primary particles from combustion sources — crop residue, wood, and solid waste, *Sci. Rep.*, 7(1), 5047, doi:10.1038/s41598-017-05357-2, 2017.
- Lobo, P., Durdina, L., Smallwood, G. J., Rindlisbacher, T., Siegerist, F., Black, E. A., Yu, Z., Mensah, A. A., Hagen, D. E., Miake-Lye, R. C., Thomson, K. A., Brem, B. T., Corbin, J. C., Abegglen, M., Sierau, B., Whitefield, P. D. and Wang, J.: Measurement of Aircraft Engine Non-Volatile PM Emissions: Results of the Aviation-Particle Regulatory Instrumentation Demonstration Experiment (A-PRIDE) 4 Campaign, *Aerosol Sci. Technol.*, 49(7), 472–484, doi:10.1080/02786826.2015.1047012, 2015.
- 1430 Lohmann, U.: A glaciation indirect aerosol effect caused by soot aerosols, *Geophys. Res. Lett.*, 29(4), 11-1-11-4, doi:10.1029/2001GL014357, 2002.
- 1435 Lohmann, U., Lüönd, F. and Mahrt, F.: *An Introduction to Clouds: From the Microscale to Climate*, 1st edition., Cambridge University Press, Cambridge., 2016.
- Lohmann, U., Friebel, F., Kanji, Z. A., Mahrt, F., Mensah, A. A. and Neubauer, D.: Future warming exacerbated by aged-soot effect on cloud formation, *Nat. Geosci.*, 13(10), 674–680, doi:10.1038/s41561-020-0631-0, 2020.
- 1440 Ma, X. F., Zangmeister, C. D., Gigault, J., Mulholland, G. W. and Zachariah, M. R.: Soot aggregate restructuring during water processing, *J. Aerosol Sci.*, 66, 209–219, doi:10.1016/j.jaerosci.2013.08.001, 2013.
- Mahrt, F., Marcolli, C., David, R. O., Grönquist, P., Barthazy Meier, E. J., Lohmann, U. and Kanji, Z. A.: Ice nucleation abilities of soot particles determined with the Horizontal Ice Nucleation Chamber, *Atmos Chem Phys*, 18(18), 13363–13392, doi:10.5194/acp-18-13363-2018, 2018.
- 1445 Mahrt, F., Alpert, P. A., Dou, J., Grönquist, P., Arroyo, P. C., Ammann, M., Lohmann, U. and Kanji, Z. A.: Aging induced changes in ice nucleation activity of combustion aerosol as determined by near edge X-ray absorption fine structure (NEXAFS) spectroscopy, *Environ. Sci. Process. Impacts*, doi:10.1039/C9EM00525K, 2020a.
- Mahrt, F., Kilchhofer, K., Marcolli, C., Grönquist, P., David, R. O., Rösch, M., Lohmann, U. and Kanji, Z. A.: The Impact of Cloud Processing on the Ice Nucleation Abilities of Soot Particles at Cirrus Temperatures, *J. Geophys. Res. Atmospheres*, 125(3), e2019JD030922, doi:10.1029/2019JD030922, 2020b.



- 1450 Manka, A., Pathak, H., Tanimura, S., Wölk, J., Strey, R. and Wyslouzil, B. E.: Freezing water in no-man's land, *Phys. Chem. Chem. Phys.*, 14(13), 4505–4516, doi:10.1039/C2CP23116F, 2012.
- Marcolli, C.: Deposition nucleation viewed as homogeneous or immersion freezing in pores and cavities, *Atmospheric Chem. Phys.*, 14(4), 2071–2104, doi:10.5194/acp-14-2071-2014, 2014.
- Marcolli, C.: Ice nucleation triggered by negative pressure, *Sci. Rep.*, 7(1), 1–8, doi:10.1038/s41598-017-16787-3, 2017a.
- 1455 Marcolli, C.: Pre-activation of aerosol particles by ice preserved in pores, *Atmospheric Chem. Phys.*, 17(3), 1596–1623, doi:10.5194/acp-17-1595-2017, 2017b.
- Marcolli, C.: Technical note: Fundamental aspects of ice nucleation via pore condensation and freezing including Laplace pressure and growth into macroscopic ice, *Atmospheric Chem. Phys.*, 20(5), 3209–3230, doi:https://doi.org/10.5194/acp-20-3209-2020, 2020.
- 1460 Marhaba, I., Ferry, D., Laffon, C., Regier, T. Z., Ouf, F.-X. and Parent, P.: Aircraft and MiniCAST soot at the nanoscale, *Combust. Flame*, 204, 278–289, doi:10.1016/j.combustflame.2019.03.018, 2019.
- Martinez-Martin, D., Longuinhos, R., Izquierdo, J. G., Marele, A., Alexandre, S. S., Jaafar, M., Gómez-Rodríguez, J. M., Bañares, L., Soler, J. M. and Gomez-Herrero, J.: Atmospheric contaminants on graphitic surfaces, *Carbon*, 61, 33–39, doi:10.1016/j.carbon.2013.04.056, 2013.
- 1465 Masiol, M. and Harrison, R. M.: Aircraft engine exhaust emissions and other airport-related contributions to ambient air pollution: A review, *Atmos. Environ.*, 95, 409–455, doi:10.1016/j.atmosenv.2014.05.070, 2014.
- Mason, B. J.: The nature of ice-forming nuclei in the atmosphere, *Q. J. R. Meteorol. Soc.*, 76(327), 59–74, doi:10.1002/qj.49707632707, 1950.
- Mazaheri, M., Johnson, G. R. and Morawska, L.: Particle and Gaseous Emissions from Commercial Aircraft at Each Stage of the Landing and Takeoff Cycle, *Environ. Sci. Technol.*, 43(2), 441–446, doi:10.1021/es8013985, 2009.
- McGraw, Z., Storelvmo, T., Samset, B. and Stjern, C. W.: Global radiative impacts of black carbon acting as ice nucleating particles, *Geophys. Res. Lett.*, n/a(n/a), e2020GL089056, doi:10.1029/2020GL089056, 2020.
- Meakin, P.: Fractal aggregates, *Adv. Colloid Interface Sci.*, 28, 249–331, doi:10.1016/0001-8686(87)80016-7, 1987.
- Megaridis, C. M. and Dobbins, R. A.: Morphological Description of Flame-Generated Materials, *Combust. Sci. Technol.*, 71(1–3), 95–109, doi:10.1080/00102209008951626, 1990.
- Miljevic, B., Surawski, N. C., Bostrom, T. and Ristovski, Z. D.: Restructuring of carbonaceous particles upon exposure to organic and water vapours, *J. Aerosol Sci.*, 47, 48–57, doi:10.1016/j.jaerosci.2011.12.005, 2012.
- Möhler, O., Büttner, S., Linke, C., Schnaiter, M., Saathoff, H., Stetzer, O., Wagner, R., Krämer, M., Mangold, A., Ebert, V. and Schurath, U.: Effect of sulfuric acid coating on heterogeneous ice nucleation by soot aerosol particles, *J. Geophys. Res. Atmospheres*, 110(D11), D11210, doi:10.1029/2004JD005169, 2005a.
- 1480 Möhler, O., Linke, C., Saathoff, H., Schnaiter, M., Wagner, R., Mangold, A., Kramer, M. and Schurath, U.: Ice nucleation on flame soot aerosol of different organic carbon content, *Meteorol. Z.*, 14(4), 477–484, doi:10.1127/0941-2948/2005/0055, 2005b.



- 1485 Moore, E. B., Allen, J. T. and Molinero, V.: Liquid-Ice Coexistence below the Melting Temperature for Water Confined in Hydrophilic and Hydrophobic Nanopores, *J. Phys. Chem. C*, 116(13), 7507–7514, doi:10.1021/jp3012409, 2012.
- Moore, R. H., Shook, M., Beyersdorf, A., Corr, C., Herndon, S., Knighton, W. B., Miake-Lye, R., Thornhill, K. L., Winstead, E. L., Yu, Z., Ziemba, L. D. and Anderson, B. E.: Influence of Jet Fuel Composition on Aircraft Engine Emissions: A Synthesis of Aerosol Emissions Data from the NASA APEX, AAFEX, and ACCESS Missions, *Energy Fuels*, 29(4), 2591–2600, doi:10.1021/ef502618w, 2015.
- 1490 Moore, R. H., Thornhill, K. L., Weinzierl, B., Sauer, D., D’Ascoli, E., Kim, J., Lichtenstern, M., Scheibe, M., Beaton, B., Beyersdorf, A. J., Barrick, J., Bulzan, D., Corr, C. A., Crosbie, E., Jurkat, T., Martin, R., Riddick, D., Shook, M., Slover, G., Voigt, C., White, R., Winstead, E., Yasky, R., Ziemba, L. D., Brown, A., Schlager, H. and Anderson, B. E.: Biofuel blending reduces particle emissions from aircraft engines at cruise conditions, *Nature*, 543(7645), 411–415, doi:10.1038/nature21420, 2017.
- 1495 Morcos, I.: Surface Tension of Stress-Annealed Pyrolytic Graphite, *J. Chem. Phys.*, 57(4), 1801–1802, doi:10.1063/1.1678482, 1972.
- Morishige, K.: Influence of Pore Wall Hydrophobicity on Freezing and Melting of Confined Water, *J. Phys. Chem. C*, 122(9), 5013–5019, doi:10.1021/acs.jpcc.8b00538, 2018.
- Mossop, S. C.: Sublimation Nuclei, *Proc. Phys. Soc. Sect. B*, 69(2), 161–164, 1956.
- 1500 Murray, B. J., Broadley, S. L., Wilson, T. W., Bull, S. J., Wills, R. H., Christenson, H. K. and Murray, E. J.: Kinetics of the homogeneous freezing of water, *Phys. Chem. Chem. Phys.*, 12(35), 10380–10387, doi:10.1039/C003297B, 2010.
- Nenow, D. and Trayanov, A.: Thermodynamics of crystal surfaces with quasi-liquid layer, *J. Cryst. Growth*, 79(1, Part 2), 801–805, doi:10.1016/0022-0248(86)90557-9, 1986.
- 1505 Nichman, L., Wolf, M., Davidovits, P., Onasch, T. B., Zhang, Y., Worsnop, D. R., Bhandari, J., Mazzoleni, C. and Cziczo, D. J.: Laboratory study of the heterogeneous ice nucleation on black-carbon-containing aerosol, *Atmos Chem Phys*, 19(19), 12175–12194, doi:10.5194/acp-19-12175-2019, 2019.
- Ogren, J. A. and Charlson, R. J.: Elemental carbon in the atmosphere: cycle and lifetime, *Tellus B Chem. Phys. Meteorol.*, 35(4), 241–254, doi:10.3402/tellusb.v35i4.14612, 1983.
- 1510 Oh, C. and Sorensen, C. M.: The Effect of Overlap between Monomers on the Determination of Fractal Cluster Morphology, *J. Colloid Interface Sci.*, 193(1), 17–25, doi:10.1006/jcis.1997.5046, 1997.
- Okada, K., Ikegami, M., Uchino, O., Nikaidou, Y., Zaizen, Y., Tsutsumi, Y. and Makino, Y.: Extremely high proportions of soot particles in the upper troposphere over Japan, *Geophys. Res. Lett.*, 19(9), 921–924, doi:10.1029/92GL00487, 1992.
- Olfert, J. and Rogak, S.: Universal relations between soot effective density and primary particle size for common combustion sources, *Aerosol Sci. Technol.*, 1–9, doi:10.1080/02786826.2019.1577949, 2019.
- 1515 Olfert, J. S., Dickau, M., Momenimovahed, A., Saffaripour, M., Thomson, K., Smallwood, G., Stettler, M. E. J., Boies, A., Sevcenco, Y., Crayford, A. and Johnson, M.: Effective density and volatility of particles sampled from a helicopter gas turbine engine, *Aerosol Sci. Technol.*, 51(6), 1–11, doi:10.1080/02786826.2017.1292346, 2017.



- 1520 Ouf, F. X., Yon, J., Ausset, P., Coppalle, A. and Maillé, M.: Influence of Sampling and Storage Protocol on Fractal Morphology of Soot Studied by Transmission Electron Microscopy, *Aerosol Sci. Technol.*, 44(11), 1005–1017, doi:10.1080/02786826.2010.507228, 2010.
- Ouf, F. X., Parent, P., Laffon, C., Marhaba, I., Ferry, D., Marcillaud, B., Antonsson, E., Benkoula, S., Liu, X. J., Nicolas, C., Robert, E., Patanen, M., Barreda, F. A., Sublemontier, O., Coppalle, A., Yon, J., Miserque, F., Mostefaoui, T., Regier, T. Z., Mitchell, J. A. and Miron, C.: First in-flight synchrotron X-ray absorption and photoemission study of carbon soot nanoparticles, *Sci Rep*, 6, 36495, doi:10.1038/srep36495, 2016.
- 1525 Ouf, F.-X., Bourrous, S., Vallières, C., Yon, J. and Lintis, L.: Specific surface area of combustion emitted particles: Impact of primary particle diameter and organic content, *J. Aerosol Sci.*, 137, 105436, doi:10.1016/j.jaerosci.2019.105436, 2019.
- Park, K., Kittelson, D. B. and McMurry, P. H.: Structural properties of diesel exhaust particles measured by transmission electron microscopy (TEM): Relationships to particle mass and mobility, *Aerosol Sci. Technol.*, 38(9), 881–889, doi:10.1080/027868290505189, 2004.
- 1530 Penner, J. E., Zhou, C., Garnier, A. and Mitchell, D. L.: Anthropogenic Aerosol Indirect Effects in Cirrus Clouds, *J. Geophys. Res.-Atmospheres*, 123(20), 11652–11677, doi:10.1029/2018jd029204, 2018.
- Persiantseva, N. M., Popovicheva, O. B. and Shonija, N. K.: Wetting and hydration of insoluble soot particles in the upper troposphere, *J. Environ. Monit.*, 6(12), 939–945, doi:10.1039/B407770A, 2004.
- 1535 Petzold, A., Strom, J., Ohlsson, S. and Schroder, F. P.: Elemental composition and morphology of ice-crystal residual particles in cirrus clouds and contrails, *Atmospheric Res.*, 49(1), 21–34, doi:10.1016/s0169-8095(97)00083-5, 1998.
- Popovicheva, O., Persiantseva, N. M., Shonija, N. K., DeMott, P., Koehler, K., Petters, M., Kreidenweis, S., Tishkova, V., Demirdjian, B. and Suzanne, J.: Water interaction with hydrophobic and hydrophilic soot particles, *Phys. Chem. Chem. Phys.*, 10(17), 2332–2344, doi:10.1039/B718944N, 2008.
- 1540 Popovicheva, O. B., Persiantseva, N. M., Trukhin, M. E., Rulev, G. B., Shonija, N. K., Buriko, Y. Y., Starik, A. M., Demirdjian, B., Ferry, D. and Suzanne, J.: Experimental characterization of aircraft combustor soot: Microstructure, surface area, porosity and water adsorption, *Phys. Chem. Chem. Phys.*, 2(19), 4421–4426, doi:10.1039/b004345l, 2000.
- Posfai, M., Simonics, R., Li, J., Hobbs, P. V. and Buseck, P. R.: Individual aerosol particles from biomass burning in southern Africa: 1. Compositions and size distributions of carbonaceous particles, *J. Geophys. Res.-Atmospheres*, 108(D13), doi:10.1029/2002jd002291, 2003.
- 1545 Pruppacher, H. R. and Klett, D. J.: *Microphysics of Clouds and Precipitation*, 2nd edition., Kluwer Academic Publishers, Dordrecht, The Netherlands., 1997.
- Ramanathan, V. and Carmichael, G.: Global and regional climate changes due to black carbon, *Nat. Geosci.*, 1(4), 221–227, doi:10.1038/ngeo156, 2008.
- 1550 Reddy, M. S. and Boucher, O.: Climate impact of black carbon emitted from energy consumption in the world's regions, *Geophys. Res. Lett.*, 34(11), doi:10.1029/2006gl028904, 2007.
- Rockne, K. J., Taghon, G. L. and Kosson, D. S.: Pore structure of soot deposits from several combustion sources, *Chemosphere*, 41(8), 1125–1135, doi:10.1016/S0045-6535(00)00040-0, 2000.



- Roessler, D. M.: Diesel particle mass concentration by optical techniques, *Appl. Opt.*, 21(22), 4077–4086, doi:10.1364/AO.21.004077, 1982.
- 1555 Rose, D., Wehner, B., Ketzler, M., Engler, C., Voigtlander, J., Tuch, T. and Wiedensohler, A.: Atmospheric number size distributions of soot particles and estimation of emission factors, *Atmospheric Chem. Phys.*, 6, 1021–1031, 2006.
- Samson, R. J., Mulholland, G. W. and Gentry, J. W.: Structural-analysis of soot agglomerates, *Langmuir*, 3(2), 272–281, doi:10.1021/la00074a022, 1987.
- 1560 Schill, G. P., Jathar, S. H., Kodros, J. K., Levin, E. J. T., Galang, A. M., Friedman, B., Link, M. F., Farmer, D. K., Pierce, J. R., Kreidenweis, S. M. and DeMott, P. J.: Ice-nucleating particle emissions from photochemically aged diesel and biodiesel exhaust, *Geophys. Res. Lett.*, 43(10), 5524–5531, doi:10.1002/2016gl069529, 2016.
- Schill, G. P., DeMott, P. J., Emerson, E. W., Rauker, A. M. C., Kodros, J. K., Suski, K. J., Hill, T. C. J., Levin, E. J. T., Pierce, J. R., Farmer, D. K. and Kreidenweis, S. M.: The contribution of black carbon to global ice nucleating particle concentrations relevant to mixed-phase clouds, *Proc. Natl. Acad. Sci.*, doi:10.1073/pnas.2001674117, 2020a.
- 1565 Schill, G. P., Froyd, K. D., Bian, H., Kupc, A., Williamson, C., Brock, C. A., Ray, E., Hornbrook, R. S., Hills, A. J., Apel, E. C., Chin, M., Colarco, P. R. and Murphy, D. M.: Widespread biomass burning smoke throughout the remote troposphere, *Nat. Geosci.*, 1–6, doi:10.1038/s41561-020-0586-1, 2020b.
- Schrader, M. E.: Ultrahigh vacuum techniques in the measurement of contact angles. IV. Water on graphite (0001), *J. Phys. Chem.*, 79(23), 2508–2515, doi:10.1021/j100590a013, 1975.
- 1570 Shin, Y. J., Wang, Y., Huang, H., Kalon, G., Wee, A. T. S., Shen, Z., Bhatia, C. S. and Yang, H.: Surface-Energy Engineering of Graphene, *Langmuir*, 26(6), 3798–3802, doi:10.1021/la100231u, 2010.
- Smekens, A., Godoi, R. H. M., Berghmans, P. and Van Grieken, R.: Characterisation of Soot Emitted by Domestic Heating Aircraft and Cars Using Diesel or Biodiesel, *J. Atmospheric Chem.*, 52(1), 45–62, doi:10.1007/s10874-005-6903-7, 2005.
- 1575 Son, S., Chen, L., Kang, Q., Derome, D. and Carmeliet, J.: Contact Angle Effects on Pore and Corner Arc Menisci in Polygonal Capillary Tubes Studied with the Pseudopotential Multiphase Lattice Boltzmann Model, *Computation*, 4(1), 12, doi:10.3390/computation4010012, 2016.
- Sorensen, C. M.: The Mobility of Fractal Aggregates: A Review, *Aerosol Sci. Technol.*, 45(7), 765–779, doi:10.1080/02786826.2011.560909, 2011.
- 1580 Sorensen, C. M., Cai, J. and Lu, N.: Light-scattering measurements of monomer size, monomers per aggregate, and fractal dimension for soot aggregates in flames, *Appl. Opt.*, 31(30), 6547–6557, doi:10.1364/AO.31.006547, 1992.
- Su, D. S., Müller, J.-O., Jentoft, R. E., Rothe, D., Jacob, E. and Schlögl, R.: Fullerene-like soot from EuroIV diesel engine: consequences for catalytic automotive pollution control, *Top. Catal.*, 30(1), 241–245, doi:10.1023/B:TOCA.0000029756.50941.02, 2004.
- 1585 Thomson, W. F. R. S.: LX. On the equilibrium of vapour at a curved surface of liquid, *Lond. Edinb. Dublin Philos. Mag. J. Sci.*, 42(282), 448–452, doi:10.1080/14786447108640606, 1871.
- Twohy, C. H. and Gandrud, B. W.: Electron microscope analysis of residual particles from aircraft contrails, *Geophys. Res. Lett.*, 25(9), 1359–1362, doi:10.1029/97gl03162, 1998.



- 1590 Ullrich, R., Hoose, C., Möhler, O., Niemand, M., Wagner, R., Höhler, K., Hiranuma, N., Saathoff, H. and Leisner, T.: A New Ice Nucleation Active Site Parameterization for Desert Dust and Soot, *J. Atmospheric Sci.*, 74(3), 699–717, doi:10.1175/jas-d-16-0074.1, 2017.
- Umo, N. S., Wagner, R., Ullrich, R., Kiselev, A., Saathoff, H., Weidler, P. G., Cziczo, D. J., Leisner, T. and Möhler, O.: Enhanced ice nucleation activity of coal fly ash aerosol particles initiated by ice-filled pores, *Atmos Chem Phys*, 19(13), 8783–8800, doi:10.5194/acp-19-8783-2019, 2019.
- 1595 Urso, M. E. D., Lawrence, C. J. and Adams, M. J.: Pendular, Funicular, and Capillary Bridges: Results for Two Dimensions, *J. Colloid Interface Sci.*, 220(1), 42–56, doi:10.1006/jcis.1999.6512, 1999.
- Vali, G., DeMott, P. J., Mohler, O. and Whale, T. F.: Technical Note: A proposal for ice nucleation terminology, *Atmospheric Chem. Phys.*, 15(18), 10263–10270, doi:10.5194/acp-15-10263-2015, 2015.
- Vargaftik, N. B., Volkov, B. N. and Voljak, L. D.: International tables of the surface-tension of water, *J. Phys. Chem. Ref. Data*, 12(3), 817–820, 1983.
- 1600 Vergara-Temprado, J., Holden, M. A., Orton, T. R., O’Sullivan, D., Umo, N. S., Browse, J., Reddington, C., Baeza-Romero, M. T., Jones, J. M., Lea-Langton, A., Williams, A., Carslaw, K. S. and Murray, B. J.: Is Black Carbon an Unimportant Ice-Nucleating Particle in Mixed-Phase Clouds?, *J. Geophys. Res. Atmospheres*, 123(8), 4273–4283, doi:10.1002/2017JD027831, 2018.
- 1605 Wagner, R., Kiselev, A., Möhler, O., Saathoff, H. and Steinke, I.: Pre-activation of ice-nucleating particles by the pore condensation and freezing mechanism, *Atmospheric Chem. Phys.*, 16(4), 2025–2042, doi:10.5194/acp-16-2025-2016, 2016.
- Wallace, J. M. and Hobbs, P. V.: *Atmospheric science: an introductory survey*, Elsevier Acad. Press, Amsterdam., 2011.
- Wang, Q., Jacob, D. J., Spackman, J. R., Perring, A. E., Schwarz, J. P., Moteki, N., Marais, E. A., Ge, C., Wang, J. and Barrett, S. R. H.: Global budget and radiative forcing of black carbon aerosol: Constraints from pole-to-pole (HIPPO) observations across the Pacific, *J. Geophys. Res. Atmospheres*, 119(1), 195–206, doi:10.1002/2013JD020824, 2014.
- 1610 Wei, Y., Zhang, Q. and Thompson, J. E.: The Wetting Behavior of Fresh and Aged Soot Studied through Contact Angle Measurements, *Atmospheric Clim. Sci.*, 07(01), 11–22, doi:10.4236/acs.2017.71002, 2017.
- Welti, A., Kanji, Z. A., Lüönd, F., Stetzer, O. and Lohmann, U.: Exploring the Mechanisms of Ice Nucleation on Kaolinite: From Deposition Nucleation to Condensation Freezing, *J. Atmospheric Sci.*, 71(1), 16–36, doi:10.1175/jas-d-12-0252.1, 2014.
- 1615 Wentzel, M., Gorzawski, H., Naumann, K. H., Saathoff, H. and Weinbruch, S.: Transmission electron microscopical and aerosol dynamical characterization of soot aerosols, *J. Aerosol Sci.*, 34(10), 1347–1370, doi:10.1016/S0021-8502(03)00360-4, 2003.
- Westreich, P., Fortier, H., Flynn, S., Foster, S. and Dahn, J. R.: Exclusion of Salt Solutions from Activated Carbon Pores and the Relationship to Contact Angle on Graphite, *J. Phys. Chem. C*, 111(9), 3680–3684, doi:10.1021/jp066800z, 2007.
- 1620 Wettlaufer, J. S.: Crystal Growth, Surface Phase Transitions and Thermomolecular Pressure, in *Ice Physics and the Natural Environment*, edited by J. S. Wettlaufer, J. G. Dash, and N. Untersteiner, pp. 39–67, Springer, Berlin, Heidelberg., 1999.
- Witten, T. A. and Sander, L. M.: Diffusion-limited aggregation, *Phys. Rev. B*, 27(9), 5686–5697, doi:10.1103/PhysRevB.27.5686, 1983.



- Yon, J., Bescond, A. and Liu, F.: On the radiative properties of soot aggregates part 1: Necking and overlapping, *J. Quant. Spectrosc. Radiat. Transf.*, 162, 197–206, doi:10.1016/j.jqsrt.2015.03.027, 2015.
- 1625 Young, T.: An essay on the cohesion of fluids, *Philos. Trans. R. Soc. Lond.* 1776-1886, 95, 65–87, doi:10.1098/rstl.1805.0005, 1805.
- Zaragoza, A., Conde, M. M., Espinosa, J. R., Valeriani, C., Vega, C. and Sanz, E.: Competition between ices Ih and Ic in homogeneous water freezing, *J. Chem. Phys.*, 143(13), 134504, doi:10.1063/1.4931987, 2015.
- 1630 Zelenay, V., Monge, M. E., D’Anna, B., George, C., Styler, S. A., Huthwelker, T. and Ammann, M.: Increased steady state uptake of ozone on soot due to UV/Vis radiation, *J. Geophys. Res.-Atmospheres*, 116(D11), doi:10.1029/2010jd015500, 2011.
- Zhang, C., Zhang, Y., Wolf, M. J., Nichman, L., Shen, C., Onasch, T. B., Chen, L. and Cziczo, D. J.: The effects of morphology, mobility size and SOA material coating on the ice nucleation activity of black carbon in the cirrus regime, *Atmospheric Chem. Phys. Discuss.*, 1–40, doi:https://doi.org/10.5194/acp-2020-809, 2020.
- 1635 Zhao, B., Wang, Y., Gu, Y., Liou, K.-N., Jiang, J. H., Fan, J., Liu, X., Huang, L. and Yung, Y. L.: Ice nucleation by aerosols from anthropogenic pollution, *Nat. Geosci.*, doi:10.1038/s41561-019-0389-4, 2019.
- Zhou, C. and Penner, J. E.: Aircraft soot indirect effect on large-scale cirrus clouds: Is the indirect forcing by aircraft soot positive or negative?, *J. Geophys. Res. Atmospheres*, 119(19), 11,303-11,320, doi:10.1002/2014JD021914, 2014.
- Zuberi, B., Johnson, K. S., Aleks, G. K., Molina, L. T., Molina, M. J. and Laskin, A.: Hydrophilic properties of aged soot, *Geophys. Res. Lett.*, 32(L01807), doi:10.1029/2004GL021496, 2005.

1640